MUTUAL COUPLING CALIBRATION OF ANTENNA ARRAYS FOR DIRECTION-OF-ARRIVAL ESTIMATION

A THESIS SUBMITTED TO
THE GRADUATE SCHOOL OF NATURAL AND APPLIED SCIENCES
OF
MIDDLE EAST TECHNICAL UNIVERSITY

BY

TAYLAN AKSOY

IN PARTIAL FULFILLMENT OF THE REQUIREMENTS
FOR
THE DEGREE OF MASTER OF SCIENCE
IN
ELECTRICAL AND ELECTRONICS ENGINEERING

FEBRUARY 2012

Approval of the thesis:

MUTUAL COUPLING CALIBRATION OF ANTENNA ARRAYS FOR DIRECTION-OF-ARRIVAL ESTIMATION

submitted by **TAYLAN AKSOY** in partial fulfillment of the requirements for the degree of **Master of Science in Electrical and Electronics Engineering Department, Middle East Technical University** by,

Prof. Dr. Canan Özgen
Dean, Graduate School of **Natural and Applied Sciences** _____

Prof. Dr. İsmet Erkmen
Head of Department, **Electrical and Electronics Engineering** _____

Prof. Dr. T. Engin Tuncer
Supervisor, **Electrical and Electronics Eng. Dept., METU** _____

Examining Committee Members:

Prof. Dr. Buyurman Baykal
Electrical and Electronics Engineering Dept., METU _____

Prof. Dr. T. Engin Tuncer
Electrical and Electronics Engineering Dept., METU _____

Assoc. Prof. Dr. Şimşek Demir
Electrical and Electronics Engineering Dept., METU _____

Dr. Arzu Koç
Electrical and Electronics Engineering Dept., METU _____

Dr. Tansu Filik
REHİS Division, ASELSAN _____

Date: _____

I hereby declare that all information in this document has been obtained and presented in accordance with academic rules and ethical conduct. I also declare that, as required by these rules and conduct, I have fully cited and referenced all material and results that are not original to this work.

Name, Last Name: TAYLAN AKSOY

Signature :

ABSTRACT

MUTUAL COUPLING CALIBRATION OF ANTENNA ARRAYS FOR DIRECTION-OF-ARRIVAL ESTIMATION

Aksoy, Taylan

M.Sc., Department of Electrical and Electronics Engineering

Supervisor : Prof. Dr. T. Engin Tuncer

February 2012, 82 pages

An antenna array is an indispensable portion of a direction-of-arrival (DOA) estimation operation. A number of error sources in the arrays degrade the DOA estimation accuracy. Mutual coupling effect is one of the main error sources and should be corrected for any antenna array.

In this thesis, a system theoretic approach is presented for mutual coupling characterization of antenna arrays. In this approach, the idea is to model the mutual coupling effect through a simple linear transformation between the measured and the ideal array data. In this context, a measurement reduction method (MRM) is proposed to decrease the number of calibration measurements. This new method dramatically reduces the number of calibration measurements for omnidirectional antennas. It is shown that a single calibration measurement is sufficient for uniform circular arrays when MRM is used.

The method is extended for the arrays composed of non-omnidirectional (NOD) antennas. It is shown that a single calibration matrix can not properly model the mutual

coupling effect in an NOD antenna array. Therefore, a sectorized calibration approach is proposed for NOD antenna arrays where the mutual coupling calibration is done in angular sectors.

Furthermore, mutual coupling problem is also investigated for antenna arrays over a perfect electric conductor plate. In this case, reflections from the plate lead to gain/phase mismatches in the antenna elements. In this context, a composite matrix approach is proposed where mutual coupling and gain/phase mismatch are jointly modelled by using a single composite calibration matrix.

The proposed methods are evaluated over DOA estimation accuracies using Multiple Signal Classification (MUSIC) algorithm. The calibration measurements are obtained using the numerical electromagnetic simulation tool FEKO. The evaluation results show that the proposed methods effectively realize the mutual coupling calibration of antenna arrays.

Keywords: mutual coupling, antenna array calibration, direction-of-arrival estimation

ÖZ

GELİŞ-AÇISI KESTİRİMİ İÇİN ANTEN DİZİLERİNİN MÜŞTEREK BAĞLAŞIM KALİBRASYONU

Aksoy, Taylan
Yüksek Lisans, Elektrik Elektronik Mühendisliğ Bölümü
Tez Yöneticisi : Prof. Dr. T. Engin Tuncer

Şubat 2012, 82 sayfa

Anten dizisi, geliş-açısı kestirimi işleminin vazgeçilmez bir parçasıdır. Dizilerde bulunan birçok hata kaynağı, kestirim sonuçlarının doğruluğunu düşürmektedir. Anten elemanları arasındaki müşterek bağlaşım etkisi, bir anten dizisindeki temel hata kaynaklarından biridir ve her anten dizisinde düzeltilmesi gereklidir.

Bu tezde, anten dizilerindeki müşterek bağlaşım etkisinin karakterizasyonu için sistematik bir yaklaşım sunulmaktadır. Bu kapmsamda, kalibrasyon ölçüm sayısının azaltılması için bir ölçüm azaltma yöntemi (ÖAY) önerilmektedir. Bu yeni yöntem, eşyönlü antenler için kalibrasyon ölçüm sayısını önemli ölçüde azaltmaktadır. ÖAY kullanılması durumunda, tekdüze dairesel diziler için bir tek kalibrasyon ölçümünün yeterli olduğu gösterilmiştir.

Yöntem, eşyönlü olmayan antenlerde uygulanmak üzere genişletilmiştir. Tek bir kalibrasyon matrisinin, eşyönlü olmayan antenlerden oluşan dizilerdeki müşterek bağlaşım etkisini modellemek için yeterli olmadığı gösterilmiştir. Bu nedenle, eşyönlü olmayan antenlerden oluşan diziler için, müşterek bağlaşım kalibrasyonunun açısal sektörler

kullanılarak yapıldığı bir sektörlü yaklaşım önerilmiştir.

Müşterek bağlaşım problemi, kusursuz elektriksel iletken bir plaka üzerinde duran anten dizileri için de incelenmiştir. Bu durumda, plakadan gelen yansımalar, anten elemanlarında kazanç/faz uyuşmazlıklarına yol açmaktadır. Bu kapsamda, müşterek bağlaşım ve kazanç/faz uyuşmazlığının, bir tek bileşik kalibrasyon matrisi kullanarak birlikte modellendiği bir bileşik matris yaklaşımı önerilmiştir.

Önerilen yöntemler, Çoklu Sinyal Sınıflandırma (Multiple Signal Classification, MUSIC) algoritması ile yapılan geliş-açısı kestirimindeki doğruluk miktarları kullanılarak değerlendirilmiştir. Kalibrasyon ölçümleri, nümerik elektromanyetik simülasyon aracı olan FEKO kullanılarak yapılmıştır. Değerlendirme sonuçları, önerilen yöntemlerin anten dizilerinde müşterek bağlaşım kalibrasyonunu etkin bir biçimde yapabildiğini göstermektedir.

Anahtar Kelimeler: müşterek bağlaşım, anten dizisi kalibrasyonu, geliş-açısı kestirimi

To my mother Aliye Aksoy,

ACKNOWLEDGMENTS

I would like to emphasize my sincere gratitude to my supervisor Prof. Dr. T. Engin Tuncer for his invaluable guidance, advice and help throughout this study.

I appreciate my mother Aliye for her endless love and numerous sacrifices in my life. Her encouraging advices became my main motivation in completing this study just as in all the previous stringent cases throughout my life.

I am grateful to my sister Ceren for her love and friendship during all my life. She has always been my best friend and confidant. Thank goodness for her existence in my life.

I want to express my appreciation to my collegues and my manager in ASELSAN for their patience and encouragement during this study.

I would like to thank to The Scientific and Technological Research Council of Turkey (TÜBİTAK) for the scholarship they provided to me during this study.

TABLE OF CONTENTS

ABSTRACT iv

ÖZ vi

ACKNOWLEDGMENTS ix

TABLE OF CONTENTS x

LIST OF TABLES xii

LIST OF FIGURES xiii

CHAPTERS

1 INTRODUCTION 1

1.1 Thesis Organization 4

2 REVIEW OF THE METHODS FOR MUTUAL COUPLING CALIBRATION 5

2.1 The Open-Circuit Method 5

2.2 The Yamada's Method 7

2.3 The Sato's Method 9

2.4 The Hui's Method 13

3 MUTUAL COUPLING CALIBRATION OF OMNIDIRECTIONAL ANTENNA ARRAYS 16

3.1 Signal Model 17

3.2 Transformation Approach 18

3.3 Measurement Reduction Method 21

3.4 Simulations 28

4 MUTUAL COUPLING CALIBRATION OF NON-OMNIDIRECTIONAL ANTENNA ARRAYS 41

4.1 Signal Model 41

4.2 Sectorized Approach 43

4.3 MRM for NOD Antenna Arrays 45
4.4 Simulations 49
5 MUTUAL COUPLING AND GAIN/PHASE MISMATCH CALIBRATION OF ANTENNA ARRAYS OVER A PEC PLATE 58
5.1 Signal Model 59
5.2 Composite Matrix Approach 60
5.3 Simulations 63
6 CONCLUSIONS 77
REFERENCES 81

LIST OF TABLES

TABLES

Table 3.1 Number of calibration measurements required for different types of arrays which are composed of N identical and omnidirectional antennas. ($\lceil \cdot \rceil$ denotes the ceiling function.) 28

LIST OF FIGURES

FIGURES

Figure 2.1 The N-element antenna array is treated as an $(N+1)-$terminal network 6

Figure 3.1 The array elements e_1, e_2 and the directions (ϕ_1, θ_1), (ϕ_2, θ_2) are symmetrical to each other with respect to the symmetry plane s_1. 23

Figure 3.2 Two dimensional geometry of a UCA with N elements, $e_1, e_2, \ldots, e_N$, and S symmetry planes, $s_1, s_2, \ldots, s_S$,. There are S symmetric couples, $[\mathbf{g_i}, \mathbf{g_{i+1}}]$ $(i = 1, 3, \ldots, 2S-1)$, in the array. 25

Figure 3.3 The radiation pattern of a single dipole antenna with 5.25 mm diameter and 34.1 cm length at 100 MHz. 29

Figure 3.4 The radiation pattern of a single dipole antenna with 5.25 mm diameter and 34.1 cm length at 440 MHz. 29

Figure 3.5 The radiation pattern of a single dipole antenna with 5.25 mm diameter and 34.1 cm length at 800 MHz. 29

Figure 3.6 The 8-element UCA model used in the performance evaluation experiments. 30

Figure 3.7 The MUSIC spectrum due to three sources at 100 MHz coming from $(\phi_1 = 50^\circ, \theta_1 = 90^\circ)$, $(\phi_2 = 90^\circ, \theta_2 = 90^\circ)$ and $(\phi_3 = 200^\circ, \theta_3 = 90^\circ)$ directions, respectively. 32

Figure 3.8 The MUSIC spectrum due to three sources at 440 MHz coming from $(\phi_1 = 50^\circ, \theta_1 = 90^\circ)$, $(\phi_2 = 90^\circ, \theta_2 = 90^\circ)$ and $(\phi_3 = 200^\circ, \theta_3 = 90^\circ)$ directions, respectively. 32

Figure 3.9 The MUSIC spectrum due to three sources at 800 MHz coming from ($\phi_1 = 50°, \theta_1 = 90°$), ($\phi_2 = 90°, \theta_2 = 90°$) and ($\phi_3 = 200°, \theta_3 = 90°$) directions, respectively. 33

Figure 3.10 The azimuth performances of MRM and the Hui's method at 100 MHz when two sources are fixed at $\phi_1 = 50°$ and $\phi_2 = 90°$, and the third source is swept in one degree resolution. 34

Figure 3.11 The azimuth performances of MRM and the Hui's method at 440 MHz when two sources are fixed at $\phi_1 = 50°$ and $\phi_2 = 90°$, and the third source is swept in one degree resolution. 35

Figure 3.12 The azimuth performances of MRM and the Hui's method at 800 MHz when two sources are fixed at $\phi_1 = 50°$ and $\phi_2 = 90°$, and the third source is swept in one degree resolution. 35

Figure 3.13 The performance comparison of MRM and the Hui's method for the noisy case. The experiment is done at 440 MHz for 20 dB SNR. There are two fixed sources from $\phi_1 = 50°$ and $\phi_2 = 90°$, and the third source is swept in one degree resolution. 36

Figure 3.14 The elevation performance of MRM at 100 MHz for three sources whose elevation angles $\theta_1 = \theta_2 = \theta_3$ are varied from 75° to 105° with 3 degree steps. 37

Figure 3.15 The elevation performance of MRM at 440 MHz for three sources whose elevation angles $\theta_1 = \theta_2 = \theta_3$ are varied from 75° to 105° with 3 degree steps. 38

Figure 3.16 The elevation performance of MRM at 800 MHz for three sources whose elevation angles $\theta_1 = \theta_2 = \theta_3$ are varied from 75° to 105° with 3 degree steps. 38

Figure 3.17 The frequency performance of MRM for three sources whose frequencies $f_1 = f_2 = f_3$ are varried between 95 MHz and 105 MHz. 39

Figure 3.18 The frequency performance of MRM for three sources whose frequencies $f_1 = f_2 = f_3$ are varried between 435 MHz and 445 MHz. 40

Figure 3.19 The frequency performance of MRM for three sources whose frequencies $f_1 = f_2 = f_3$ are varried between 795 MHz and 805 MHz. 40

Figure 4.1 The top view of a UCA with N patch antenna elements, $e_1, e_2, \ldots, e_N$. There are S symmetry planes, $s_1, s_2, \ldots, s_S$, in the array. 46

Figure 4.2 The three dimensional transmitting array pattern due to e_2 from top, front and isometric view angles. 47

Figure 4.3 The three dimensional transmitting array pattern due to e_N from top, front and isometric view angles. 48

Figure 4.4 The wideband non-symmetric dipole patch antenna [17] used in the experiments. 50

Figure 4.5 Three dimensional radiation pattern of the semi-omnidirectional antenna at 100 MHz. 50

Figure 4.6 Three dimensional radiation pattern of the semi-omnidirectional antenna at 300 MHz. 51

Figure 4.7 Three dimensional radiation pattern of the semi-omnidirectional antenna at 440 MHz. 51

Figure 4.8 Three dimensional radiation pattern of the semi-omnidirectional antenna at 600 MHz. 52

Figure 4.9 Three dimensional radiation pattern of the semi-omnidirectional antenna at 800 MHz. 52

Figure 4.10 The 8-element UCA model composed of semi-omnidirectional antennas. 53

Figure 4.11 The azimuth performance of the conventional calibration approach where a single $\mathbf{C}$ matrix is used for the whole azimuth plane. 54

Figure 4.12 The azimuth performance of the sectorized calibration approach combined with MRM where the azimuth plane is divided into 90° wide sectors and a distinct $\mathbf{C}$ matrix is used for each sector. 55

Figure 4.13 The elevation performance of the sectorized calibration approach combined with MRM where the $\mathbf{C}$ matrices found for $\theta = 90°$ are used while the source elevation angle is varied from 75° to 105° with 3 degrees steps. 56

Figure 4.14 The frequency performance of the sectorized calibration approach combined with MRM where the **C** matrices found for 800 MHz are used while the source frequency is varied from 795 MHz to 805 MHz with 250 kHz steps. 57

Figure 5.1 The FEKO model for the 8-element UCA with dipole antennas elevated over a circular PEC plate. 63

Figure 5.2 The FEKO model for the 8-element UCA with monopole antennas attached to a circular PEC plate. 64

Figure 5.3 The MUSIC spectrum of the dipole antenna array calibrated using the composite matrix approach for $(\phi = 70^\circ, \theta = 60^\circ)$ direction. The composite matrices are found by using three non-overlapping azimuth sectors of 120° angular width. 65

Figure 5.4 The MUSIC spectrum of the dipole antenna array calibrated using the composite matrix approach for $(\phi = 70^\circ, \theta = 70^\circ)$ direction. The composite matrices are found by using three non-overlapping azimuth sectors of 120° angular width. 66

Figure 5.5 The MUSIC spectrum of the dipole antenna array calibrated using the composite matrix approach for $(\phi = 70^\circ, \theta = 80^\circ)$ direction. The composite matrices are found by using three non-overlapping azimuth sectors of 120° angular width. 66

Figure 5.6 The azimuth performance of the dipole antenna array calibrated using the composite matrix approach for $\theta = 60^\circ$. The calibration is done by using three non-overlapping azimuth sectors of 120° angular width. . . 67

Figure 5.7 The azimuth performance of the dipole antenna array calibrated using the composite matrix approach for $\theta = 70^\circ$. The calibration is done by using three non-overlapping azimuth sectors of 120° angular width. . . 68

Figure 5.8 The azimuth performance of the dipole antenna array calibrated using the composite matrix approach for $\theta = 80^\circ$. The calibration is done by using three non-overlapping azimuth sectors of 120° angular width. . . 68

Figure 5.9 The MUSIC spectrum of the monopole antenna array calibrated using the composite matrix approach for ($\phi = 80°, \theta = 60°$) direction. The composite matrices are found by using four non-overlapping azimuth sectors of 90° angular width. 69

Figure 5.10 The MUSIC spectrum of the monopole antenna array calibrated using the composite matrix approach for ($\phi = 80°, \theta = 70°$) direction. The composite matrices are found by using four non-overlapping azimuth sectors of 90° angular width. 70

Figure 5.11 The MUSIC spectrum of the monopole antenna array calibrated using the composite matrix approach for ($\phi = 80°, \theta = 80°$) direction. The composite matrices are found by using four non-overlapping azimuth sectors of 90° angular width. 70

Figure 5.12 The azimuth performance of the monopole antenna array calibrated using the composite matrix approach for $\theta = 60°$. The calibration is done by using four non-overlapping azimuth sectors of 90° angular width. 71

Figure 5.13 The azimuth performance of the monopole antenna array calibrated using the composite matrix approach for $\theta = 70°$. The calibration is done by using four non-overlapping azimuth sectors of 90° angular width. 72

Figure 5.14 The azimuth performance of the monopole antenna array calibrated using the composite matrix approach for $\theta = 80°$. The calibration is done by using four non-overlapping azimuth sectors of 90° angular width. 72

Figure 5.15 The elevation performance of the dipole antenna array calibrated using the composite matrix approach. The composite matrices found for $\theta = 70°$ are used while the elevation angle is swept from 68° to 72° with 0.25 degree steps. 73

Figure 5.16 The elevation performance of the monopole antenna array calibrated using the composite matrix approach. The composite matrices found for $\theta = 70°$ are used while the elevation angle is swept from 68° to 72° with 0.25 degree steps. 74

Figure 5.17 The frequency performance of the dipole antenna array calibrated using the composite matrix approach. The composite matrices found for f = 1000 MHz are used while the source frequency is swept from 995 MHz to 1005 MHz with 0.25 MHz steps. 75

Figure 5.18 The frequency performance of the monopole antenna array calibrated using the composite matrix approach. The composite matrices found for f = 1000 MHz are used while the source frequency is swept from 995 MHz to 1005 MHz with 0.25 MHz steps. 76

CHAPTER 1

INTRODUCTION

Since the advent of wireless communication, direction-of-arrival (DOA) estimation applications became one of the most appealing topics among the researchers. There are different kinds of DOA estimation techniques which depend on processing the signals acquired by an antenna array. There are many factors distorting the received signal in an antenna array, such as antenna misplacements, mismatches in cable lengths, mutual coupling between antennas or gain/phase mismatches due to antenna radiation patterns.

When an antenna array is excited by an external source, each array element is subject to the scattering and re-radiation effects coming from the other array elements. These interactions between the array elements is referred as *mutual coupling*. In this respect, mutual coupling represents one of the most important distortion sources given an ideal array model. Super-resolution DOA algorithms, such as Multiple Signal Classification (MUSIC) algorithm [1], use the ideal array model and orthogonality of subspaces to determine the DOA angle. In these algorithms, it is assumed that the measurements are independently taken from the antenna elements which corresponds to neglecting the mutual coupling effect. Therefore, such algorithms require accurate identification and calibration of mutual coupling for an acceptable DOA performance.

Several methods have been proposed to characterize the mutual coupling effect [2]. One of the earliest methods is suggested by Gupta and Ksienski [3]. This method is called as *the open-circuit method*. It treats the N-element array as an $(N+1)$-terminal, bilateral network and relates the antenna terminal voltages to the open-circuit voltages through an impedance matrix composed of mutual impedances. The

open-circuit method is a widely accepted method for mutual coupling analysis because of its familiar concepts depending on the circuit theory. However, it can not completely model the effect of mutual coupling since it does not take into account the scattering effect due to the presence of other antenna elements [4]. In [5, 6], a new mutual impedance calculation technique considering the receiving characteristics of arrays is proposed to overcome the problems of the open-circuit method. This method is further developed in [7] by taking into account all the array elements simultaneously.

In [8], Yamada et. al improved the circuit equation proposed in [3]. In the Yamada's method, two types of mutual impedances are defined, namely, the transmission mutual impedance and the re-radiation mutual impedance. In this context, it is proposed that the re-radiation mutual impedances should be used for mutual coupling calibration. In order to find the re-radiation mutual impedances, each antenna is excited by an external voltage source, and the resulting set of N^2 simultaneous equations is solved. In [9], Sato and Kohno improved the circuit equation further where the case of a receiving array is distinguished from the case of a transmitting array. In both cases, impedance matrix due to re-radiating current distribution is separated from the matrices due to the transmitting or receiving current distributions. Accordingly, two different calibration matrices are proposed for the cases of receiving and transmitting arrays.

In addition to the methods based on mutual impedance calculation, there are also transfer function based methods in the literature such as [10]. In these methods, ideal array data is related to the measured array data without using any physical concept such as mutual impedance. In this thesis, a similar *transformation approach* is presented for mutual coupling identification where the ideal and the measured array data are related through a linear transformation. While the transformation approach has certain similarities with the method in [7], it is easier to comprehend and implement. Furthermore, a new approach is presented in order to decrease the number of calibration measurements required for the transformation approach [11]. This new method is called as *the measurement reduction method (MRM)* which uses the symmetry planes in the array geometry and generates multiple array data from a single measured array data through simple data permutations. MRM is initially proposed for arrays with identical and omnidirectional antenna elements, and a significant degradation

is achieved in the number of calibration measurements. It is shown that a single measurement is sufficient for the calibration of uniform circular arrays (UCA) when MRM is used. MRM simplifies the manual labour in the calibration process which also leads to further degradation in time and cost. It can be applied to any array that has symmetry planes in its geometry. It is shown that many of the well-known array forms have more than one symmetry plane making them suitable for MRM.

The case of non-omnidirectional (NOD) antennas is also examined under the scope of this thesis. It is shown that a single coupling matrix can not properly model the mutual coupling effect for an NOD antenna array. In this context, *a sectorized approach* is proposed for accurate mutual coupling calibration of NOD antenna arrays. In this approach, calibration is done in angular sectors and a different coupling matrix is found for each sector using the transformation approach. In addition, it is shown that MRM is also applicable to NOD antenna arrays with identical elements if the array has symmetry planes in its geometry.

The perfomance of transformation approach combined with MRM for omnidirectional antenna arrays, and the performance of sectorized approach combined with MRM for NOD antenna arrays are evaluated through DOA estimation simulations using the MUSIC algorithm. The calibration measurements are obtained using the full-wave numerical electromagnetic simulation tool FEKO [12]. The performances of the methods are examined for the changes in source frequency, elevation and azimuth angles.

As a final study, the mutual coupling problem is investigated for the case of antenna arrays over a perfect electric conductor (PEC) plate. In this case, additional disturbance is caused by the reflections from the plate. This distorts the receiving pattern of the antenna array which results in gain/phase mismatches in the antenna elements. In this context, a composite matrix approach is proposed where mutual coupling and gain/phase mismatch are jointly modelled by using a single composite calibration matrix. The composite matrix approach is an extension to the transformation approach where the composite calibration matrix represents a linear transformation between the measured and the ideal array data. In the analysis, identical and omnidirectional antenna elements are considered. Therefore, the mutual coupling effect is direction

independent. However, the gain/phase mismatch has a direction dependent characteristics. Hence, the composite calibration matrix, which is formed by mutual coupling and gain/phase mismatch, is also direction dependent. Therefore, a sectorized approach is followed in the composite matrix approach. The approach is evaluated using a dipole antenna array elevated over a circular PEC plate and a monopole antenna array attached to a circular PEC plate, and the results for the two arrays are compared. The evaluations are carried out to monitor the performance of the approach for the changes in source frquency, azimuth and elevation angles.

1.1 Thesis Organization

In the first chapter, the scope and the organization of the thesis are provided. In the second chapter, a review of the methods for mutual coupling calibration is presented in detail by giving the theories lying behind these methods. In the third chapter, calibration of omnidirectional antennas is considered presenting the transformation approach and the measurement reduction method. Then, NOD antenna elements are considered in the fourth chapter where a sectorized approach is proposed for proper calibration of NOD antenna arrays. In the fifth chapter, calibration of mutual coupling and gain/phase mismatch is investigated for the case of antenna arrays over a PEC plate and a composite matrix approach is proposed. Finally, conclusions are discussed in the sixth and the last chapter of the thesis.

CHAPTER 2

REVIEW OF THE METHODS FOR MUTUAL COUPLING CALIBRATION

Mutual coupling stands for the disturbing effects of scattering and re-radiation from an array element to the other array elements. It is nearly impossible to discard mutual coupling effect by making optimizations in physical factors such as antenna type, array geometry or the operation platform. More or less, any antenna array will be exposed to this effect. The common approach is to properly identify the mutual coupling effect in an antenna array and process the array data to compensate for the mutual coupling. Beacuse of its varying effects, mutual coupling has generated a large volume of research to study its causes and calibration methods. Mutual coupling effects are investigated in a variety of fields including multiple-input multiple-output (MIMO) systems, diversity systems, medical imaging, and sonar and radar systems [13]. Recent developments in small-size radio transceivers demanding small-size antenna arrays increased the importance of analysing the mutual coupling. Throughout the years, many different methods have been proposed to characterize and compansate for mutual coupling. In this chapter, four of these methods will be explained in detail by giving the underlying mathematical models.

2.1 The Open-Circuit Method

The open-circuit method is one of the earliest mutual coupling calibration methods proposed by Gupta and Ksienski [3]. The open-circuit method is a widely accepted method for mutual coupling analysis because of its familiar concepts depending on

the circuit theory. In the method, the antenna terminal voltages are related to the open-circuit voltages through an impedance matrix consisting of antenna mutual impedances. The relation is constituted by treating the N-element antenna array as an $(N+1)$-terminal, bilateral network responding to an outside source as shown in Figure 2.1 [3].

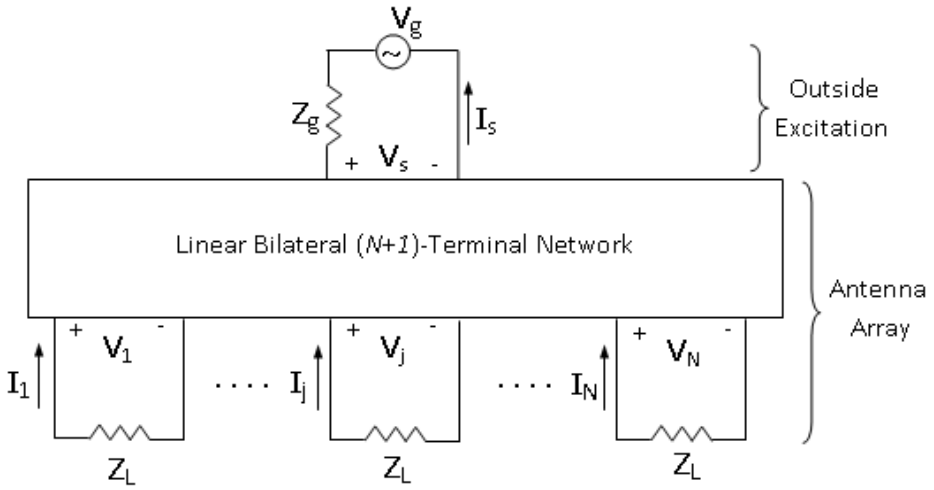

Figure 2.1: The N-element antenna array is treated as an $(N+1)-$terminal network

As shown in Figure 2.1, each antenna is terminated with a known load impedance Z_L, the driving source generator has an open-circuit voltage V_g and internal impedance Z_g. The Kirchoff relation for the $(N+1)$-terminal network can be written as,

$$\begin{aligned}
V_1 &= I_1 Z_{11} + \cdots + I_j Z_{1j} + \cdots + I_N Z_{1N} + I_s Z_{1s} \\
&\vdots \quad \vdots \quad \vdots \quad \vdots \quad \vdots \\
V_j &= I_1 Z_{j1} + \cdots + I_j Z_{jj} + \cdots + I_N Z_{jN} + I_s Z_{js} \\
&\vdots \quad \vdots \quad \vdots \quad \vdots \quad \vdots \\
V_N &= I_1 Z_{N1} + \cdots + I_j Z_{Nj} + \cdots + I_N Z_{NN} + I_s Z_{Ns}
\end{aligned} \tag{2.1}$$

where Z_{ij} represents the mutual impedance between the i^{th} and j^{th} ports (array elements). The relation between terminal current and load impedance is as follows,

$$I_j = -\frac{V_j}{Z_L}, \quad j = 1, 2, \ldots, N \tag{2.2}$$

If all the elements in the array are in an open-circuit condition, then $I_j = 0$, $j =$

$1, 2, \ldots, N$. Inserting this condition into (2.1), we end up with,

$$V_j = V_{OCj} = Z_{js} I_s, \quad j = 1, 2, \ldots, N \tag{2.3}$$

Inserting (2.2) and (2.3) into (2.1), we obtain:

$$\begin{bmatrix} 1 + \frac{Z_{11}}{Z_L} & \frac{Z_{12}}{Z_L} & \cdots & \frac{Z_{1N}}{Z_L} \\ \frac{Z_{21}}{Z_L} & 1 + \frac{Z_{22}}{Z_L} & \cdots & \frac{Z_{2N}}{Z_L} \\ \vdots & \vdots & \ddots & \vdots \\ \frac{Z_{N1}}{Z_L} & \frac{Z_{N2}}{Z_L} & \cdots & 1 + \frac{Z_{NN}}{Z_L} \end{bmatrix} \begin{bmatrix} V_1 \\ V_2 \\ \vdots \\ V_N \end{bmatrix} = \begin{bmatrix} V_{OC1} \\ V_{OC2} \\ \vdots \\ V_{OCN} \end{bmatrix} \tag{2.4}$$

where Z_{ij} $(i, j = 1, 2, \ldots, N)$ are the mutual impedances between the antenna elements and Z_{ii} are the self-impedances of the antennas. The mutual impedances or the self-impedances in (2.4), for example for wire antennas, are defined as [15],

$$Z_{ij} = \frac{V_{OCi}}{I_j(0)} = -\frac{1}{I_i(0) I_j(0)} \int_0^L \mathbf{E}_j(\mathbf{r}) \cdot \mathbf{I}_i(\mathbf{r}) dl \tag{2.5}$$

where $I_i(0)$ is the value of the current distribution $\mathbf{I}_i(\mathbf{r})$ of the i^{th} antenna at the feedpoint (and similarly for $I_j(0)$), $\mathbf{E}_j(\mathbf{r})$ is the radiation electric field at the surface of the i^{th} antenna (with its terminals being shorted) which is generated by the current distribution at the j^{th} antenna, and L is the physical length of the i^{th} antenna. The definition in (2.5) corresponds to a self-impedance if $i = j$ and to a mutual impedance if $i \neq j$. Note that, the current distribution $\mathbf{I}_i(\mathbf{r})$ is obtained by driving the i^{th} antenna in the transmitting mode while terminals of the j^{th} antenna are shorted (and similarly for $\mathbf{I}_j(\mathbf{r})$).

2.2 The Yamada's Method

In [8], Yamada et. al proposed a new circuit equation which is an improved version of the one used in the open-circuit method. In the Yamada's method, two types of

mutual impedances are defined, namely, the transmission mutual impedance (Z_{ij}) and the re-radiation mutual impedance (Z^s_{ij}). Using these two types of mutual impedances, the relation between voltages and currents of antennas for an N-element array can be written as [8],

$$\begin{bmatrix} V_0' \\ V_1' \\ \vdots \\ V_N' \end{bmatrix} = \begin{bmatrix} V_{g0} - Z_L I_0 \\ -Z_L I_1 \\ \vdots \\ -Z_L I_N \end{bmatrix} = \begin{bmatrix} Z_{00} & Z^s_{01} & Z^s_{02} & \cdots & Z^s_{0N} \\ Z_{10} & Z_{11} & Z^s_{12} & \cdots & Z^s_{1N} \\ Z_{20} & Z^s_{21} & Z_{22} & \cdots & Z^s_{2N} \\ \vdots & \vdots & & \ddots & \vdots \\ Z_{N0} & Z^s_{N1} & Z^s_{N2} & \cdots & Z_{NN} \end{bmatrix} \begin{bmatrix} I_0 \\ I_1 \\ \vdots \\ I_N \end{bmatrix} \tag{2.6}$$

where the subindex 0 denotes transmitting antennas and subindices $1, 2, \ldots, N$ represent receiving antennas. Since $-Z_{j0}I_j$ ($j = 1, 2, \ldots, N$) is the (uncoupled) open-circuit voltage of the j^{th} receiving antenna, the relation between the open-circuit voltages ($\mathbf{v}_{open}$) and the (coupled) terminal voltages ($\mathbf{v}$) can be derived as,

$$\mathbf{v}_{open} = \begin{bmatrix} 1 + \frac{Z_{11}}{Z_L} & \frac{Z^s_{12}}{Z_L} & \cdots & \frac{Z^s_{1N}}{Z_L} \\ \frac{Z^s_{21}}{Z_L} & 1 + \frac{Z_{22}}{Z_L} & \cdots & \frac{Z^s_{2N}}{Z_L} \\ \vdots & \vdots & \ddots & \vdots \\ \frac{Z^s_{N1}}{Z_L} & \frac{Z^s_{N2}}{Z_L} & \cdots & 1 + \frac{Z_{NN}}{Z_L} \end{bmatrix} \begin{bmatrix} V_1 \\ V_2 \\ \vdots \\ V_N \end{bmatrix} = \left(\mathbf{I}^N + \frac{1}{Z_L} \mathbf{Z}_s \right) \mathbf{v} = \mathbf{C}^{-1} \mathbf{v} \tag{2.7}$$

where $\mathbf{I}^N$ is the $N \times N$ identity matrix. This equation shows that the re-radiation mutual impedances should be used for mutual coupling calibration. The impedances can be estimated by using the receiving array alone. When each port is excited by V_g separately, the following equation can be obtained,

$$diag\{V_g, V_g, \ldots, V_g\} =$$

$$= (\mathbf{Z}_m + Z_L\mathbf{I}^N) \begin{bmatrix} I_{11} & & 0 \\ & \ddots & \\ 0 & & I_{NN} \end{bmatrix} + (\mathbf{Z}_s + Z_L\mathbf{I}^N) \begin{bmatrix} 0 & I_{12} & \ldots & I_{1N} \\ I_{21} & 0 & & I_{2N} \\ \vdots & & \ddots & \vdots \\ I_{N1} & I_{N2} & \ldots & 0 \end{bmatrix} \quad (2.8)$$

This is a set of N^2 simultaneous equations having N^2 unknowns $(Z_{ii}, Z_{ij}, Z_{ij}^s)$. This set has a solution when N is greater than a certain value which is determined by the array geometry. (For instance, for a uniform linear array, the solution exists for $N > 2$ [8].) After solving this equation set, calibration is done using (2.7).

2.3 The Sato's Method

Sato and Kohno modified the circuit equation where the case of a receiving array is distinguished from the case of a transmitting array [9]. For the case of a transmitting array, the terminal current of the i^{th} antenna is considered to be the sum of the transmitting current I_i^t and the re-radiating (scattering) current I_i^s, i.e.,

$$I_i = I_i^t + I_i^s \quad (2.9)$$

The ideal circuit equation which is free from the mutual coupling effect is,

$$\begin{bmatrix} V_{g1} - Z_L I_1^t \\ V_{g2} - Z_L I_2^t \\ \vdots \\ V_{gN} - Z_L I_N^t \end{bmatrix} = \begin{bmatrix} Z_{in} & & & 0 \\ & Z_{in} & & \\ & & \ddots & \\ 0 & & & Z_{in} \end{bmatrix} \begin{bmatrix} I_1^t \\ I_2^t \\ \vdots \\ I_N^t \end{bmatrix} \quad (2.10)$$

where V_{gi} is the voltage source connected to the i^{th} antenna and Z_{in} is the input impedance of the identical antennas, and all the antennas are terminated with a load impedance Z_L. Since the impedance matrix is diagonal, it is clear that this equation is free from the mutual coupling effect. The proposed circuit equation, which has two terms resulting from the different current distributions, is presented as,

$$\begin{bmatrix} V_{g1} - Z_L(I_1^t + I_1^s) \\ V_{g2} - Z_L(I_2^t + I_2^s) \\ \vdots \\ V_{gN} - Z_L(I_N^t + I_N^s) \end{bmatrix} = \begin{bmatrix} Z_{in} & Z_{12}^t & \cdots & Z_{1N}^t \\ Z_{21}^t & Z_{in} & \ddots & Z_{2N}^t \\ \vdots & \ddots & \ddots & \vdots \\ Z_{N1}^t & Z_{N2}^t & \cdots & Z_{in} \end{bmatrix} \begin{bmatrix} I_1^t \\ I_2^t \\ \vdots \\ I_N^t \end{bmatrix} + \begin{bmatrix} Z_{in} & Z_{12}^s & \cdots & Z_{1N}^s \\ Z_{21}^s & Z_{in} & \ddots & Z_{2N}^s \\ \vdots & \ddots & \ddots & \vdots \\ Z_{N1}^s & Z_{N2}^s & \cdots & Z_{in} \end{bmatrix} \begin{bmatrix} I_1^s \\ I_2^s \\ \vdots \\ I_N^s \end{bmatrix} \tag{2.11}$$

where Z_{ij}^t is defined as the transmitting mutual impedance and Z_{ij}^s as the re-radiating (scattering) mutual impedance between the i^{th} and the j^{th} antennas. If (2.10) is subtracted from (2.11), I_i^s is found as,

$$\begin{bmatrix} I_1^s \\ I_2^s \\ \vdots \\ I_N^s \end{bmatrix} = \begin{bmatrix} 0 & \widetilde{Z}_{12}^t & \cdots & \widetilde{Z}_{1N}^t \\ \widetilde{Z}_{21}^t & 0 & \ddots & \widetilde{Z}_{2N}^t \\ \vdots & \ddots & \ddots & \vdots \\ \widetilde{Z}_{N1}^t & \widetilde{Z}_{N2}^t & \cdots & 0 \end{bmatrix} \begin{bmatrix} I_1^t \\ I_2^t \\ \vdots \\ I_N^t \end{bmatrix} + \begin{bmatrix} 0 & \widetilde{Z}_{12}^s & \cdots & \widetilde{Z}_{1N}^s \\ \widetilde{Z}_{21}^s & 0 & \ddots & \widetilde{Z}_{2N}^s \\ \vdots & \ddots & \ddots & \vdots \\ \widetilde{Z}_{N1}^s & \widetilde{Z}_{N2}^s & \cdots & 0 \end{bmatrix} \begin{bmatrix} I_1^s \\ I_2^s \\ \vdots \\ I_N^s \end{bmatrix} \tag{2.12}$$

where

$$\widetilde{Z}_{ij}^t = -\frac{Z_{ij}^t}{Z_L + Z_{in}}, \qquad \widetilde{Z}_{ij}^s = -\frac{Z_{ij}^s}{Z_L + Z_{in}}. \tag{2.13}$$

Or, more compactly

$$\mathbf{I}^s = \widetilde{\mathbf{Z}}^t \mathbf{I}^t + \widetilde{\mathbf{Z}}^s \mathbf{I}^s \tag{2.14}$$

where $\widetilde{\mathbf{Z}}^t$ is defined as the transmitting mutual coupling matrix and $\widetilde{\mathbf{Z}}^s$ as the re-radiating mutual coupling matrix. Also, the equation in (2.14) is called as the current

coupling equation.

It is desired that the beam pattern is formed in the far-field for the transmitting array. Therefore, the transmitting calibration matrix should be determined by taking into account the influence of both the transmitting and the re-radiating currents in the far-field. In order to fulfill this, the calibration matrix $\mathbf{Z}_c^t$ should satisfy the following conditional equation where the effective weights of the current distributions (X_t, X_s) are considered,

$$\mathbf{Z}_c^t \left(X_t \mathbf{I}^t + X_s \mathbf{I}^s \right) = X_t \mathbf{I}^t \tag{2.15}$$

Combining (2.14) and (2.15), the transmitting calibration matrix is found as,

$$\mathbf{Z}_c^t = \left(\frac{X_s}{X_t} \left(\mathbf{I}^N - \widetilde{\mathbf{Z}}^s \right)^{-1} \widetilde{\mathbf{Z}}^t + \mathbf{I}^N \right)^{-1} \tag{2.16}$$

where $\mathbf{I}^N$ is the $N \times N$ identitiy matrix.

In the case of a receiving array, the receiving calibration matrix is obtained by a similar procedure as in the case of a transmitting array. The current coupling equation in the receiving case is,

$$\mathbf{I}^s = \widetilde{\mathbf{Z}}^r \mathbf{I}^r + \widetilde{\mathbf{Z}}^s \mathbf{I}^s \tag{2.17}$$

where $\mathbf{I}^r$ is the vector composed of receiving currents at the antenna terminals and $\widetilde{\mathbf{Z}}^r$ is the receiving mutual coupling matrix. Note that the receiving mutual coupling matrix is nearly equal to the re-radiating mutual coupling matrix if the interelement spacing is larger than quarter wavelength when the half wavelength dipole antenna array is used. This is due to the reduction of near field effect resulting from the re-radiating current. Accordingly, the receiving mutual coupling matrix is approximated by the re-radiating mutual coupling matrix, i.e.,

$$\widetilde{\mathbf{Z}}^r \approx \widetilde{\mathbf{Z}}^s \tag{2.18}$$

In contrast to the transmitting case, the receiving calibration is simply a matter of controlling the current of the antenna terminals directly. The conditional equation is expressed as,

$$\mathbf{Z}_c^r \ (\mathbf{I}^r + \mathbf{I}^s) = \mathbf{I}^r \tag{2.19}$$

When (2.17) and (2.18) are inserted into (2.19), the receiving calibration matrix is obtained as,

$$\mathbf{Z}_c^r = \left(\left(\mathbf{I}^N - \widetilde{\mathbf{Z}}^s \right)^{-1} \widetilde{\mathbf{Z}}^s + \mathbf{I}^N \right)^{-1} \tag{2.20}$$

As seen in (2.16) and (2.20), the calibration matrices can be found if the effective weights, X_t and X_s, and the mutual coupling matrices, $\widetilde{\mathbf{Z}}^t$ and $\widetilde{\mathbf{Z}}^s$, are known. The proposed method does not measure the far-field electrical field. Therefore, the component of the current coupling matrix that is calculated above is used as an approximated value. As the distance between antenna elements gets larger, the approximated value becomes more accurate. Then, the top right (or bottom left) component of the impedance matrix can be used as effective weights, i.e.,

$$\begin{aligned} X_t &= \widetilde{\mathbf{Z}}^t_{1N} = \widetilde{\mathbf{Z}}^t_{N1} \\ X_s &= \widetilde{\mathbf{Z}}^s_{1N} = \widetilde{\mathbf{Z}}^s_{N1} \end{aligned} \tag{2.21}$$

In order to find the coupling matrices, one antenna is excited by connecting a constant-voltage source and the terminal currents of all the antennas are measured. The same procedure is repeated for all the antennas. Then, the measured terminal currents are substituted into the left-hand side of the following extended current coupling equations derived from (2.9) and (2.14) as,

$$\left(\mathbf{I}^N - \widetilde{\mathbf{Z}}^s \right) [\mathbf{I}_1 \ \mathbf{I}_2 \dots \mathbf{I}_N] = \left(\widetilde{\mathbf{Z}}^t - \widetilde{\mathbf{Z}}^s + \mathbf{I}^N \right) diag \left(I_1^t, I_2^t, \dots, I_N^t \right) \tag{2.22}$$

where $\mathbf{I}_i$ is the vector of measured currents when the i^{th} antenna is excited. Note that, all the amount of radiating current are assumed to be the same, i.e., $I_1^t = I_2^t = \dots = I_N^t$.

As seen in (2.22), the Sato's Method also ends up with a set of N^2 simultaneous equations having N^2 unknowns similar to the Yamada's Method. This set has a solution when N is greater than a certain value which is determined by the array geometry. (For instance, for a uniform linear array, the solution exists for $N > 2$ [9].) After solving this equation set, calibration matrices can be found by using (2.16) and (2.20).

2.4 The Hui's Method

A new method using the receiving characteristics of the antenna array for finding the so-called receiving mutual impedances is proposed by Hui in [5, 6]. The receiving mutual impedances are found by considering the antennas in pairs. This method is further developed in [7] by taking into account all the array elements simultaneously to find the receiving mutual impedances. The new version of the method proposed in [7] is presented below.

Consider an antenna array with N elements where each antenna is terminated with a load impedance Z_L. As shown in [6], the receiving mutual impedance between the k^{th} and the i^{th} antennas is defined as,

$$Z^{ki} = \frac{V_c^{ki}}{I_i} \tag{2.23}$$

where V_c^{ki} is the coupled voltage across the terminal load of the k^{th} antenna due to the current on the i^{th} antenna (terminal value, $I_i = V_i/Z_L$).

When the array is excited by a plane wave coming from a direction of ϕ_1, the received voltage $V_k^{\phi_1}$ at the terminal of the k^{th} antenna can be expressed as,

$$V_k^{\phi_1} = U_k^{\phi_1} + V_c^{k1} + V_c^{k2} + \cdots + V_c^{k(k-1)} + V_c^{k(k+1)} + \cdots + V_c^{kN} \tag{2.24}$$

where $U_k^{\phi_1}$ is the received voltage on the k^{th} antenna due to the plane wave only. Using the definition of the receiving mutual impedance given in (2.23), the received voltage in (2.24) can be written as,

$$V_k^{\phi_1} = U_k^{\phi_1} + Z_t^{k1} I_1^{\phi_1} + Z_t^{k2} I_2^{\phi_1} + \cdots + Z_t^{k(k-1)} I_{k-1}^{\phi_1} + Z_t^{k(k+1)} I_{k+1}^{\phi_1} + \cdots + Z_t^{kN} I_N^{\phi_1} \quad (2.25)$$

Since the terminal value of the current on the i^{th} antenna ($I_i^{\phi_1} = V_i^{\phi_1}/Z_L$) is used, (2.25) can be rewritten as,

$$\begin{aligned} V_k^{\phi_1} - U_k^{\phi_1} = Z_t^{k1}\frac{V_1^{\phi_1}}{Z_L} + Z_t^{k2}\frac{V_2^{\phi_1}}{Z_L} + \cdots + Z_t^{k(k-1)}\frac{V_{k-1}^{\phi_1}}{Z_L} \\ + Z_t^{k(k+1)}\frac{V_{k+1}^{\phi_1}}{Z_L} + \cdots + Z_t^{kN}\frac{V_N^{\phi_1}}{Z_L} \end{aligned} \quad (2.26)$$

In general, the receiving mutual impedances Z_t^{ki} of an antenna array change with the source direction. However, the receiving mutual impedances do not change with the source direction for omnidirectional antennas. On the other hand, $V_k^{\phi_1}$ and $U_k^{\phi_1}$ are both functions of the source direction. Using this fact, many equations like (2.26) can be generated for different source directions. Putting these equations into a matrix form, we have the following system of equations for L plane wave directions,

$$\begin{bmatrix} V_k^{\phi_1} - U_k^{\phi_1} \\ V_k^{\phi_2} - U_k^{\phi_2} \\ \vdots \\ V_k^{\phi_{L-1}} - U_k^{\phi_{L-1}} \\ V_k^{\phi_L} - U_k^{\phi_L} \end{bmatrix}$$

$$= \begin{bmatrix} \frac{V_1^{\phi_1}}{Z_L} & \cdots & \frac{V_{k-1}^{\phi_1}}{Z_L} & \frac{V_{k+1}^{\phi_1}}{Z_L} & \cdots & \frac{V_N^{\phi_1}}{Z_L} \\ \frac{V_1^{\phi_2}}{Z_L} & \cdots & \frac{V_{k-1}^{\phi_2}}{Z_L} & \frac{V_{k+1}^{\phi_2}}{Z_L} & \cdots & \frac{V_N^{\phi_2}}{Z_L} \\ \vdots & \ddots & \vdots & \vdots & \ddots & \vdots \\ \frac{V_1^{\phi_{L-1}}}{Z_L} & \cdots & \frac{V_{k-1}^{\phi_{L-1}}}{Z_L} & \frac{V_{k+1}^{\phi_{L-1}}}{Z_L} & \cdots & \frac{V_N^{\phi_{L-1}}}{Z_L} \\ \frac{V_1^{\phi_L}}{Z_L} & \cdots & \frac{V_{k-1}^{\phi_L}}{Z_L} & \frac{V_{k+1}^{\phi_L}}{Z_L} & \cdots & \frac{V_N^{\phi_L}}{Z_L} \end{bmatrix} \begin{bmatrix} Z^{k1} \\ \vdots \\ Z^{k(k-1)} \\ Z^{k(k+1)} \\ \vdots \\ Z^{kN} \end{bmatrix} \quad (2.27)$$

(2.27) has a solution for $L \geq N-1$. When (2.27) is solved, mutual impedances between the k^{th} antenna and the other antennas, i.e. $(Z^{k1}, \ldots, Z^{k(k-1)}, Z^{k(k+1)}, \ldots, Z^{kN})$, are found in a single step. If this procedure is repeated for each antenna element, all the

mutual impedances between all the antenna elements are obtained. Then, the $N \times N$ mutual impedance matrix, $\mathbf{Z}$, can be constructed as [2],

$$\mathbf{Z} = \begin{bmatrix} 1 & -\frac{Z^{12}}{Z_L} & \cdots & -\frac{Z^{1N}}{Z_L} \\ -\frac{Z^{21}}{Z_L} & 1 & \cdots & -\frac{Z^{2N}}{Z_L} \\ \vdots & \vdots & \ddots & \vdots \\ -\frac{Z^{N1}}{Z_L} & -\frac{Z^{N2}}{Z_L} & \cdots & 1 \end{bmatrix} \tag{2.28}$$

Then, the relation between the coupled voltages $(V_1, V_2, \ldots, V_N)$ and the uncoupled voltages $(U_1, U_2, \ldots, U_N)$ is given as [2],

$$\begin{bmatrix} 1 & -\frac{Z^{12}}{Z_L} & \cdots & -\frac{Z^{1N}}{Z_L} \\ -\frac{Z^{21}}{Z_L} & 1 & \cdots & -\frac{Z^{2N}}{Z_L} \\ \vdots & \vdots & \ddots & \vdots \\ -\frac{Z^{N1}}{Z_L} & -\frac{Z^{N2}}{Z_L} & \cdots & 1 \end{bmatrix} \begin{bmatrix} V_1 \\ V_2 \\ \vdots \\ V_N \end{bmatrix} = \begin{bmatrix} U_1 \\ U_2 \\ \vdots \\ U_N \end{bmatrix} \tag{2.29}$$

Finally, the mutual coupling matrix, $\mathbf{C}$, can be found as the inverse of the mutual impedance matrix, $\mathbf{Z}$, i.e.,

$$\mathbf{C} = \mathbf{Z}^{-1} \tag{2.30}$$

The four methods investigated in this chapter, the open-circuit method, the Hui's method, the Yamada's method and the Sato's method, are compared in [14]. In this comparison, a linear dipole antenna array is used and the detection of vertical and horizontal polarized incoming signals is considered. The methods are evaluated over the DOA estimation accuracies using the MUSIC algorithm. The results show that the Hui's method provides a better mutual coupling calibration for DOA estimation than the remaining three methods.

CHAPTER 3

MUTUAL COUPLING CALIBRATION OF OMNIDIRECTIONAL ANTENNA ARRAYS

In the previous chapter, some of the existing mutual coupling calibration methods are explained in detail. All of these methods consider arrays composed of omnidirectional antennas. In this chapter, first, a linear transformation approach similar to [10] is presented for mutual coupling calibration [11]. In the transformation approach, the ideal array data is related to the measured array data through a linear transformation. The linear set of equations used in the approach is similar to the one in [7]. However, the transformation approach is easier to comprehend and implement, and computationally more efficient.

Next, a new method is presented in order to decrease the number of measurements required for mutual coupling calibration of omnidirectional antenna arrays using the transformation approach. The method is called as *the measurement reduction method (MRM)* [11]. MRM is based on the symmetry planes in the array geometry. The idea is to use a single measurement in order to generate multiple measurements through simple data permutations. Here, a measurement corresponds to an array output observation for a given calibration angle.

Before presenting these two novel methods, it is convenient to give the signal model used in the course of this chapter.

3.1 Signal Model

In this chapter, antenna arrays composed of identical and omnidirectional elements are considered in a noise-free environment, and narrowband model is used. The output vector for an N-element antenna array is given as,

$$\mathbf{y}(t) = \mathbf{C}\ \mathbf{A}\ \mathbf{s}(t), \qquad t = 1, 2, \ldots, P \tag{3.1}$$

where P is the number of snapshots and $\mathbf{C}$ is the $N \times N$ mutual coupling matrix. Columns of the steering matrix $\mathbf{A}$ are the steering vectors for L excitation sources coming from distinct azimuth, ϕ_l, and elevation, θ_l, angles, i.e. $\mathbf{A} = [\mathbf{a}(\phi_1, \theta_1)\ \ \mathbf{a}(\phi_2, \theta_2) \ldots \mathbf{a}(\phi_L, \theta_L)]$. The steering vector for the excitation source coming from (ϕ_l, θ_l) direction is $\mathbf{a}(\phi_l, \theta_l) = [\alpha_1(\phi_l, \theta_l)\ \ \alpha_2(\phi_l, \theta_l) \ldots \alpha_N(\phi_l, \theta_l)]^T$ where $(\cdot)^T$ denotes transposition. The vector element corresponding to the n^{th} antenna positioned at (x_n, y_n, z_n) is $\alpha_n(\phi_l, \theta_l) = e^{j\frac{2\pi}{\lambda}(x_n \cos\phi_l \sin\theta_l + y_n \sin\phi_l \sin\theta_l + z_n \cos\theta_l)}$. $\mathbf{s}(t) = [s_1(t)\ \ s_2(t) \ldots s_L(t)]^T$ is the signal vector that consists of the complex amplitudes of L single excitation sources.

Note that, since the arrays composed of omnidirectional and identical antennas are considered, the mutual coupling matrix, $\mathbf{C}$, is independent of the azimuth angle [16]. In this case, the MUSIC algorithm estimates the DOA angles as the maxima of the following spectrum,

$$P_{MU}(\phi, \theta) = \frac{1}{\mathbf{a}^H(\phi, \theta)\ \mathbf{C}^H\ \mathbf{E}_N\ \mathbf{E}_N^H\ \mathbf{C}\ \mathbf{a}(\phi, \theta)} \tag{3.2}$$

where $(\cdot)^H$ denotes the complex conjugate transposition and $\mathbf{E}_N$ is the matrix whose columns are the noise eigenvectors obtained from the singular value decomposition of the sample correlation matrix, $\hat{\mathbf{R}} = \dfrac{1}{P}\displaystyle\sum_{t=1}^{P} \mathbf{y}(t)\mathbf{y}^H(t)$. As it is evident from (3.2), $\mathbf{C}$ should be known for accurate DOA estimation.

3.2 Transformation Approach

The concept of antenna mutual impedances is commonly used to characterize the mutual coupling effect in antenna arrays [3, 5, 6, 7]. However, it is also possible to characterize the mutual coupling effect through a linear transformation without using any physical definitions like mutual impedance. In this part, a transformation approach for mutual coupling calibration is presented.

In most of the methods analyzing the mutual coupling effect, the main issue is to set up a relation between the data measured from antenna terminals (voltage and/or current) and another data that is assumed to be free from mutual coupling. When voltage is used as the data to be processed, it is a convenient way to refer the former as *the coupled voltage* and the latter as *the uncoupled voltage*.

Consider an arbitrary N-element antenna array with element indices of $n = 1, 2, \ldots, N$. Then, the coupled and the uncoupled voltages for the n^{th} antenna due to a single excitation source coming from (ϕ_1, θ_1) direction are denoted as $V_n(\phi_1, \theta_1)$ and $U_n(\phi_1, \theta_1)$, respectively. The coupled voltage vector,

$$\mathbf{v}(\phi_1, \theta_1) = [V_1(\phi_1, \theta_1)\ V_2(\phi_1, \theta_1)\ \ \ldots\ \ V_N(\phi_1, \theta_1)]^T \tag{3.3}$$

is obtained with a single measurement when all the antennas are residing in the array. The uncoupled voltage vector,

$$\mathbf{u}(\phi_1, \theta_1) = [U_1(\phi_1, \theta_1)\ U_2(\phi_1, \theta_1)\ \ \ldots\ \ U_N(\phi_1, \theta_1)]^T \tag{3.4}$$

is obtained with N measurements each of which is taken on a single antenna while all the remaining antennas are removed. Hence, there is no mutual coupling effect during the measurements for the uncoupled voltage vector.

Let us recall the calibration equation of the Hui's method given in (2.29) using our new notation,

$$\begin{bmatrix} 1 & -\frac{Z^{12}}{Z_L} & \cdots & -\frac{Z^{1N}}{Z_L} \\ -\frac{Z^{21}}{Z_L} & 1 & \cdots & -\frac{Z^{2N}}{Z_L} \\ \vdots & \vdots & \ddots & \vdots \\ -\frac{Z^{N1}}{Z_L} & -\frac{Z^{N2}}{Z_L} & \cdots & 1 \end{bmatrix} \begin{bmatrix} V_1(\phi_1,\theta_1) \\ V_2(\phi_1,\theta_1) \\ \vdots \\ V_N(\phi_1,\theta_1) \end{bmatrix} = \begin{bmatrix} U_1(\phi_1,\theta_1) \\ U_2(\phi_1,\theta_1) \\ \vdots \\ U_N(\phi_1,\theta_1) \end{bmatrix} \tag{3.5}$$

Or, more compactly,

$$\mathbf{Z}\ \mathbf{v}(\phi_1,\theta_1) = \mathbf{u}(\phi_1,\theta_1) \tag{3.6}$$

The target in array calibration is to find the coupling matrix, $\mathbf{C}$, which is defined as the inverse of the mutual impedance matrix, $\mathbf{Z}$, i.e. $\mathbf{C} = \mathbf{Z}^{-1}$. In [7], each row of $\mathbf{Z}$ except the diagonal element is separately calculated by using a matrix inversion each time. While the approach in [7] is effective, it is possible to use an alternative approach. In the new transformation approach, it is proposed that the uncoupled voltage at the n^{th} antenna can be expressed as a linear combination of the coupled voltages as,

$$U_n(\phi_1,\theta_1) = t_{n1}V_1(\phi_1,\theta_1) + t_{n2}V_2(\phi_1,\theta_1) + \cdots + t_{nN}V_N(\phi_1,\theta_1) \tag{3.7}$$

where t_{nm} $(n,m = 1,2,\ldots,N)$ are the transformation coefficients. If (3.7) is written for all antenna elements and put in a matrix form, we obtain,

$$\begin{bmatrix} t_{11} & t_{12} & \ldots & t_{1N} \\ t_{21} & t_{22} & \ldots & t_{2N} \\ \vdots & \vdots & \ddots & \vdots \\ t_{N1} & t_{N2} & \ldots & t_{NN} \end{bmatrix} \begin{bmatrix} V_1(\phi_1,\theta_1) \\ V_2(\phi_1,\theta_1) \\ \vdots \\ V_N(\phi_1,\theta_1) \end{bmatrix} = \begin{bmatrix} U_1(\phi_1,\theta_1) \\ U_2(\phi_1,\theta_1) \\ \vdots \\ U_N(\phi_1,\theta_1) \end{bmatrix} \tag{3.8}$$

Or, more compactly,

$$\mathbf{T}\ \mathbf{v}(\phi_1,\theta_1) = \mathbf{u}(\phi_1,\theta_1) \tag{3.9}$$

where $\mathbf{T}$ is the $N \times N$ transformation matrix. As seen in (3.6) and (3.9), both $\mathbf{Z}$ and $\mathbf{T}$ appear in the same equation. The main difference between these two matrices is that $\mathbf{Z}$ has a special structure with ones in its diagonal as shown in (3.5) whereas $\mathbf{T}$ does not have a special structure and can be obtained directly as a least-squares solution. The mutual coupling matrix, $\mathbf{C}$, is independent of the azimuth angle for an array with omnidirectional and identical antennas [16]. This is verified through the simulation results. On the other hand, $\mathbf{C}$ depends on the operating frequency, and this dependency is also elaborated through the simulation results.

Additional observations are required to solve for the $N \times N$ transformation matrix, $\mathbf{T}$. Let $\mathbf{V} = [\mathbf{v}(\phi_1, \theta_1)\ \mathbf{v}(\phi_2, \theta_2)\ \ldots\ \mathbf{v}(\phi_L, \theta_L)]$ and $\mathbf{U} = [\mathbf{u}(\phi_1, \theta_1)\ \mathbf{u}(\phi_2, \theta_2)\ \ldots\ \mathbf{u}(\phi_L, \theta_L)]$ be $N \times L$ matrices whose columns are the coupled and the uncoupled voltage vectors due to L single excitation sources coming from distinct directions. Then, (3.9) can be extended as,

$$\mathbf{T}\,\mathbf{V} = \mathbf{U} \tag{3.10}$$

Assuming $L \geq N$, the transformation matrix, $\mathbf{T}$, can be found as,

$$\mathbf{T} = \mathbf{U}\,\mathbf{V}^{\dagger} \tag{3.11}$$

where $(\cdot)^{\dagger}$ denotes the Moore-Penrose pseudo inverse. Note that a single matrix inversion is sufficient to calculate $\mathbf{T}$ whereas N matrix inversions are needed to calculate $\mathbf{Z}$ [7]. Therefore, the transformation approach provides a significant reduction in computational complexity. In addition to its efficiency in computation, convenience in comprehension and implementation are the basic advantages.

The implementation of the transformation approach for an N-element array can be summarized as follows:

1. Obtain the coupled voltage vector $\mathbf{v}(\phi_1, \theta_1)$ with a single measurement when all the antennas are residing. Also, obtain the uncoupled voltage vector $\mathbf{u}(\phi_1, \theta_1)$ with N measurements each time when a single antenna is residing.

2. Repeat the first step $L \geq N$ times using a single excitation source coming from a distinct direction each time, and obtain $\mathbf{V} = [\mathbf{v}(\phi_1, \theta_1)\ \mathbf{v}(\phi_2, \theta_2)\ \ldots\ \mathbf{v}(\phi_L, \theta_L)]$ and $\mathbf{U} = [\mathbf{u}(\phi_1, \theta_1)\ \mathbf{u}(\phi_2, \theta_2)\ \ldots\ \mathbf{u}(\phi_L, \theta_L)]$.

3. Use (3.11) to find $\mathbf{T}$, and $\mathbf{C}$ is found as the inverse of $\mathbf{T}$.

The diagonal elements of $\mathbf{T}$ are not exactly one as in $\mathbf{Z}$, but the simulation results show that the difference is very small and can easily be ignored. It turns out that the difference between $\mathbf{T}$ and $\mathbf{Z}$ is numerically very small and they almost result the same mutual coupling matrix, $\mathbf{C}$. For an N-element array, at least $(N-1) \times (N+1)$ measurements are needed in order to find $\mathbf{Z}$ ($L = N-1$) [7] whereas at least $N \times (N+1)$ measurements are required in order to find $\mathbf{T}$ ($L = N$). In the following part, MRM is presented in order to decrease the number of required measurements significantly.

3.3 Measurement Reduction Method

In this part, the measurement reduction method (MRM) is presented for arrays with omnidirectional and identical elements in order to decrease the number of measurements during the calibration procedure. This method is based on the fact that certain measurements repeat themselves with permutations in the observed data vector. This is due to the symmetry in the array geometry. MRM has distinct advantages compared to the conventional calibration approaches. The required manual labour for the calibration process is decreased as well as the time and the cost.

Consider an array which is composed of N omnidirectional and identical antennas with the array model given in (3.1). Then, the uncoupled voltage vectors are the same as the steering vectors up to a complex scaling factor β, i.e.,

$$\mathbf{u}(\phi_l, \theta_l) = \beta\, \mathbf{a}(\phi_l, \theta_l), \quad l = 1, 2, \ldots, L \tag{3.12}$$

Therefore, the steering matrix, $\mathbf{A}$, can be used instead of the uncoupled voltage matrix, $\mathbf{U}$, in order to find $\mathbf{T}$ as,

$$\mathbf{T} = \mathbf{A}\ \mathbf{V}^{\dagger} \tag{3.13}$$

Hence, there is no need to have measurements for **U** and it is sufficient to obtain only the measurements for **V**. In the following part, it is presented how to further decrease the measurements for **V** using MRM. This presentation uses the uncoupled voltages while the same results are validated for the coupled voltages.

Lemma 1: Assume that an arbitrary array with a symmetry plane s_1 is given. The array is composed of omnidirectional and identical elements. Let $U_1(\phi_1, \theta_1)$ be the uncoupled voltage measured at the array element e_1 due to a single excitation source coming from (ϕ_1, θ_1) direction. Similarly, let $U_2(\phi_2, \theta_2)$ be the uncoupled voltage measured at the array element e_2 due to a single excitation source coming from (ϕ_2, θ_2) direction. If the array elements e_1, e_2 and the directions (ϕ_1, θ_1), (ϕ_2, θ_2) are symmetrical to each other with respect to the symmetry plane s_1, then $U_1(\phi_1, \theta_1) = U_2(\phi_2, \theta_2)$.

Proof 1: In Figure 3.1, the geometry of the problem is presented where e_1 and e_2 are located at (x_1, y_1, z_1) and (x_2, y_2, z_2) respectively. The uncoupled voltages and the corresponding steering vector elements are equal up to a scaling factor β by (3.12),

$$\begin{aligned} U_1(\phi_1, \theta_1) &= \beta\ \alpha_1(\phi_1, \theta_1) \\ U_2(\phi_2, \theta_2) &= \beta\ \alpha_2(\phi_2, \theta_2) \end{aligned} \tag{3.14}$$

The steering vector elements in (3.14) are,

$$\begin{aligned} \alpha_1(\phi_1, \theta_1) &= e^{j\frac{2\pi}{\lambda}(x_1 \cos\phi_1 \sin\theta_1 + y_1 \sin\phi_1 \sin\theta_1 + z_1 \cos\theta_1)} \\ \alpha_2(\phi_2, \theta_2) &= e^{j\frac{2\pi}{\lambda}(x_2 \cos\phi_2 \sin\theta_2 + y_2 \sin\phi_2 \sin\theta_2 + z_2 \cos\theta_2)} \end{aligned} \tag{3.15}$$

As seen in Figure 3.1, the work space can be defined such that the xy-plane is the symmetry plane s_1 without loss of generality. This leads to the following equalities,

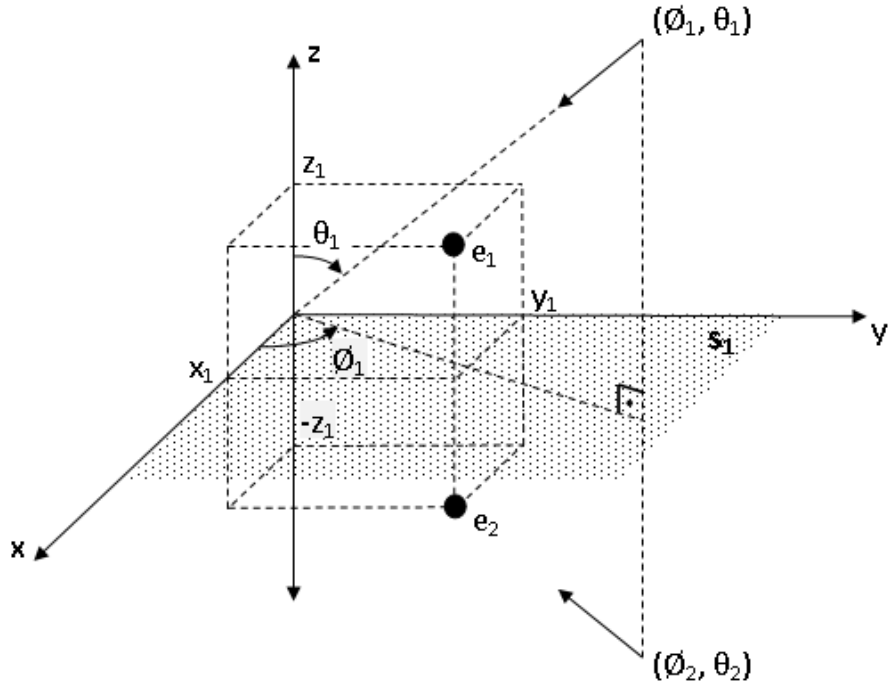

Figure 3.1: The array elements e_1, e_2 and the directions (ϕ_1, θ_1), (ϕ_2, θ_2) are symmetrical to each other with respect to the symmetry plane s_1.

$$\begin{aligned} x_2 &= x_1 \\ y_2 &= y_1 \\ z_2 &= -z_1 \\ \phi_2 &= \phi_1 \\ \theta_2 &= \pi - \theta_1 \end{aligned} \tag{3.16}$$

When (3.16) is inserted into (3.15), the following equations are obtained,

$$\begin{aligned} \alpha_1(\phi_1, \theta_1) &= e^{j\frac{2\pi}{\lambda}(x_1 \cos\phi_1 \sin\theta_1 + y_1 \sin\phi_1 \sin\theta_1 + z_1 \cos\theta_1)} \\ \alpha_2(\phi_2, \theta_2) &= e^{j\frac{2\pi}{\lambda}[x_1 \cos\phi_1 \sin(\pi-\theta_1) + y_1 \sin\phi_1 \sin(\pi-\theta_1) - z_1 \cos(\pi-\theta_1)]} \end{aligned} \tag{3.17}$$

In (3.17), it can be seen that $\alpha_1(\phi_1, \theta_1) = \alpha_2(\phi_2, \theta_2)$. Therefore, $U_1(\phi_1, \theta_1) = U_2(\phi_2, \theta_2)$ by (3.14).

Fact 1: Lemma 1 is presented for the uncoupled voltages. However, a similar fact should be true for the coupled voltages in order to have measurement reduction.

Given an arbitrary array, finding the relation between the coupled voltages through a simple closed form expression is a hard if not an impossible problem. Usually, this problem is solved by using numerical electromagnetic simulation tools as in [7, 14]. In our case, the full-wave numerical electromagnetic simulation tool FEKO [12] is used. Different array types such as uniform circular array (UCA), uniform linear array (ULA), uniform X-shaped array and uniform V-shaped array, are considered and tested. It is found that the coupled voltages also show similar relations as the uncoupled voltages. Therefore, Lemma 1 is valid for the coupled voltages as well, i.e.,

$$V_1(\phi_1, \theta_1) = V_2(\phi_2, \theta_2) \tag{3.18}$$

Lemma 2: Assume that there are S symmetry planes, $s_1, s_2, \ldots, s_S$, in the array geometry. Let $\mathbf{g_1}(\phi_1, \theta_1)$ be a unit direction vector which is not lying on a symmetry plane and $\mathbf{g_2}(\phi_2, \theta_2)$ be its symmetric vector with respect to the symmetry plane s_1. Denote the vectors $[\mathbf{g_1}, \mathbf{g_2}]$ as *a symmetric couple*. Then, there exist S symmetric couples, $[\mathbf{g_i}, \mathbf{g_{i+1}}]$ $(i = 1, 3, \ldots, 2S-1)$, in the array.

Proof 2: In Figure 3.2, the two dimensional geometry of the problem is given for the UCA. Consider the symmetric couple $[\mathbf{g_1}, \mathbf{g_2}]$ whose elements are symmetrical to each other with respect to s_1. There are $S-1$ directions, $\mathbf{g_4}(\phi_4, \theta_4), \mathbf{g_6}(\phi_6, \theta_6), \ldots,$ $\mathbf{g_{2S}}(\phi_{2S}, \theta_{2S})$, which are symmetrical to $\mathbf{g_1}(\phi_1, \theta_1)$ with respect to $s_2, s_3, \ldots, s_S$, respectively. Similarly, there are another $S-1$ directions, $\mathbf{g_3}(\phi_3, \theta_3), \mathbf{g_5}(\phi_5, \theta_5), \ldots,$ $\mathbf{g_{2S-1}}(\phi_{2S-1}, \theta_{2S-1})$, which are symmetrical to $\mathbf{g_2}(\phi_2, \theta_2)$ with respect to $s_2, s_3, \ldots, s_S$, respectively. Then, these $2S-2$ directions constitute $S-1$ symmetric couples, $[\mathbf{g_3}, \mathbf{g_4}]$, $[\mathbf{g_5}, \mathbf{g_6}], \ldots, [\mathbf{g_{2S-1}}, \mathbf{g_{2S}}]$, respectively. Therefore, including $[\mathbf{g_1}, \mathbf{g_2}]$, there exist a total of S symmetric couples in the array.

Lemma 3: Assume that a volumetric array is composed of N omnidirectional and identical elements. Also, assume that there are S symmetry planes, $s_1, s_2, \ldots, s_S$, in the array geometry. Let $\mathbf{g_1}(\phi_1, \theta_1)$ be a unit direction vector which is not lying on a symmetry plane. Let the uncoupled voltage vector $\mathbf{u}(\phi_1, \theta_1)$ be known. Then, $2S-1$ uncoupled voltage vectors, $\mathbf{u}(\phi_2, \theta_2), \mathbf{u}(\phi_3, \theta_3), \ldots, \mathbf{u}(\phi_{2S}, \theta_{2S})$, can be generated from $\mathbf{u}(\phi_1, \theta_1)$ through data permutations.

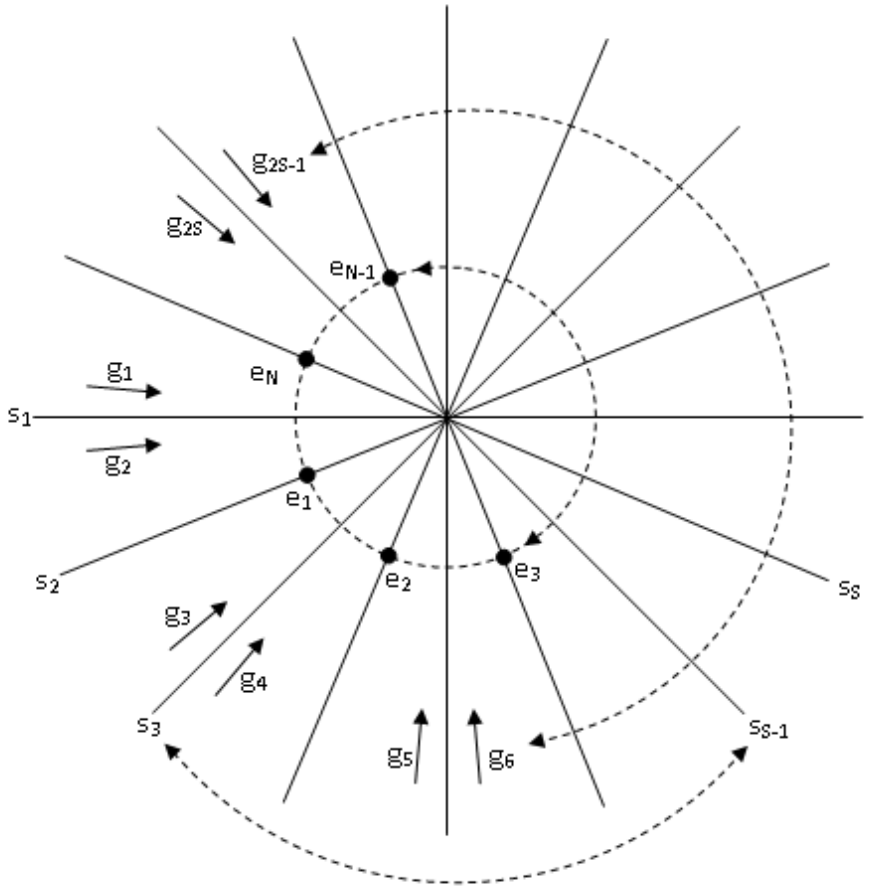

Figure 3.2: Two dimensional geometry of a UCA with N elements, $e_1, e_2, \ldots, e_N$, and S symmetry planes, $s_1, s_2, \ldots, s_S$,. There are S symmetric couples, $[\mathbf{g_i}, \mathbf{g_{i+1}}]$ $(i = 1, 3, \ldots, 2S-1)$, in the array.

Proof 3: Let $\mathbf{g_2}(\phi_2, \theta_2)$ be the direction symmetrical to $\mathbf{g_1}(\phi_1, \theta_1)$ with respect to the symmetry plane s_1. By *Lemma 1*, $U_1(\phi_1, \theta_1) = U_2(\phi_2, \theta_2)$. Since each array element has a symmetric element with respect to s_1, $\mathbf{u}(\phi_2, \theta_2)$ can be generated from $\mathbf{u}(\phi_1, \theta_1)$ through data permutations. By *Lemma 2*, there are $2S$ symmetric directions, $\mathbf{g_1}(\phi_1, \theta_1), \mathbf{g_2}(\phi_2, \theta_2), \ldots, \mathbf{g_{2S}}(\phi_{2S}, \theta_{2S})$, with respect to the S symmetry planes in the array. Then, similar to $\mathbf{u}(\phi_2, \theta_2)$, the uncoupled voltage vectors $\mathbf{u}(\phi_3, \theta_3), \mathbf{u}(\phi_4, \theta_4), \ldots, \mathbf{u}(\phi_{2S}, \theta_{2S})$ can also be generated from $\mathbf{u}(\phi_1, \theta_1)$ through data permutations. Therefore, $2S-1$ uncoupled voltage vectors, $\mathbf{u}(\phi_2, \theta_2), \mathbf{u}(\phi_3, \theta_3), \ldots,$ $\mathbf{u}(\phi_{2S}, \theta_{2S})$, can be generated from $\mathbf{u}(\phi_1, \theta_1)$ through data permutations.

Fact 2: Lemma 3 is given for the uncoupled voltage vectors. In order to identify the characteristics for the coupled voltage vectors, different array types are investigated

through numerical electromagnetic simulations in FEKO. It is found that Lemma 3 is valid for the coupled voltage vectors as well. Therefore, if the coupled voltage vector $\mathbf{v}(\phi_1, \theta_1)$ is known, then $2S-1$ coupled voltage vectors, $\mathbf{v}(\phi_2, \theta_2), \mathbf{v}(\phi_3, \theta_3), \ldots,$ $\mathbf{v}(\phi_{2S}, \theta_{2S})$, can be generated from $\mathbf{v}(\phi_1, \theta_1)$ through data permutations.

MRM is based on Fact 2. The implementation of the method for an N-element array with S symmetry planes can be summarized as follows:

1. Excite the array using a single source coming from (ϕ_1, θ_1) direction which is not lying on a symmetry plane. Obtain the coupled voltage vector $\mathbf{v}(\phi_1, \theta_1)$ with a single measurement when all the antennas are residing.

2. Using Fact 2, generate $\mathbf{v}(\phi_2, \theta_2), \mathbf{v}(\phi_3, \theta_3), \ldots, \mathbf{v}(\phi_{2S}, \theta_{2S})$ from $\mathbf{v}(\phi_1, \theta_1)$ through data permutations. (The source directions, (ϕ_l, θ_l) $(l = 2, 3, \ldots, 2S)$, are obtained using (ϕ_1, θ_1) and the symmetry planes as in Figure 3.2.)

3. Repeat Step-1 and Step-2 $L \geq \lceil \frac{N}{2S} \rceil$ times, each time starting with a single excitation source coming from a direction that is different from all the previously used directions, $(\phi_{2S(l-1)+k}, \theta_{2S(l-1)+k})$, $l = 1, 2, \ldots, L$ and $k = 1, 2, \ldots, 2S$. ($\lceil \cdot \rceil$ denotes the ceiling function.)

4. Use (3.13) to find $\mathbf{T}$, and $\mathbf{C}$ is found as the inverse of $\mathbf{T}$.

Remark 1: When the excitation source direction (ϕ_1, θ_1) lies on a symmetry plane s_1, its symmetric direction with respect to s_1 will be itself. Therefore, there will be no symmetric couples. Hence, the $2S$ symmetric directions in Lemma 2 will reduce to S symmetric directions all of which lie on symmetry planes. Then, it will be possible to generate $S-1$ coupled voltage vectors from $\mathbf{v}(\phi_1, \theta_1)$ through data permutations. In this case, twice the number of measurements will be required. Therefore, it is better to choose the excitation source direction (ϕ_1, θ_1) off the symmetry planes.

The application of the proposed method on a UCA is considered. In Figure 3.2, two dimensional geometry of the application for an N-element UCA with S symmetry planes is presented. As seen in Figure 3.2, $\mathbf{g_1}(\phi_1, \theta_1), \mathbf{g_2}(\phi_2, \theta_2), \ldots, \mathbf{g_{2S}}(\phi_{2S}, \theta_{2S})$ are the $2S$ symmetric directions. Assume that the coupled voltage vector $\mathbf{v}(\phi_1, \theta_1)$ is measured. Then, $\mathbf{v}(\phi_2, \theta_2)$ can be obtained reversing the element order of $\mathbf{v}(\phi_1, \theta_1)$

as,

$$\mathbf{v}(\phi_1,\theta_1) = \begin{bmatrix} V_1(\phi_1,\theta_1) \\ V_2(\phi_1,\theta_1) \\ \vdots \\ V_N(\phi_1,\theta_1) \end{bmatrix}, \quad \mathbf{v}(\phi_2,\theta_2) = \begin{bmatrix} V_N(\phi_1,\theta_1) \\ V_{N-1}(\phi_1,\theta_1) \\ \vdots \\ V_1(\phi_1,\theta_1) \end{bmatrix} \tag{3.19}$$

The coupled voltage vectors $\mathbf{v}(\phi_{2i-1},\theta_{2i-1})$ $(i = 2,3,\ldots,S)$ can be generated from $\mathbf{v}(\phi_1,\theta_1)$ through cyclic shifts in data vectors as i is incremented by one each time. Similarly, $\mathbf{v}(\phi_{2i},\theta_{2i})(i = 2,3,\ldots,S)$ can be generated from $\mathbf{v}(\phi_2,\theta_2)$ through cyclic shifts in data vectors. This correseponds to the following data permutation.

$$\begin{aligned} V_n(\phi_{2i-1},\theta_{2i-1}) &= V_{n'}(\phi_1,\theta_1), \quad \left\{ \begin{array}{l} n' = N \quad ,if \;\; n-i+1 \equiv 0 \;(modN) \\ n' \equiv n-i+1 \;(modN) \quad ,else \end{array} \right\} \\ V_n(\phi_{2i},\theta_{2i}) &= V_{n'}(\phi_1,\theta_1), \qquad \left\{ \begin{array}{l} n' = N \quad ,if \;\; N-n+i \equiv 0 \;(modN) \\ n' \equiv N-n+i \;(modN) \quad ,else \end{array} \right\} \end{aligned} \tag{3.20}$$

where $n, n' = 1,2,\ldots,N$ and $i = 1,2,\ldots,S$.

In Table 3.1, numbers of calibration measurements for MRM are given for a variety of array types. As seen from Table 3.1, MRM leads to significant savings in the calibration process. The most advantageous array type for this purpose seems to be the uniform circular array which has N symmetry planes. It is followed by the uniform linear and the uniform X-shaped arrays.

Note that, MRM is not related with the used calibration method. MRM is a methodology that is proposed for generating coupled voltage vectors for multiple directions from a measured coupled voltage vector for a symmetric direction. Therefore, the coupled voltage vectors generated through MRM can also be used with the Hui's method or any other calibration method. However, no other method is previously proposed to decrease the calibration measurements. Hence, in Table 3.1, the comparison is done over the number of calibration measurements proposed in the original Hui's method without employing MRM.

Table 3.1: Number of calibration measurements required for different types of arrays which are composed of N identical and omnidirectional antennas. ($\lceil \cdot \rceil$ denotes the ceiling function.)

Array Type	# of Sym. Planes	# of Measurements (Hui's Method)	# of Measurements (MRM)
Uniform Circular	N	$(N-1) \times (N+1)$	1
Uniform Linear	2	$(N-1) \times (N+1)$	$\lceil N/4 \rceil$
Uniform X-Shaped	2	$(N-1) \times (N+1)$	$\lceil N/4 \rceil$
Uniform V-Shaped	1	$(N-1) \times (N+1)$	$\lceil N/2 \rceil$

3.4 Simulations

In this part of the study, the full-wave electromagnetic simulation tool FEKO [12] is used to have measurements. FEKO simulations are implemented by using the method-of-moments (MOM). The performance evaluation is done over DOA estimation accuracy using MUSIC algorithm. The experiments are done using a planar 8-element UCA with identical dipole antennas. The dimensions are selected such that the dipole antenna array has an operating frequency band of 80-800 MHz. The dipole diameter is chosen as 5.25 mm and the dipole length is 34.1 cm which is the half wavelentgh at 440 MHz (the mid frequency). The radiation patterns of a single dipole for 100 MHz (lower band), 440 MHz (mid band) and 800 MHz (upper band) are given in Figures 3.3, 3.4 and 3.5, respectively. In order to avoid spatial aliasing, the distance between two elements in the array is chosen as the half wavelength at 800 MHz, that is 18.75 cm. Each array element is terminated with a $Z_L = 50\Omega$ load. In Figure 3.6, the 8-element UCA model is presented.

As explained at the end of Section 3.2, $N \times (N+1)$ measurements are needed for an N-element array to find the transformation matrix, $\mathbf{T}$, by using the conventional approach. However, as shown in Section 3.3, a single measurement is sufficient for a UCA when MRM is used. In this case, the coupled voltage vector $\mathbf{v}(\phi_1, \theta_1)$ is measured, and $\mathbf{v}(\phi_2, \theta_2), \mathbf{v}(\phi_3, \theta_3), \ldots, \mathbf{v}(\phi_{2S}, \theta_{2S})$ are generated from $\mathbf{v}(\phi_1, \theta_1)$ through cyclic data shifts as explained along with (3.19).

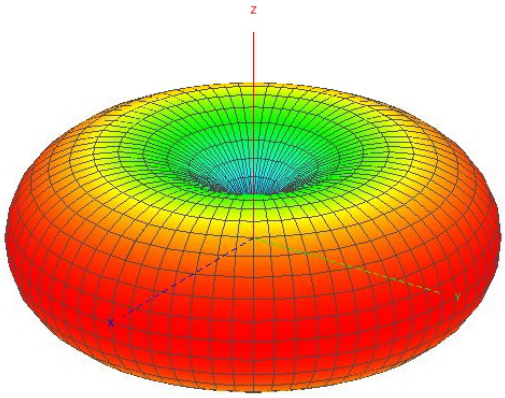

Figure 3.3: The radiation pattern of a single dipole antenna with 5.25 mm diameter and 34.1 cm length at 100 MHz.

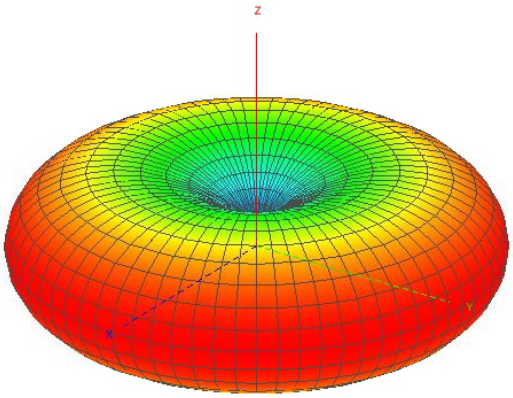

Figure 3.4: The radiation pattern of a single dipole antenna with 5.25 mm diameter and 34.1 cm length at 440 MHz.

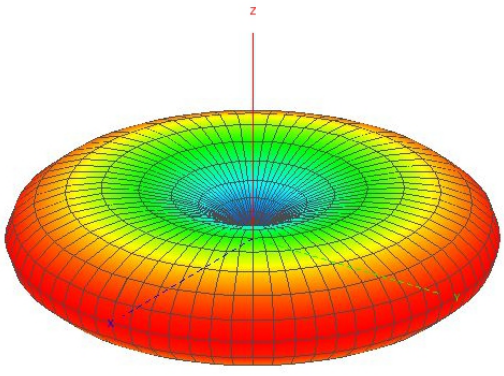

Figure 3.5: The radiation pattern of a single dipole antenna with 5.25 mm diameter and 34.1 cm length at 800 MHz.

Before evaluating the DOA estimation performance of MRM, it is reasonable to evaluate its numerical accuracy. For this purpose, using the 8-element UCA given in Figure 3.6, the coupled voltage vector $\mathbf{v}(10°, 90°)$ is measured at 440 MHz, and seven coupled voltage vectors $\mathbf{v}(55°, 90°), \mathbf{v}(100°, 90°), \ldots, \mathbf{v}(325°, 90°)$ are generated from $\mathbf{v}(10°, 90°)$ by using MRM. Then, $\mathbf{T}$ is found by using (3.13) and denoted as $\mathbf{T_1}$. The mutual coupling matrix $\mathbf{C_1}$ is obtained as the inverse of $\mathbf{T_1}$. It is observed that $\mathbf{C_1}$ is a complex symmetric circulant matrix as it is well known in the literature [16]. $\mathbf{C_1}$ can be represented by its first row, $\mathbf{c_1}$, which is found to be,

$$\mathbf{c_1} = 10^{-3} \times \begin{bmatrix} 0.9151 - 0.7849i \\ 0.1720 + 0.5691i \\ 0.1581 + 0.1152i \\ 0.1048 + 0.1041i \\ 0.1154 + 0.0995i \\ 0.1048 + 0.1041i \\ 0.1580 + 0.1152i \\ 0.1721 + 0.5691i \end{bmatrix}^T \tag{3.21}$$

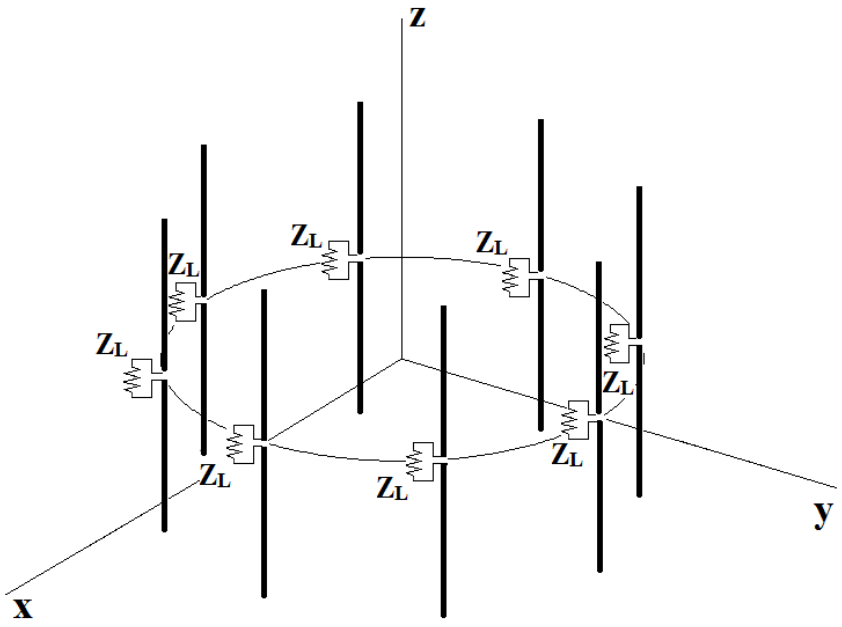

Figure 3.6: The 8-element UCA model used in the performance evaluation experiments.

Now, consider another transformation matrix $\mathbf{T_2}$ that is obtained with the conventional measurement approach. 36 coupled voltage vectors are measured due to single excitation sources separated by 10 degrees in azimuth ($\phi = 10°, 20°, \ldots, 360°, \theta = 90°$). Then, $\mathbf{T_2}$ is found by using (3.13). The difference between $\mathbf{T_1}$ and $\mathbf{T_2}$ can be used to identify the numerical accuracy of MRM. Accordingly, $\frac{\|\mathbf{T_1} - \mathbf{T_2}\|}{\|\mathbf{T_1}\|}$ is calculated and found to be on the order of 10^{-4} which means that the transformation matrix obtained with MRM is very close to the one obtained with the conventional measurement approach. This shows the robustness and numerical accuracy of MRM.

Remark 2: The common approach in calibration measurements is to turn 360 degrees around the antenna array in equiangular steps. If only a limited angular sector is used, $\mathbf{V}$ matrix in (3.11) becomes ill-conditioned. This causes large errors in mutual coupling matrix estimation. As shown in Figure 3.2, MRM generates the measurement vectors by turning 360 degrees around the array in uniform intervals. Hence, $\mathbf{V}$ matrix in (3.11) is a well-conditioned matrix for the UCA. A similar case is valid for other types of arrays as well.

In the first part of the simulations, the performance of MRM against the changes in source azimuth angle is evaluated. For this purpose, the array is excited by three sources on the azimuth plane ($\theta_1 = \theta_2 = \theta_3 = 90°$). Two sources have fixed azimuth angles of $\phi_1 = 50°$ and $\phi_2 = 90°$, and the third source is swept with one degree intervals, i.e., $\phi_3 = 0°, 1°, \ldots, 359°$. The experiment is repeated for lower, mid and upper band frequencies, 100 MHz, 440 MHz and 800 MHz, respectively. $\mathbf{C}$ matrices are separately found and used for each frequency. In Figures 3.7, 3.8, 3.9, MUSIC spectra with and without mutual coupling calibration for $\phi_3 = 200°$ are given. As seen in these three figures, the calibrated array spectra are significantly better than the uncalibrated array spectra. In each of the figures, there are three sharp peaks at the correct azimuth angles in the calibrated array spectrum whereas the peaks in the uncalibrated array spectrum are very smooth, especially for 440 MHz.

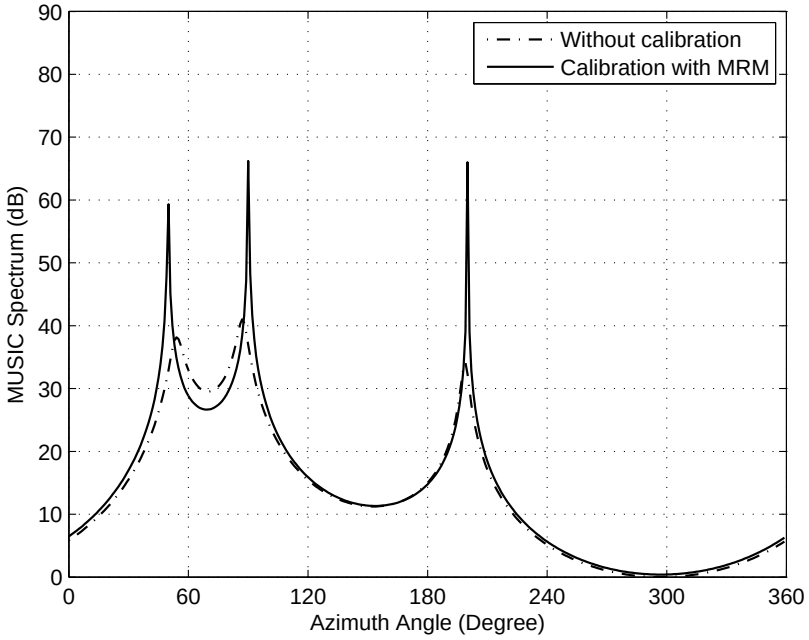

Figure 3.7: The MUSIC spectrum due to three sources at 100 MHz coming from $(\phi_1 = 50^\circ, \theta_1 = 90^\circ)$, $(\phi_2 = 90^\circ, \theta_2 = 90^\circ)$ and $(\phi_3 = 200^\circ, \theta_3 = 90^\circ)$ directions, respectively.

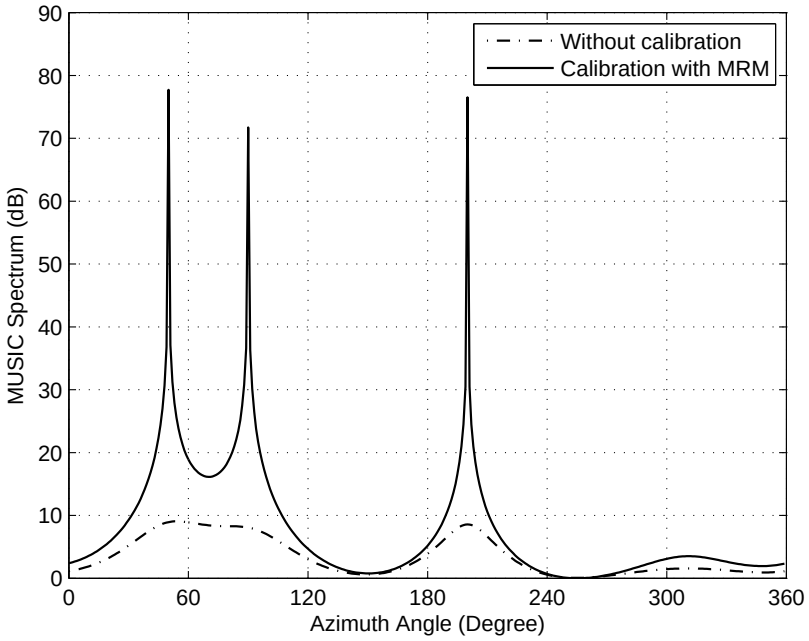

Figure 3.8: The MUSIC spectrum due to three sources at 440 MHz coming from $(\phi_1 = 50^\circ, \theta_1 = 90^\circ)$, $(\phi_2 = 90^\circ, \theta_2 = 90^\circ)$ and $(\phi_3 = 200^\circ, \theta_3 = 90^\circ)$ directions, respectively.

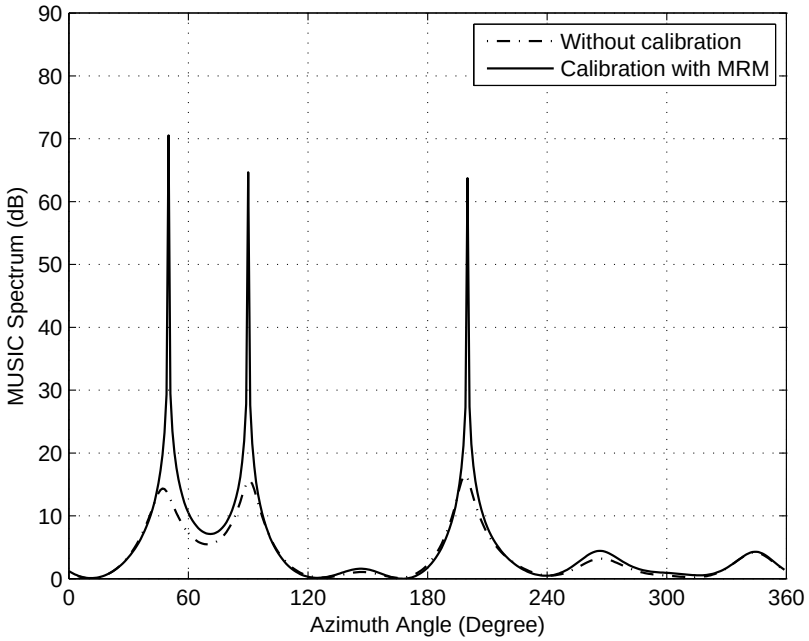

Figure 3.9: The MUSIC spectrum due to three sources at 800 MHz coming from ($\phi_1 = 50°, \theta_1 = 90°$), ($\phi_2 = 90°, \theta_2 = 90°$) and ($\phi_3 = 200°, \theta_3 = 90°$) directions, respectively.

The performance evaluation is done using the root-mean-square errors (RMSE) in DOA estimation. RMSE for the three sources is found as,

$$RMSE = \sqrt{\frac{1}{3}(r_1^2 + r_2^2 + r_3^2)} \tag{3.22}$$

where r_1, r_2 and r_3 are the DOA estimation errors in estimating ϕ_1, ϕ_2 and ϕ_3, respectively. RMSE values for $\phi_3 = 0°, 1°, \ldots, 359°$ at 100 MHz, 440 MHz and 800 MHz are given in Figures 3.10, 3.11 and 3.12, respectively. It is observed that in the literature, it is somehow hard to find figures which show the complete azimuth performance like these three figures. In this context, these figures are important to show that MRM produces a proper mutual coupling matrix, $\mathbf{C}$, that is independent of the azimuth angle as expected for an array with omnidirectional and identical antennas [16]. As seen in Figures 3.10, 3.11 and 3.12, RMSE performance of MRM calibration is significantly better than the performance of the uncalibrated array. The two peaks on the calibrated array responses correspond to the directions of the fixed sources at

$\phi_1 = 50°$ and $\phi_2 = 90°$, respectively. As an additional information, performance of the Hui's method is also given in Figures 3.10, 3.11 and 3.12. When MRM is compared to the Hui's method, it is seen that the performances of the two methods are very close to each other at 440 MHz. However, the Hui's method performs better at 100 MHz and MRM performs better at 800 MHz.

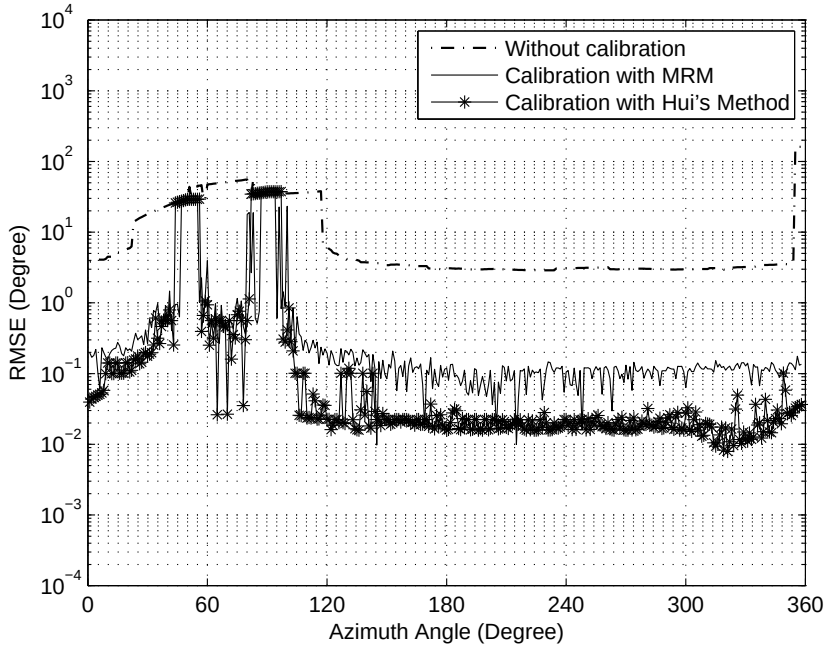

Figure 3.10: The azimuth performances of MRM and the Hui's method at 100 MHz when two sources are fixed at $\phi_1 = 50°$ and $\phi_2 = 90°$, and the third source is swept in one degree resolution.

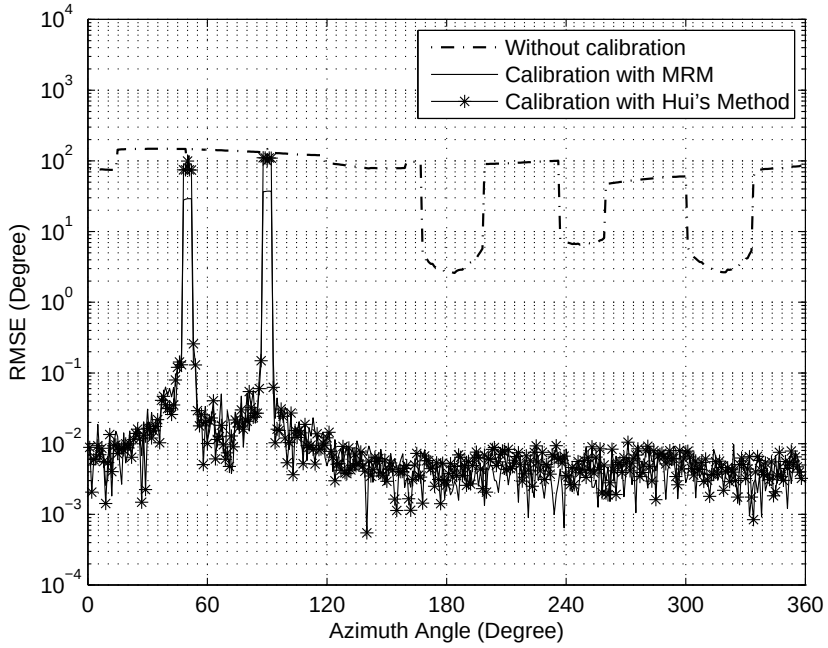

Figure 3.11: The azimuth performances of MRM and the Hui's method at 440 MHz when two sources are fixed at $\phi_1 = 50°$ and $\phi_2 = 90°$, and the third source is swept in one degree resolution.

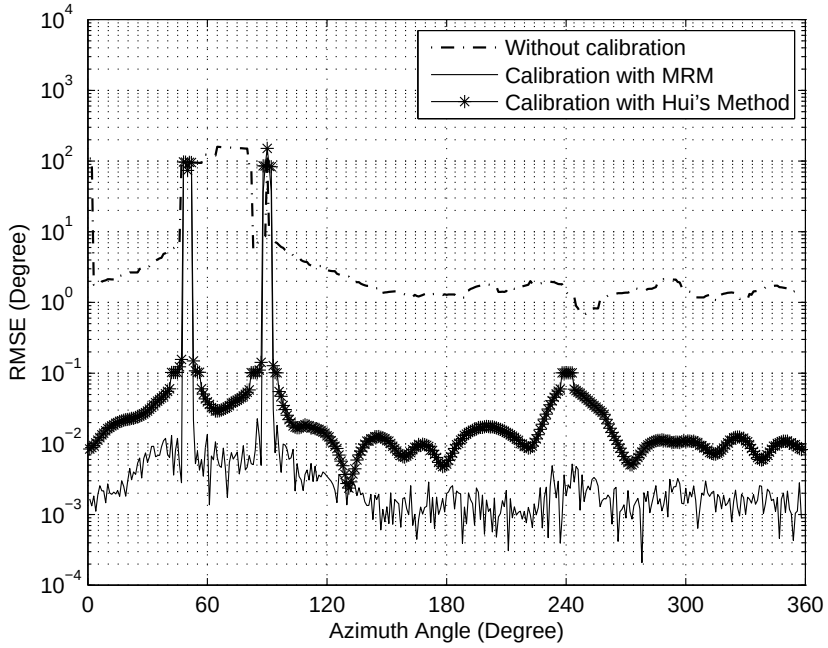

Figure 3.12: The azimuth performances of MRM and the Hui's method at 800 MHz when two sources are fixed at $\phi_1 = 50°$ and $\phi_2 = 90°$, and the third source is swept in one degree resolution.

Additionally, performances of MRM and Hui's method are also compared under noise. The array is excited with three sources on the azimuth plane ($\theta_1 = \theta_2 = \theta_3 = 90°$). Two sources have fixed azimuth angles of $\phi_1 = 50°$ and $\phi_2 = 90°$, and the third source is swept with one degree intervals, i.e., $\phi_3 = 0°, 1°, \ldots, 359°$. The experiment is done at 440 MHz for 20 dB signal-to-noise ratio (SNR) where independent and additive white Gaussian noise components are considered. The RMSE performances of the two methods in this case are given in Figure 3.13. As seen in Figure 3.13, the performances of the two methods are very similar to each other just as in the noise-free case.

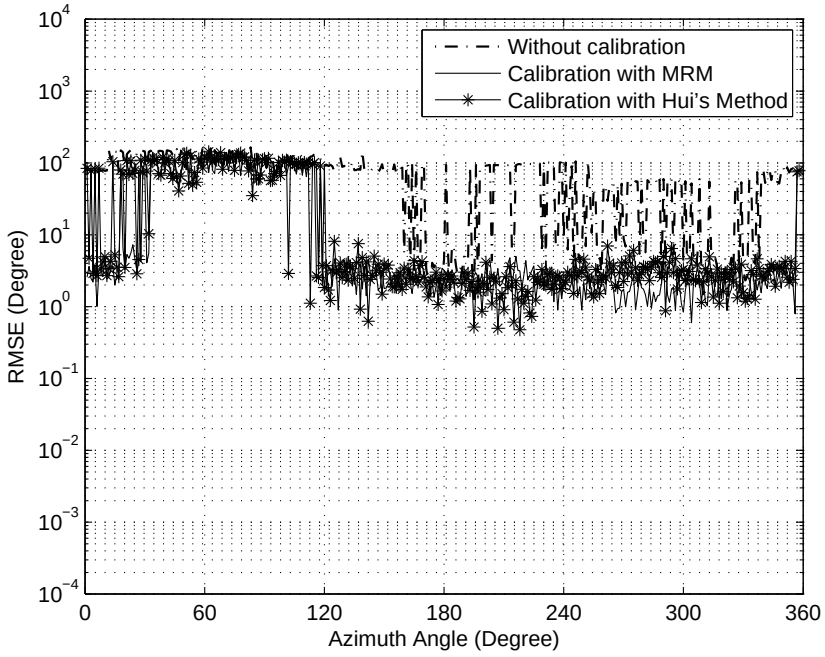

Figure 3.13: The performance comparison of MRM and the Hui's method for the noisy case. The experiment is done at 440 MHz for 20 dB SNR. There are two fixed sources from $\phi_1 = 50°$ and $\phi_2 = 90°$, and the third source is swept in one degree resolution.

In order to evaluate the performance of MRM for the changes in the elevation angles of the excitation sources, the array is excited by three sources whose azimuth angles are $\phi_1 = 50°$, $\phi_2 = 90°$ and $\phi_3 = 200°$, respectively. The $\mathbf{T}$ matrix found for $\theta = 90°$ is used while the source elevation angles $\theta_1 = \theta_2 = \theta_3$ are varied from 75° to 105° with 3 degrees steps. RMSE performance of MRM versus the source elevation angle at 100 MHz, 440 MHz and 800 MHz are presented in Figure 3.14, 3.15 and 3.16, respectively. As seen in these three figures, MRM is very robust against changes in the source

elevation angle. Also, the calibrated array performance is significantly better than the uncalibrated array performance.

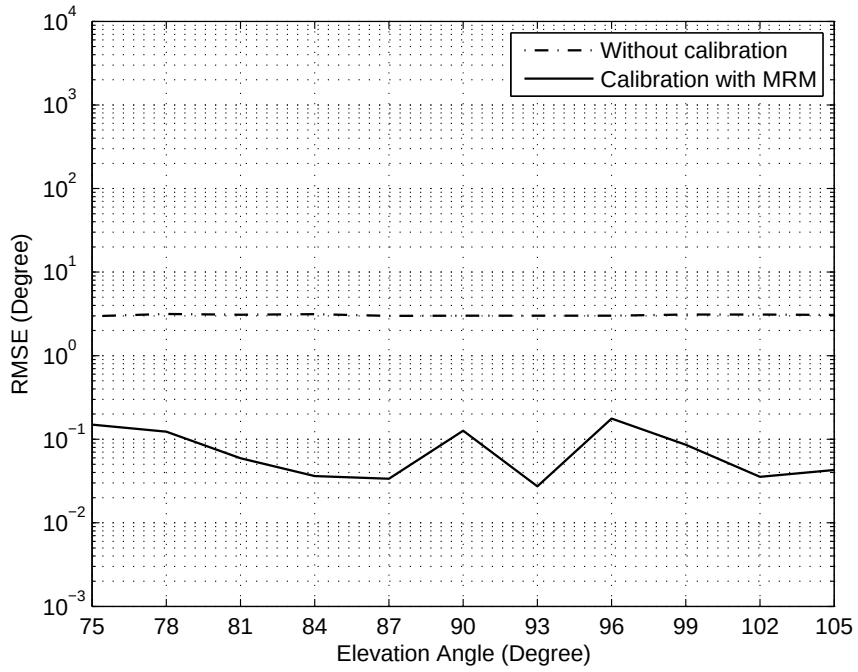

Figure 3.14: The elevation performance of MRM at 100 MHz for three sources whose elevation angles $\theta_1 = \theta_2 = \theta_3$ are varied from 75° to 105° with 3 degree steps.

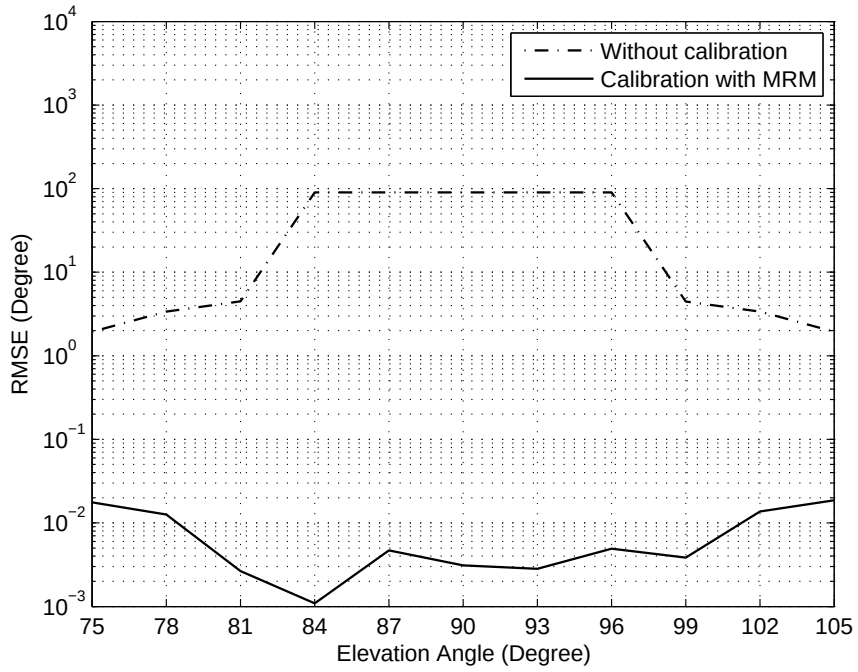

Figure 3.15: The elevation performance of MRM at 440 MHz for three sources whose elevation angles $\theta_1 = \theta_2 = \theta_3$ are varied from 75° to 105° with 3 degree steps.

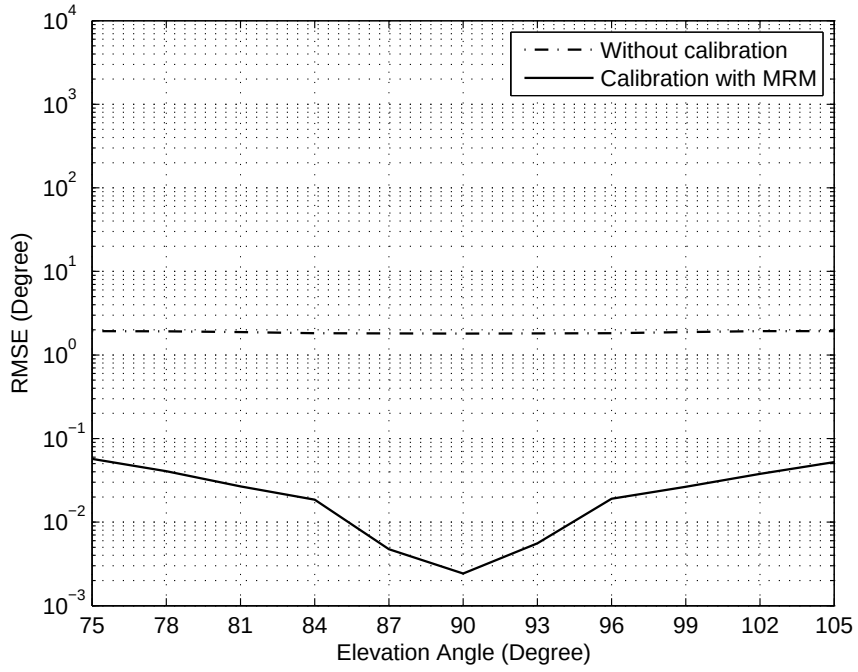

Figure 3.16: The elevation performance of MRM at 800 MHz for three sources whose elevation angles $\theta_1 = \theta_2 = \theta_3$ are varied from 75° to 105° with 3 degree steps.

Performance of MRM for the changes in the source frequency is also examined. The array is excited by three sources whose elevation angles are $\theta_1 = \theta_2 = \theta_3 = 90°$. The source azimuth angles are selected to be $\phi_1 = 50°$, $\phi_2 = 90°$ and $\phi_3 = 200°$, respectively. In Figures 3.17, 3.18 and 3.19, RMSE performances of MRM versus the source frequency are presented for lower, mid and upper band, respectively. In Figure 3.17, the $\mathbf{T}$ matrix found for 100 MHz is used while the source frequencies $f_1 = f_2 = f_3$ are varied from 95 MHz to 105 MHz with 125 kHz steps. In Figure 3.18, the $\mathbf{T}$ matrix found for 440 MHz is used while the source frequencies $f_1 = f_2 = f_3$ are varied from 435 MHz to 445 MHz with 125 kHz steps. In Figure 3.19, the $\mathbf{T}$ matrix found for 800 MHz is used while the source frequencies $f_1 = f_2 = f_3$ are varied from 795 MHz to 805 MHz with 125 kHz steps. As seen in these figures, the calibrated array performance is significantly better than the uncalibrated array performance. Also, the best performances for the calibrated array are observed at 100 MHz, 440 MHz and 800 MHz as expected. As the source frequency is changed, the mutual coupling between the antenna elements changes, and the $\mathbf{T}$ matrices found for 100 MHz, 440 MHz and 800 MHz may not be satisfactory.

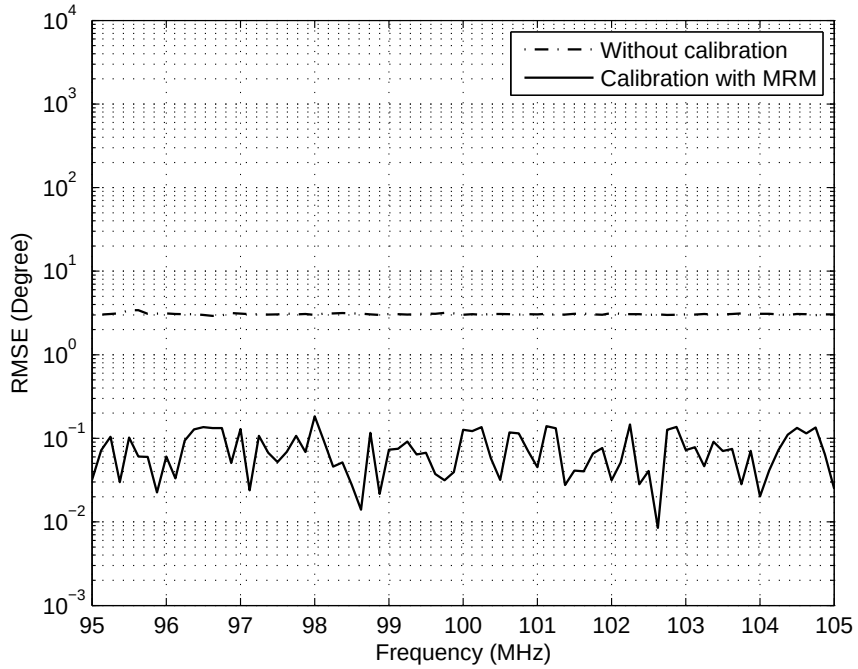

Figure 3.17: The frequency performance of MRM for three sources whose frequencies $f_1 = f_2 = f_3$ are varried between 95 MHz and 105 MHz.

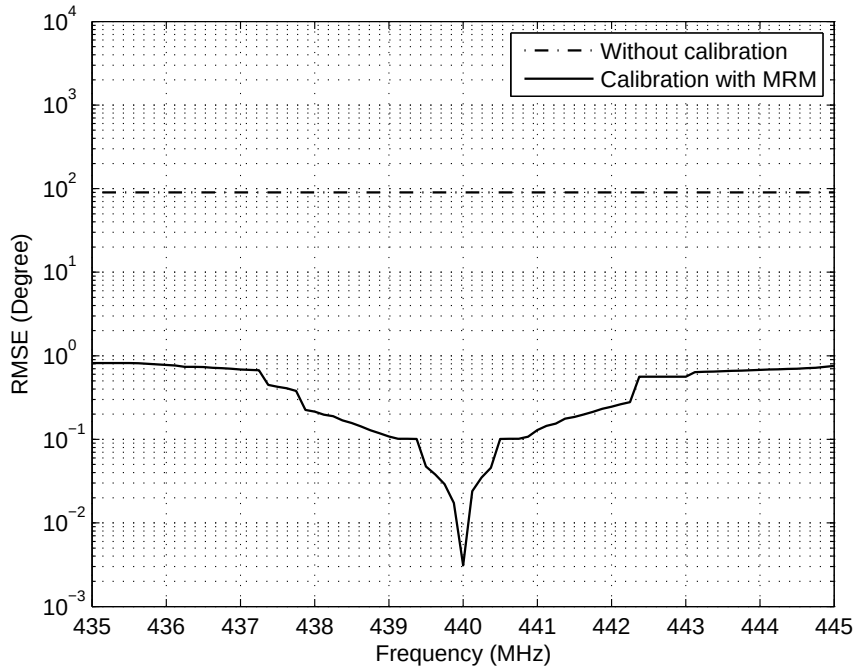

Figure 3.18: The frequency performance of MRM for three sources whose frequencies $f_1 = f_2 = f_3$ are varried between 435 MHz and 445 MHz.

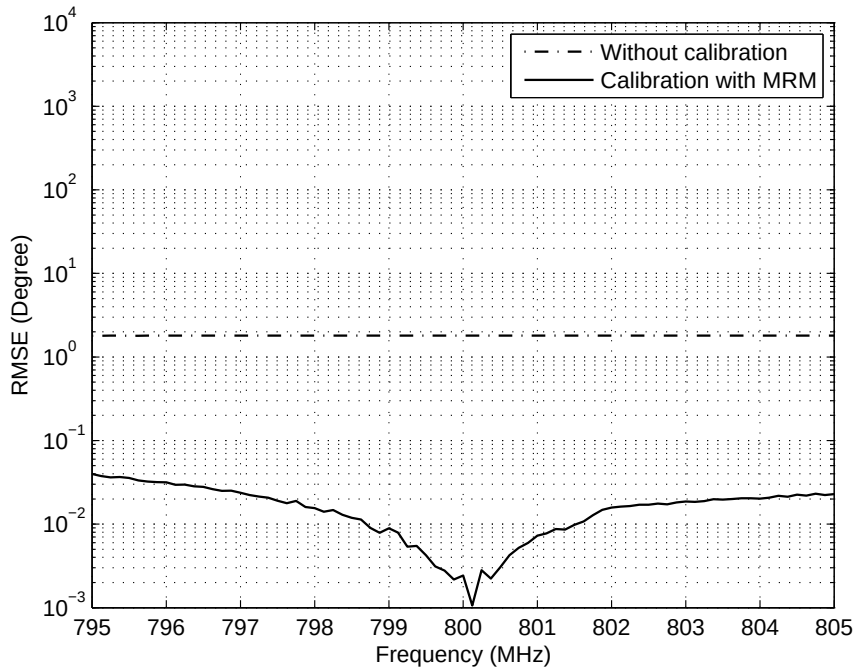

Figure 3.19: The frequency performance of MRM for three sources whose frequencies $f_1 = f_2 = f_3$ are varried between 795 MHz and 805 MHz.

CHAPTER 4

MUTUAL COUPLING CALIBRATION OF NON-OMNIDIRECTIONAL ANTENNA ARRAYS

In the previous chapter, mutual coupling calibration of omnidirectional antennas is considered. The transformation approach is presented to determine the mutual coupling matrix, $\mathbf{C}$, using a linear relationship between the measured and the ideal array data. Furthermore, MRM is presented in order to reduce the number of measurements required for calibration.

In this chapter, mutual coupling calibration of arrays composed of non-omnidirectional (NOD) antennas is considered. It is shown that a single $\mathbf{C}$ matrix can not completely model the mutual coupling effect for an NOD antenna array. In this context, *a sectorized approach* is proposed for accurate mutual coupling calibration of NOD antenna arrays. In this approach, calibration is done in angular sectors and a different coupling matrix is found for each sector using the transformation approach. In addition, it is shown that MRM is also applicable to NOD antenna arrays with identical elements if the array has symmetry planes in its geometry.

Before presenting the sectorized approach, it is convenient to give the signal model used in the course of this chapter.

4.1 Signal Model

In this chapter, antenna arrays composed of identical and non-omnidirectional elements are considered in a noise-free environment, and narrowband model is used.

The output vector due to an excitation source from (ϕ_l, θ_l) direction for an N-element antenna array is given as,

$$\mathbf{y}(t) = \mathbf{C}(\phi_l, \theta_l)\, \mathbf{\Gamma}(\phi_l, \theta_l)\, \mathbf{a}(\phi_l, \theta_l)\, s(t), \quad t = 1, 2, \ldots, P \tag{4.1}$$

For notational convenience, $\mathbf{C}(\phi_l, \theta_l)$ is abbreviated as $\mathbf{C}_l$ and $\mathbf{\Gamma}(\phi_l, \theta_l)$ is abbreviated as $\mathbf{\Gamma}_l$. Then, (4.1) is written as,

$$\mathbf{y}(t) = \mathbf{C}_l\, \mathbf{\Gamma}_l\, \mathbf{a}(\phi_l, \theta_l)\, s(t), \quad t = 1, 2, \ldots, P \tag{4.2}$$

where P is the number of snapshots and $\mathbf{C}_l$ is the $N \times N$ mutual coupling matrix for (ϕ_l, θ_l) direction. $\mathbf{\Gamma}_l = diag\{\gamma_{l1}, \gamma_{l2}, \ldots, \gamma_{lN}\}$ are the gain/phase mismatches in antenna elements due to non-omnidirectional antenna patterns for (ϕ_l, θ_l) direction where any gain/phase mismatches due to cabling and instrumentation are neglected. $\mathbf{a}(\phi_l, \theta_l) = [\alpha_1(\phi_l, \theta_l) \quad \alpha_2(\phi_l, \theta_l) \ldots \alpha_N(\phi_l, \theta_l)]^T$ is the steering vector for (ϕ_l, θ_l) direction. The vector element corresponding to the n^{th} antenna positioned at (x_n, y_n, z_n) is $\alpha_n(\phi_l, \theta_l) = e^{j\frac{2\pi}{\lambda}(x_n \cos\phi_l \sin\theta_l + y_n \sin\phi_l \sin\theta_l + z_n \cos\theta_l)}$. $s(t)$ is the complex amplitude of the excitation source from (ϕ_l, θ_l) direction.

Since identical array elements are considered, gain/phase mismatch terms for all of the array elements are the same, i.e. $\gamma_{l1} = \gamma_{l2} = \cdots = \gamma_{lN} = \gamma_l$. Hence, (4.2) reduces to,

$$\mathbf{y}(t) = \gamma_l\, \mathbf{C}_l\, \mathbf{a}(\phi_l, \theta_l)\, s(t), \quad t = 1, 2, \ldots, P \tag{4.3}$$

Note that, for the case of NOD antennas, the mutual coupling matrix, $\mathbf{C}_l$, changes with the azimuth angle unlike the case of omnidirectional antennas given in the previous chapter. In this case, the MUSIC algorithm estimates the DOA angles as the maxima of the following spectrum,

$$P_{MU}(\phi, \theta) = \frac{1}{\mathbf{a}^H(\phi, \theta)\, \mathbf{C}_l^H\, \gamma_l^*\, \mathbf{E}_N\, \mathbf{E}_N^H\, \gamma_l\, \mathbf{C}_l\, \mathbf{a}(\phi, \theta)} \tag{4.4}$$

where $(\cdot)^*$ denotes the complex conjugate.

Note that, if the correct $\mathbf{C}_l$ matrix is not supplied, the MUSIC algorithm can result errors in DOA estimation which may be larger than 10 degrees. Therefore, it is an important task to determine the $\mathbf{C}_l$ matrix to be used. Antenna pattern is a smooth function of azimuth and elevation angles for most of the antenna types. In addition, the mutual coupling effect in an antenna array does not change rapidly as the azimuth and elevation angles change. In other words, $\mathbf{C}_l$ can be assumed to remain unchanged for a sufficiently small angular sector. As a result, a sectorized approach seems to be a natural choice for mutual coupling calibration of NOD antenna arrays. In this context, a sectorized approach is presented in the next section for proper calibration of NOD antenna arrays.

4.2 Sectorized Approach

Mutual coupling characteristics do not change with the azimuth angle for omnidirectional antennas [16]. This is a consequence of the perfect angular symmetry present in their radiation pattern. In the case of NOD antennas, mutual coupling characteristics change with the azimuth angle since the angular symmetry in their radiation pattern is not perfect or even does not exist. In this context, a new sectorized calibration approach for arrays with identical NOD antennas is presented below.

In the sectorized approach, the idea is to divide 360 degrees into certain angular sectors in azimuth and obtain a distinct $\mathbf{C}$ matrix for each sector. While different types of angular sectors can be used, uniform and non-overlapping angular sectors are considered in this study. Therefore, the main issue is to properly determine the sector width, so that the mutual coupling characteristics approximately remain fixed within each sector.

Choosing the sectors as small as possible may seem to provide a more accurate mutual coupling characterization for each sector. However, in order to find a $\mathbf{C}$ matrix for a sector, array data for $L \geq N$ directions from that sector are required. Therefore, choosing unnecessarily small sectors will increase the total number of measurements and the manual labour. In addition, choosing smaller sectors makes the measurement directions get closer, and the $\mathbf{V}$ matrix in (3.11) may become ill-conditioned [11]. If $\mathbf{V}$ becomes ill-conditioned, the resulting $\mathbf{T}$ matrix (hence, the $\mathbf{C}$ matrix) will not cor-

rectly characterize the mutual coupling effect for the corresponding sector. Therefore, the sector width should be selected such that it is small enough to obtain a uniform antenna pattern and it is large enough not to end up with redundant measurements and ill-conditioned **V** matrices.

As it can be seen in (3.11), **T** (hence, **C**) changes with **U** and **V**. If the array elements are identical, **U** and **V** depend on,

- Array geometry
- Radiation pattern of a single antenna
- Number of antennas in the array

Obtaining a closed form expression for the sector width using the items in the above list is a hard if not an impossible problem. Therefore, the following iterative procedure is proposed for this purpose:

1. Determine a performance criterion and start with two non-overlapping sectors of 180° angular width.
2. Find a **C** matrix for each sector.
3. Make a performance test to see whether the **C** matrices satisfy the performance criterion or not.
4. If the performance criterion is satisfied, select the current sector width. If it is not satisfied, select a new sector width less than the current sector width and return to Step 2.

As stated above, in order to calculate a **C** matrix for a sector, measurements for $L \geq N$ directions from that sector are required. The studies show that it is sufficient to choose $L = N$ for a proper calibration. Choosing $L > N$ does not bring any further performance improvement. Instead, it increases the possibility of ending up with an ill-conditioned **V** matrix when L is chosen large.

Sectorized calibration approach gives an opportunity for calibrating NOD antennas, however, it requires extra measurements for the sectors. In the next section, extension

of MRM for NOD antenna arrays is presented in order to decrease the number of required measurements significantly.

4.3 MRM for NOD Antenna Arrays

In Section 3.3, MRM is proposed for arrays composed of identical and omnidirectional antennas. It is shown that measurements from symmetric directions can be generated from each other through simple permutations in data vectors. In this section, MRM is shown to be valid for the case of arrays with identical NOD antennas as well.

Consider an N-element array composed of identical NOD antennas with the signal model given in (4.3). Then, the uncoupled voltage vector due to an excitation source from (ϕ_l, θ_l) is the same as the corresponding steering vector up to a complex scaling factor γ_l, i.e.,

$$\mathbf{u}(\phi_l, \theta_l) = \gamma_l \, \mathbf{a}(\phi_l, \theta_l) \tag{4.5}$$

where γ_l is the gain/phase mismatch due to the non-omnidirectionality of the antennas. Note that, the scaling factor, β, in (3.12) for the case of omnidirectional antennas is independent from source direction. Whereas, the scaling factor, γ_l, in (4.5) for the case of NOD antennas changes with source direction (ϕ_l, θ_l). However, when a proper angular partitioning is applied, γ_l can be assumed to be constant within each sector. Therefore, in order to find a $\mathbf{T}$ matrix for a sector, the steering matrix $\mathbf{A}$ can be used instead of the uncoupled voltage matrix $\mathbf{U}$. Hence, (3.13) is valid within each sector. Eventually, no measurements are required for $\mathbf{U}$ and it is sufficient to have measurements only for $\mathbf{V}$. Below, the approach to further decrease the measurements for $\mathbf{V}$ is presented. In this presentation, the counterpart of the result given in *Fact 1* will be obtained for NOD antennas. Then, the data generation method given in *Lemma 2* and *Lemma 3* is directly used.

Lemma 4: Consider a volumetric array with N identical NOD antennas, $e_1, e_2, \ldots, e_N$, and S symmetry planes, $s_1, s_2, \ldots, s_S$, in its geometry. Let $\mathbf{g_1}(\phi_1, \theta_1)$ be a unit direction vector which is not lying on a symmetry plane, and $\mathbf{g_2}(\phi_2, \theta_2)$ be symmetric

to $\mathbf{g_1}(\phi_1, \theta_1)$ with respect to s_1. Also, assume that e_2 and e_N be symmetric array elements with respect to s_1. Then, $V_N(\phi_1, \theta_1) = V_2(\phi_2, \theta_2)$.

Proof 4: In Figure 4.1, top view of a UCA with patch antennas is given as an example for the two dimensional geometry of the problem. Referring to Figure 4.1, assume that e_2 is excited with a voltage source. The far-field radiation pattern in this configuration is *the transmitting array pattern due to* e_2.

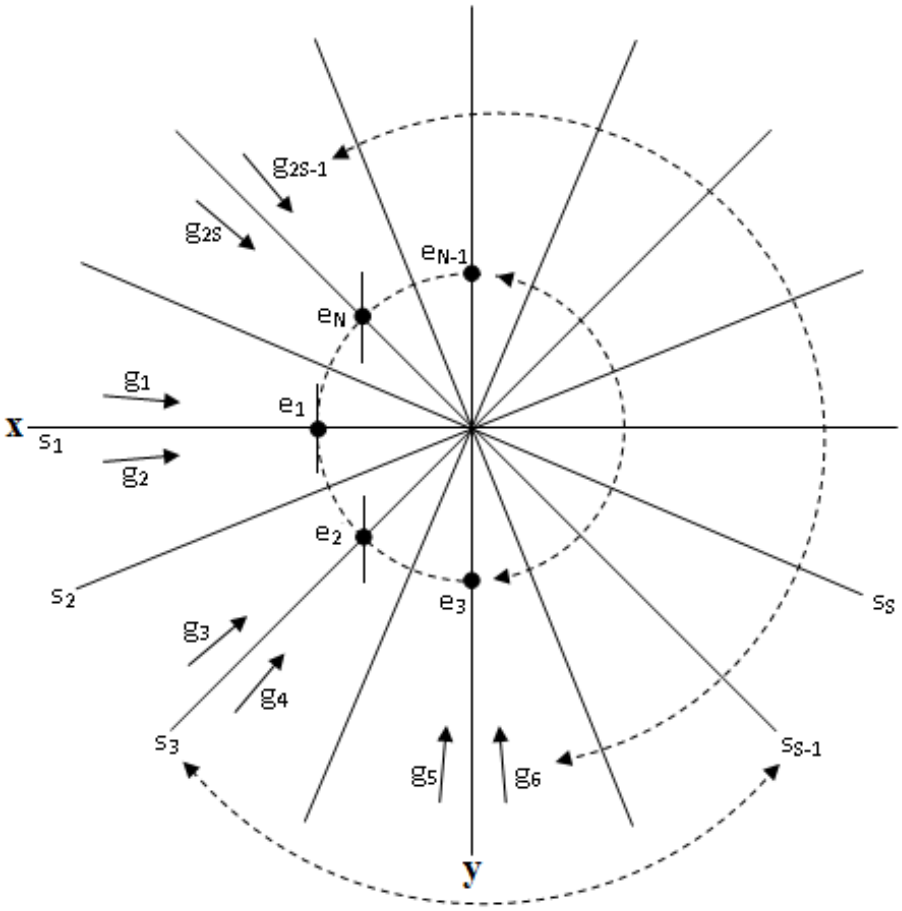

Figure 4.1: The top view of a UCA with N patch antenna elements, $e_1, e_2, \ldots, e_N$. There are S symmetry planes, $s_1, s_2, \ldots, s_S$, in the array.

The transmitting array pattern due to an array element has the following properties:

1. Since the array is composed of identical elements, the transmitting array patterns due to symmetric elements are symmetric. This is verified through FEKO simulations. As seen in Figures 4.2 and 4.3, the transmitting array pattern due to e_2 is symmetric to the transmitting array pattern due to e_N with respect to

s_1.

2. Since receiving and transmitting characteristics of antennas are the same due to reciprocity, the receiving array pattern due to an array element is the same as the transmitting array pattern due to that array element.

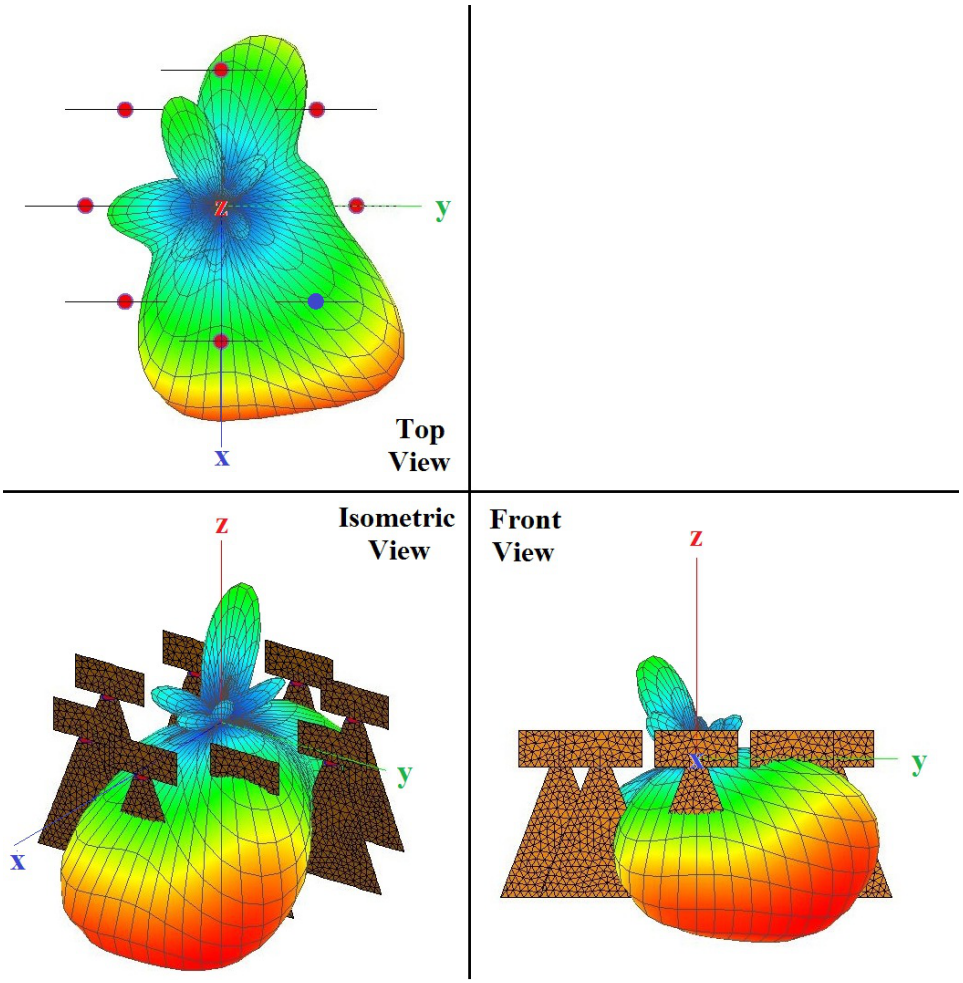

Figure 4.2: The three dimensional transmitting array pattern due to e_2 from top, front and isometric view angles.

If the first two properties are combined, the receiving array patterns due to symmetric elements are symmetric. On the other hand, while the coupled voltage at an array element is being measured, the measured value is determined by the receiving array pattern due to that array element. Therefore, the coupled voltages due to sources from symmetric directions measured at symmetric elements are equal. Namely, the coupled voltage at e_N due to a source from $\mathbf{g_1}(\phi_1, \theta_1)$ is equal to the coupled voltage at e_2 due to a source from $\mathbf{g_2}(\phi_2, \theta_2)$, i.e., $V_N(\phi_1, \theta_1) = V_2(\phi_2, \theta_2)$.

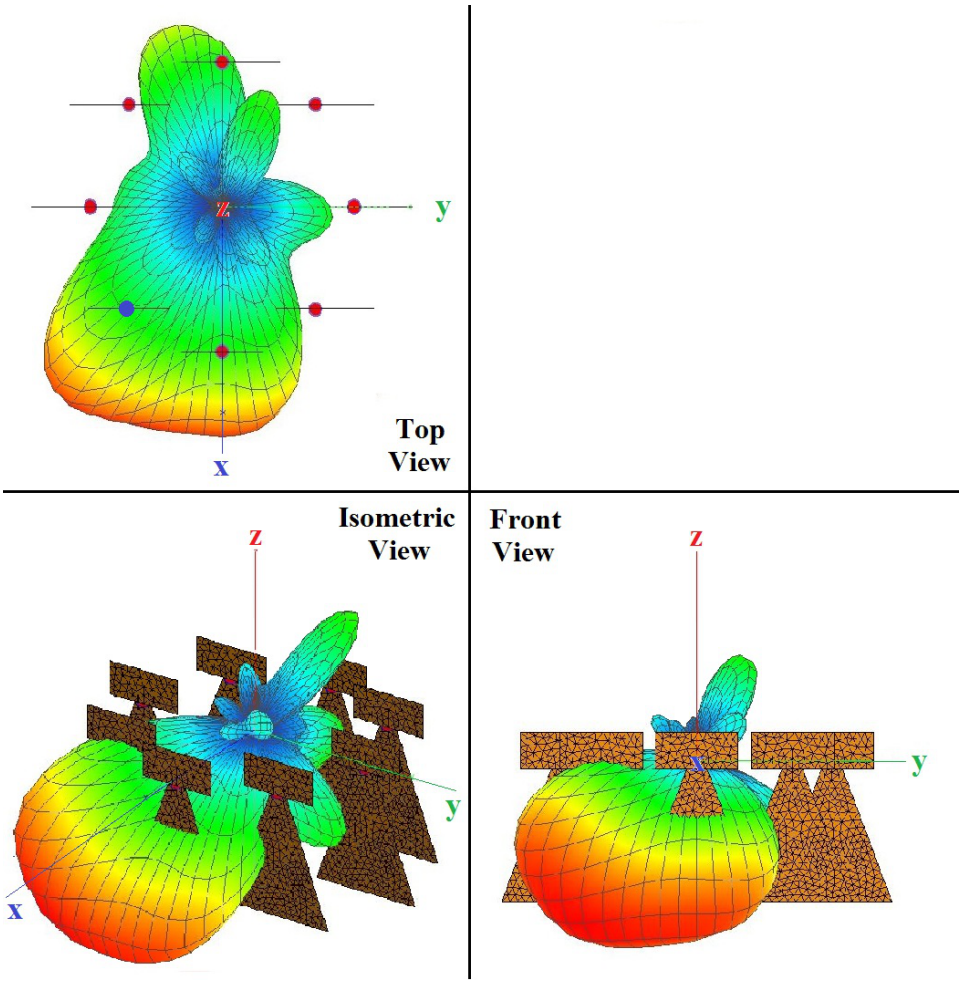

Figure 4.3: The three dimensional transmitting array pattern due to e_N from top, front and isometric view angles.

Now, we can directly use the results of *Lemma 2* and *Lemma 3* to conclude that $2S-1$ coupled voltage vectors, $\mathbf{v}(\phi_2,\theta_2), \mathbf{v}(\phi_3,\theta_3), \ldots, \mathbf{v}(\phi_{2S},\theta_{2S})$, can be generated from $\mathbf{v}(\phi_1,\theta_1)$ through data permutations.

In order to find a $\mathbf{C}$ matrix for a sector, coupled voltage vectors corresponding to at least $L = N$ directions in that sector are required. Now, let D be the number of non-overlapping sectors determined by the sectorized approach. Then, in total, array data from $D \times N$ directions are required in order to find $\mathbf{C}$ matrices for each sector. Since $2S$ array data can be generated from a single measurement by MRM, it is sufficient to make measurements for $L = \lceil \frac{D \times N}{2S} \rceil$ directions. In order to end up with array data from uniformly spaced directions at the end of MRM process, the L measurements should be taken uniformly in $360/(D \times N)$ degrees apart and they

should not be symmetric with respect to any symmetry plane in the array geometry.

The implementation of MRM combined with the sectorized approach for an N-element array with NOD antennas and S symmetry planes can be summarized as follows:

1. Determine the number of non-overlapping sectors, D, using the sectorized approach.
2. Choose $L = \lceil \frac{D \times N}{2S} \rceil$ adjacent directions that are spaced $\frac{360}{D \times N}$ degrees apart such that they are not symmetric with respect to any symmetry plane in the array geometry.
3. Obtain the coupled voltage vectors due to single excitation sources from the chosen L directions, $\mathbf{v}(\phi_l, \theta_l)$ $(l = 1, 2, \ldots, L)$.
4. Use MRM and generate $(2S - 1) \times L$ coupled voltage vectors from $\mathbf{v}(\phi_l, \theta_l)$ $(l = 1, 2, \ldots, L)$ through data permutations. In total, we will end up with $2SL$ coupled voltage vectors which should be used as groups of N in order to find a $\mathbf{T}$ matrix for each sector.
5. Take N of the total $2SL$ coupled voltage vectors from directions lying in the first sector and use (3.13) to find $\mathbf{T}_1$ for this sector. Then, take the inverse of $\mathbf{T}_1$ to find $\mathbf{C}_1$, i.e., $\mathbf{C}_1 = \mathbf{T}_1^{-1}$.
6. Repeat Step-5 for all of the sectors, and obtain $\mathbf{C}_d$, $d = 1, 2, \ldots, D$.

4.4 Simulations

In this part of the study, the full-wave electromagnetic simulation tool FEKO [12] is used to have measurements as in the previous chapter. FEKO simulations are implemented by using the method-of-moments (MOM). The performance of the sectorized approach combined with MRM is evaluated through DOA estimation simulations using the MUSIC algorithm. In the experiments, a planar 8-element UCA composed of patch antenna elements given in Figure 4.4 is used. The patch antenna is a wideband non-symmetric dipole antenna designed by T. Engin Tuncer [17]. This antenna has an operating band from 80 MHz up to 800 MHz. As seen in Figure 4.5, the antenna has

a perfect omnidirectional radiation pattern at 100 MHz. However, as seen in Figures 4.5-4.9, the perfect omnidirectional characteristic is gradually lost when the operating frequency is increased. As seen in Figure 4.9, this antenna can be seen as an NOD antenna at 800 MHz. Since the antenna is omnidirectional in the lower band and non-omnidirectional in the upper band, we call it as *a semi-omnidirectional antenna*.

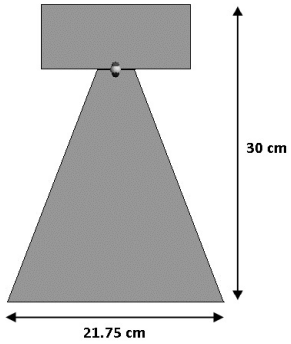

Figure 4.4: The wideband non-symmetric dipole patch antenna [17] used in the experiments.

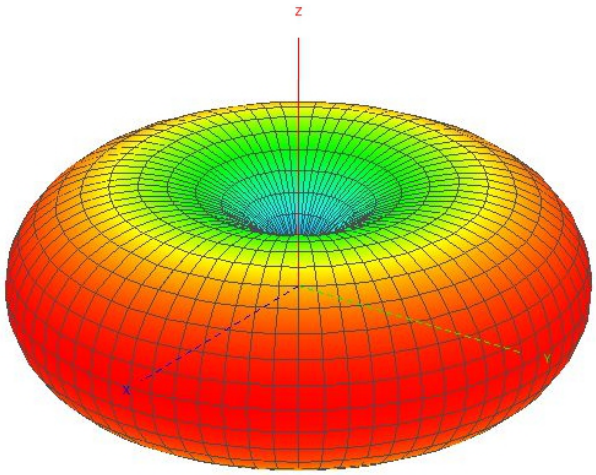

Figure 4.5: Three dimensional radiation pattern of the semi-omnidirectional antenna at 100 MHz.

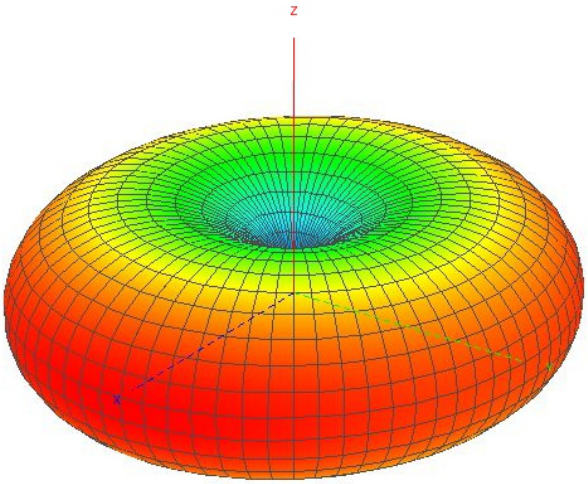

Figure 4.6: Three dimensional radiation pattern of the semi-omnidirectional antenna at 300 MHz.

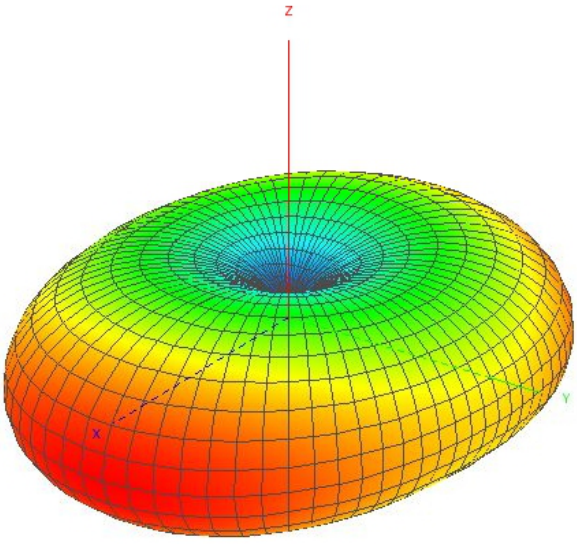

Figure 4.7: Three dimensional radiation pattern of the semi-omnidirectional antenna at 440 MHz.

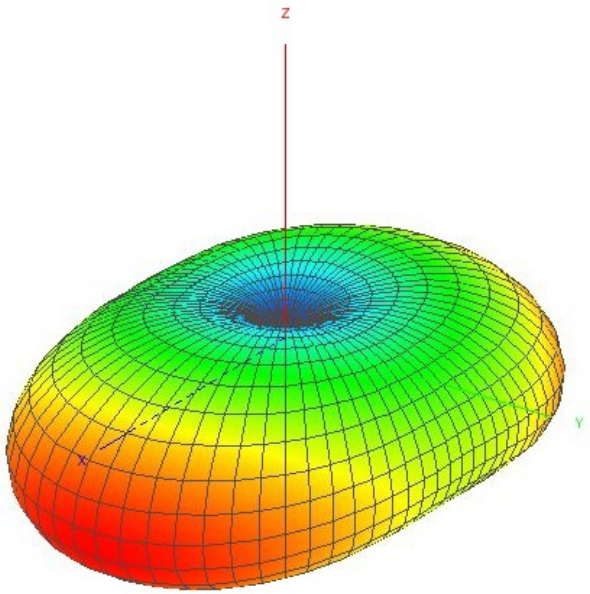

Figure 4.8: Three dimensional radiation pattern of the semi-omnidirectional antenna at 600 MHz.

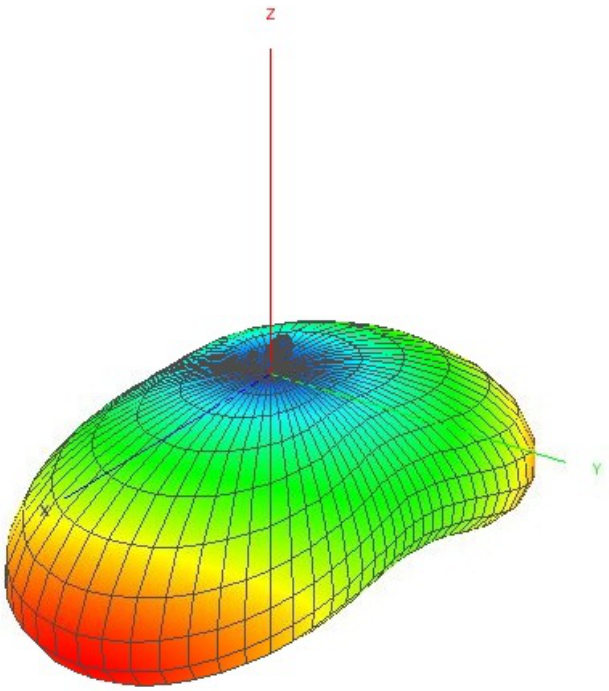

Figure 4.9: Three dimensional radiation pattern of the semi-omnidirectional antenna at 800 MHz.

It is also possible to use a directional antenna with a narrow beam as the NOD antenna in the simulations, however, a semi-omnidirectional antenna is prefered for better illustration of the idea. When narrow-beam directional antennas are used, the mutual coupling effect in the array will be negligible since the antennas have narrow main beams. On the other hand, omnidirectional antennas are prefered in DOA estimation applications in order to have a better angular coverage, which is another motivation for using the semi-omnidirectional antenna.

In Figure 4.10, the 8-element UCA model used in the simulations is presented. In the array, the minimum distance between two array elements is 18.75 cm, and all the antennas are terminated with a $Z_L = 50\Omega$ load. The operating frequency is chosen as 800 MHz in order to use the non-omnidirectional characteristics of the semi-omnidirectional antenna.

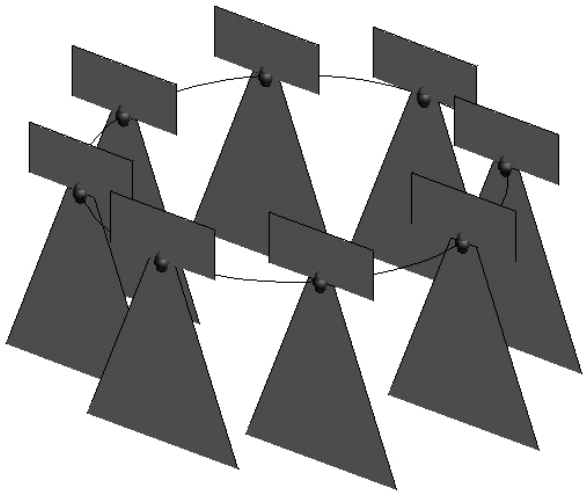

Figure 4.10: The 8-element UCA model composed of semi-omnidirectional antennas.

It is reasonable to start with the conventional calibration approach where a single $\mathbf{C}$ matrix is used. In order to calculate $\mathbf{C}$, eight measurements are obtained due to single excitation sources from uniformly spaced directions on the azimuth plane. Then, the array is excited with a single source whose azimuth angle is swept with one degree resolution, i.e., $\phi = 0^\circ, 1^\circ, \ldots, 359^\circ$, and elevation angle is θ=90°. In Figure 4.11, RMSE performance of the conventional calibration approach in DOA estimation using the MUSIC algorithm is given. As seen in Figure 4.11, a single $\mathbf{C}$ matrix can not

properly model the mutual coupling effect for an NOD antenna array. Therefore, the sectorized approach is needed for proper mutual coupling calibration of NOD antenna arrays.

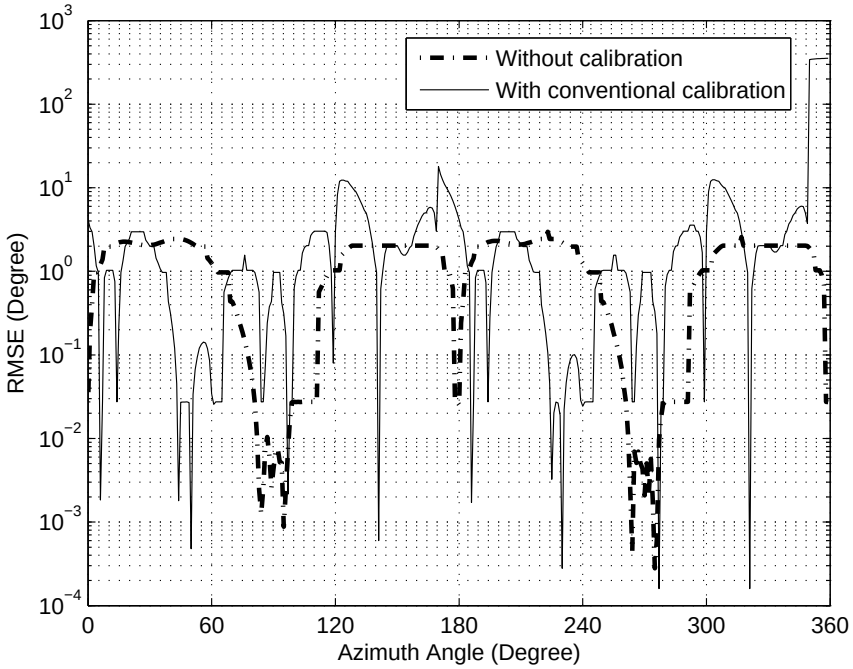

Figure 4.11: The azimuth performance of the conventional calibration approach where a single **C** matrix is used for the whole azimuth plane.

When the sectorized approach is applied to the array given in Figure 4.10 with a performance measure of maximum RMSE of 0.1° in DOA estimation, the sector width is determined as 90° following the 4-step procedure given in Section 4.2. Then, a different **C** matrix is found for each sector following the 6-step procedure given in Section 4.3. In order to evaluate the azimuth performance of the sectorized approach combined with MRM, the array is excited with a single source whose azimuth angle is swept with one degree resolution, i.e., $\phi = 0°, 1°, \ldots, 359°$, and elevation angle is $\theta = 90°$. In Figure 4.12, RMSE performance of the sectorized approach combined with MRM in DOA estimation using the MUSIC algorithm is given. As seen in Figure 4.12, a proper mutual coupling calibration is achieved using the sectorized calibration approach.

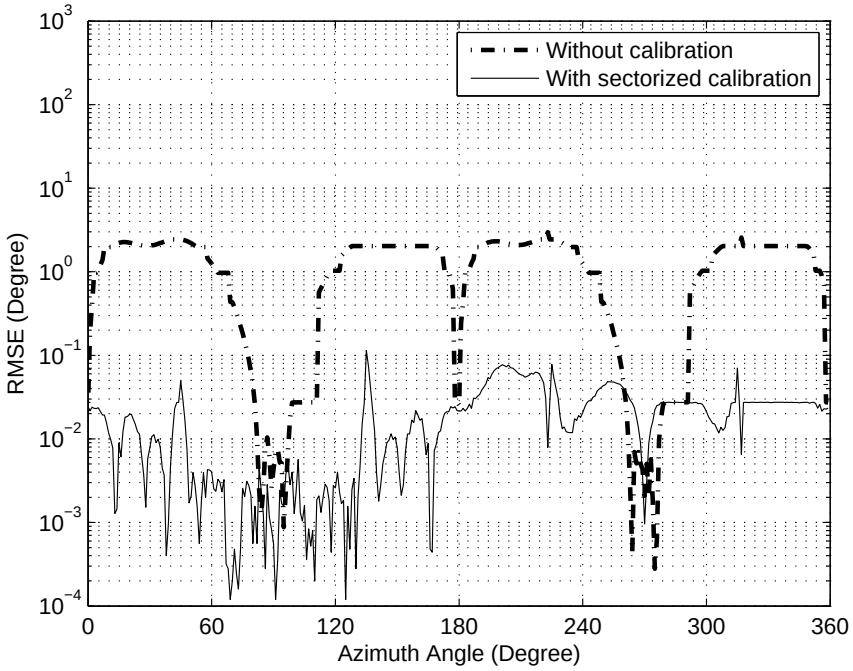

Figure 4.12: The azimuth performance of the sectorized calibration approach combined with MRM where the azimuth plane is divided into 90° wide sectors and a distinct **C** matrix is used for each sector.

In order to evaluate the performance of the sectorized calibration for the changes in source elevation angle, the array is excited by a single source. The **C** matrices found for $\theta = 90°$ are used while the source elevation angle is varied from 75° to 105° with 3 degrees steps. The source azimuth angle is swept as $\phi = 0°, 1°, \ldots, 359°$ and the average of the RMSE values for these azimuth angles is used for each elevation angle, that is:

$$E(\theta) = \frac{1}{360} \sum_{\phi=0°}^{359°} e(\phi, \theta), \qquad \theta = 75°, 78°, \ldots, 105° \tag{4.6}$$

where $e(\phi, \theta)$ is the RMSE value found for (ϕ, θ) direction and $E(\theta)$ is the average error for the corresponding elevation angle. In Figure 4.13, the elevation performance of the sectorized approach combined with MRM is presented. As seen in Figure 4.13, the best performance of the calibrated array is at 90° as expected. The calibrated array performance is better than the uncalibrated array performance in an elevation sector of $81° - 96°$. However, the **C** matrix found for $\theta = 90°$ does not properly work

for the elevation angles outside $87^\circ - 93^\circ$ region. The reason for this result is the physical structure of the patch antenna which is non-symmetric with respect to the xy-plane. It is possible to overcome this situation by following a sectorized approach for the elevation angles along with the sectorized approach for the azimuth angles.

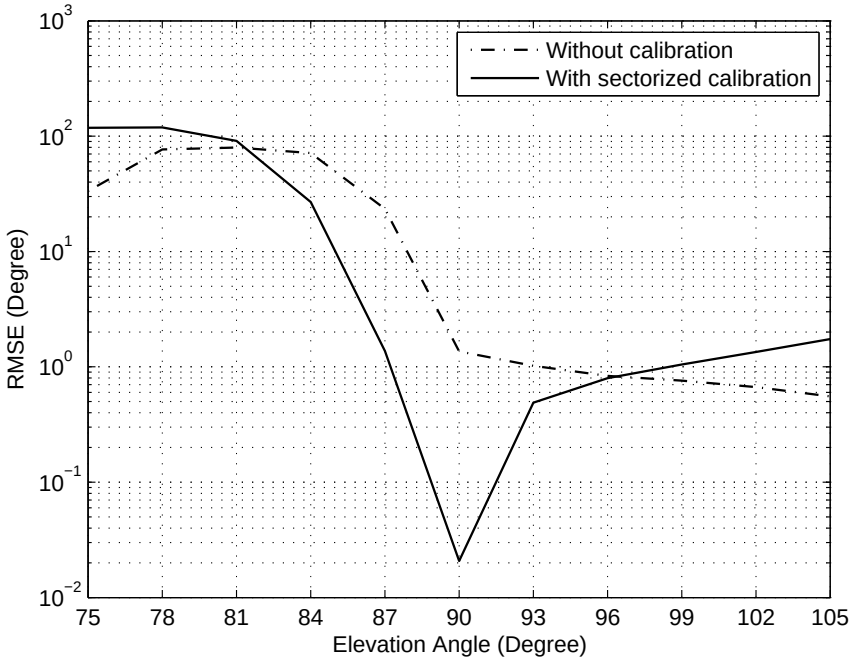

Figure 4.13: The elevation performance of the sectorized calibration approach combined with MRM where the $\mathbf{C}$ matrices found for $\theta = 90^\circ$ are used while the source elevation angle is varied from 75° to 105° with 3 degrees steps.

The performance of the sectorized approach for changes in the source frequency is also examined. The array is excited with a single source with a fixed elevation angle, $\theta = 90^\circ$. The $\mathbf{C}$ matrices found for 800 MHz are used while the source frequency is varied from 795 MHz to 805 MHz with 250 kHz steps. The source azimuth angle is swept as $\phi = 0^\circ, 1^\circ, \ldots, 359^\circ$ and the average of the RMSE values for these azimuth angles is used for each frequency value, that is:

$$E(f) = \frac{1}{360} \sum_{\phi=0^\circ}^{359^\circ} e(\phi, f), \qquad f = 795MHz, 795.25MHz, \ldots, 805MHz \tag{4.7}$$

where $e(\phi, f)$ is the RMSE value found for $(\phi, \theta = 90^\circ)$ direction at f frequency and $E(f)$ is the average error for the corresponding frequency. In Figure 4.14, the

frequency performance of the sectorized approach combined with MRM is presented. As seen in Figure 4.14, the calibrated array performance is significantly better than the uncalibrated array performance. Also, the best performance for the calibrated array is observed at 800 MHz as expected. As the source frequency is changed, the mutual coupling between the antenna elements changes, and the **C** matrix found for 800 MHz may not be satisfactory.

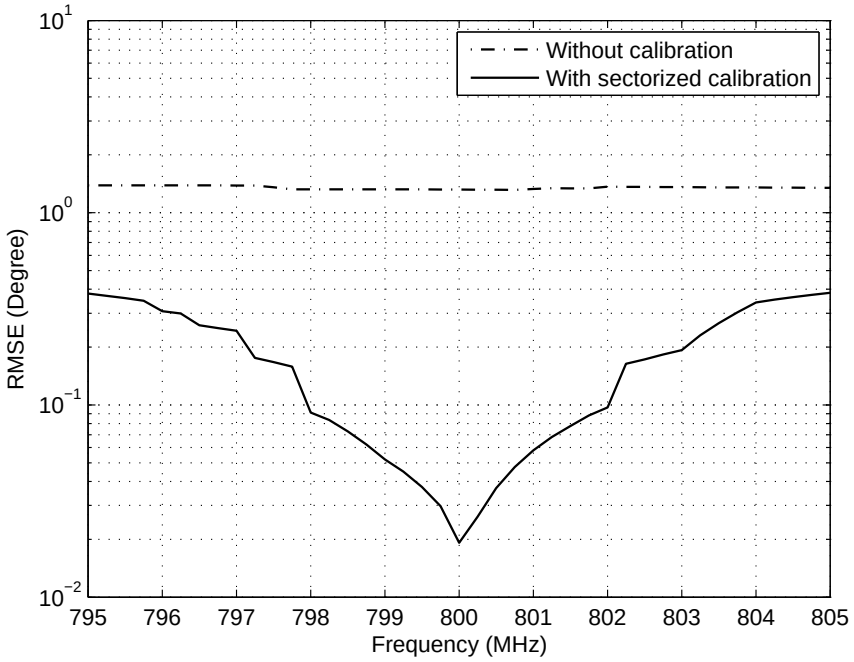

Figure 4.14: The frequency performance of the sectorized calibration approach combined with MRM where the **C** matrices found for 800 MHz are used while the source frequency is varied from 795 MHz to 805 MHz with 250 kHz steps.

CHAPTER 5

MUTUAL COUPLING AND GAIN/PHASE MISMATCH CALIBRATION OF ANTENNA ARRAYS OVER A PEC PLATE

In the previous chapters, mutual coupling effect is analyzed for antenna arrays in free space without any objects around. However, in practice, there will most probably be some objects and/or reflecting surfaces around the antenna array in DOA estimation applications. Anything around the antenna array will bring an additional distortion because of the reflections from their surfaces. In this case, the receiving pattern of the array will be distorted because of these reflections from the external objects. This will result in gain/phase mismatches in the antenna elements. Similar to mutual coupling, these gain/phase mismatches also need to be calibrated for an acceptable DOA estimation accuracy. Therefore, they should also be taken into account during the calibration of an antenna array with some objects and/or reflecting surfaces around it.

In this chapter, the case of an antenna array over a perfect electric conductor (PEC) plate is analyzed. The arrays composed of identical and omnidirectional antennas are considered. The analysis is done for two different antenna arrays, one composed of monopole antennas and another composed of dipole antennas. In order to model the mutual coupling effect together with the gain/phase mismatch caused by the PEC plate, it is proposed to use a single composite calibration matrix. The composite matrix approach is an extension to the transformation method presented in Section 3.2. In the composite matrix approach, a linear transformation is utilized to jointly model the mutual coupling and the gain/phase mismatch. Before presenting the composite

matrix approach, it is reasonable to give the signal model used under the scope of this chapter.

5.1 Signal Model

In this chapter, an antenna array composed of identical and omnidirectional antennas over a PEC plate is considered in a noise-free environment, and narrowband model is used. In this case, the output vector due to an excitation source from (ϕ_l, θ_l) direction for an N-element antenna array is represented as,

$$\mathbf{y}(t) = \mathbf{C}\,\mathbf{\Gamma}_l\,\mathbf{a}(\phi_l, \theta_l)\,s(t), \qquad t = 1, 2, \ldots, P \tag{5.1}$$

where P is the number of snapshots and $\mathbf{C}$ is the $N \times N$ mutual coupling matrix for (ϕ_l, θ_l) direction. $\mathbf{\Gamma}_l$ is an $N \times N$ matrix which stands for the gain/phase mismatch due to an excitation from (ϕ_l, θ_l) direction. $\mathbf{a}(\phi_l, \theta_l) = [\alpha_1(\phi_l, \theta_l) \quad \alpha_2(\phi_l, \theta_l) \ldots \alpha_N(\phi_l, \theta_l)]^T$ is the steering vector for (ϕ_l, θ_l) direction. The vector element corresponding to the n^{th} antenna positioned at (x_n, y_n, z_n) is $\alpha_n(\phi_l, \theta_l) = e^{j\frac{2\pi}{\lambda}(x_n \cos\phi_l \sin\theta_l + y_n \sin\phi_l \sin\theta_l + z_n \cos\theta_l)}$. $s(t)$ is the complex amplitude of the excitation source from (ϕ_l, θ_l) direction.

Note that, the mutual coupling matrix $\mathbf{C}$ denotes only the mutual coupling effect. Since we consider identical and omnidirectional antenna elements, the $\mathbf{C}$ matrix in (5.1) is the same as the $\mathbf{C}$ matrix explained in Chapter 3 which is direction independent. However, since the $\mathbf{\Gamma}_l$ matrix models the gain/phase mismatch caused by the disturbance in the receiving pattern of the array due to the PEC plate, it changes with direction. In this case, the MUSIC algorithm estimates the DOA angles as the maxima of the following spectrum,

$$P_{MU}(\phi, \theta) = \frac{1}{\mathbf{a}^H(\phi, \theta)\,\mathbf{\Gamma}_l^H\,\mathbf{C}^H\,\mathbf{E}_N\,\mathbf{E}_N^H\,\mathbf{C}\,\mathbf{\Gamma}_l\,\mathbf{a}(\phi, \theta)} \tag{5.2}$$

Note that, if the correct $\mathbf{C}$ matrix and $\mathbf{\Gamma}_l$ matrices are not supplied, the MUSIC algorithm can result errors in DOA estimation larger than 10 degrees. Therefore, it is an important task to determine the $\mathbf{C}$ matrix and $\mathbf{\Gamma}_l$ matrices to be used. However, it is also possible to model both mutual coupling and gain/phase mismatch in a single

step using a single composite calibration matrix. In this context, a composite matrix approach for calibration of antenna arrays over a PEC plate is presented in the next section.

5.2 Composite Matrix Approach

Since identical and omnidirectional antenna elements are considered, the $\mathbf{C}$ matrix is direction independent, and it can be as the inverse of the $\mathbf{T}$ matrix which is found using (3.11). Hence, the equation to find $\mathbf{C}$ can be obtained by taking the inverse of both sides of (3.11) which results as,

$$\mathbf{C} = \mathbf{V}\ \mathbf{U}^{\dagger} \tag{5.3}$$

Note that, since all the errors resulting from antenna misplacements, mismatches in cable lengths etc. are neglected, the only distortion included in the uncoupled voltages is the gain/phase mismatch due to the PEC plate. Hence, the linear relationship between the uncoupled voltage vector and the ideal steering vector for (ϕ_l, θ_l) direction is represented through $\mathbf{\Gamma}_l$ as follows,

$$\mathbf{u}(\phi_l, \theta_l) = \mathbf{\Gamma}_l\ \mathbf{a}(\phi_l, \theta_l) \tag{5.4}$$

As seen above, we end up with a direction independent $\mathbf{C}$ matrix and a direction dependent $\mathbf{\Gamma}_l$ matrix where the DOA estimation can be done using (5.2). Since $\mathbf{\Gamma}_l$ is direction dependent, we need to follow a sectorized approach to model the gain/phase mismatches for different directions.

Mutual coupling and gain/phase mismatch can be modelled separately as explained above. In this case, we need to make measurements for both coupled and uncoupled voltages. However, it is also possible to jointly model mutual coupling and the gain/phase mismatch in a single step using a composite calibration matrix. In this case, the composite calibration matrix, $\mathbf{M}_l$, is formed by two factors, $\mathbf{C}$ and $\mathbf{\Gamma}_l$, as,

$$\mathbf{M}_l = \mathbf{C}\,\mathbf{\Gamma}_l \tag{5.5}$$

In the composite matrix approach, the transformation method is extended to model the gain/phase mismatch along with the mutual coupling. Hence, the composite calibration matrix, $\mathbf{M}_l$, represents the linear relationship between the ideal steering vector and the coupled voltage vector for (ϕ_l, θ_l) direction as follows,

$$\mathbf{v}(\phi_l, \theta_l) = \mathbf{M}_l\,\mathbf{a}(\phi_l, \theta_l) \tag{5.6}$$

In this case, the MUSIC algorithm estimates the DOA angles as the maxima of the following spectrum,

$$P_{MU}(\phi, \theta) = \frac{1}{\mathbf{a}^H(\phi, \theta)\,\mathbf{M}_l^H\,\mathbf{E}_N\,\mathbf{E}_N^H\,\mathbf{M}_l\,\mathbf{a}(\phi, \theta)} \tag{5.7}$$

Note that, we do not need to make measurements to obtain uncoupled voltages whereas we need to make measurements to obtain uncoupled voltages when the $\mathbf{C}$ matrix and $\mathbf{\Gamma}_l$ matrices are found separately. On the other hand, since $\mathbf{M}_l$ is formed by a direction independent factor, $\mathbf{C}$, and a direction dependent factor, $\mathbf{\Gamma}_l$, it is direction dependent. Therefore, we need to follow a sectorized approach to find $\mathbf{M}_l$ matrices, and here comes the problem of proper sectorization. In a proper sectorization, sectors should be determined as the regions where $\mathbf{M}_l$ does not change significantly, so it can be taken as a direction independent matrix $\mathbf{M}$ within each sector.

Additional observations are required to find the $N \times N$ $\mathbf{M}$ matrix for a sector. Let $\mathbf{V}$ be an $N \times L$ matrix whose columns are the coupled voltage vectors due to L single excitation sources within the same sector. Then, (5.6) can be generalized as,

$$\mathbf{V} = \mathbf{M}\,\mathbf{A} \tag{5.8}$$

Assuming $L \geq N$, the $\mathbf{M}$ matrix for the corresponding sector can be found as,

$$\mathbf{M} = \mathbf{V}\,\mathbf{A}^{\dagger} \tag{5.9}$$

The implementation of the composite matrix approach for an N-element array composed of identical and omnidirectional antennas over a PEC plate can be summarized as follows:

1. In order to find the proper sector width, determine a performance criterion and start with two non-overlapping sectors of 180° angular width.

2. Find $\mathbf{M}$ matrices for all sectors using (5.9).

3. Using (5.7), make a performance test to see whether the $\mathbf{M}$ matrices satisfy the performance criterion or not.

4. If the performance criterion is satisfied, select the current sector width. If it is not satisfied, select a new sector width less than the current sector width and return to Step 2.

5. After the sector width is determined, the array calibration can be done using the set of $\mathbf{M}$ matrices found in the last execution of Step 2.

Consider the minimum number of measurements required in the above procedure for an N-element array. For each sector, we need at least N measurements to construct $\mathbf{V}$ in order to use in (5.9). If the number of sectors is denoted as D, we need a total of DN measurements.

In the previous chapters, measurement reduction procedures are provided for the corresponding cases. In this chapter, the case with a PEC plate under the antenna array is considered where the plate can be of any shape. If a plate without any symmetry axis in its geometry is used, the electrical symmetry will be disrupted. Hence, it will not be able to find a procedure for reducing the number of calibration measurements. However, it would be still possible to find a measurement reduction procedure if the plate has certain symmetries in its geometry. On the other hand, note that, an independent analysis should be done in order to find a measurement reduction procedure, each time the plate shape is changed. Therefore, measurement reduction concept is left out of scope for the case of an antenna array over a PEC plate.

5.3 Simulations

As in the previous chapters, the full-wave electromagnetic simulation tool FEKO [12] is used to have measurements in this part of the study. FEKO simulations are implemented by using the method-of-moments (MOM). Performance of the composite matrix approach is evaluated through DOA estimation simulations using MUSIC algorithm. In the experiments, two different planar 8-element UCA's are used, one composed of dipole antenna elements and the other composed of monopole antenna elements. The antenna arrays are located over a circular PEC plate.

The dimensions are selected such that the antenna arrays have an operating frequency band of 800-1200 MHz. The dipole diameter is chosen as 10 mm and the dipole length as 15 cm, that is the half wavelentgh at 1000 MHz. In order to avoid spatial aliasing, the distance between two array elements is chosen as 12.5 cm, that is the half wavelength at 1200 MHz. Each array element is terminated with a $Z_L = 50\Omega$ load and the simulations are carried out at 1000 MHz. The diameter of the PEC plate is chosen as 100 cm, that is greater than three times the wavelength at 1000 MHz. The dipole array is elevated 30 cm above the PEC plate. The FEKO model for the 8-element UCA with dipole antennas elevated over the circular PEC plate is presented in Figure 5.1.

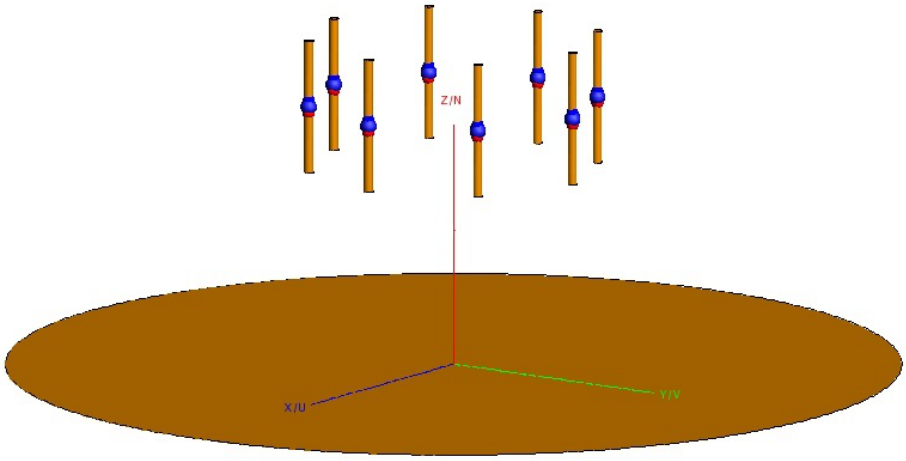

Figure 5.1: The FEKO model for the 8-element UCA with dipole antennas elevated over a circular PEC plate.

For the monopole array, there are two differences compared to the dipole array. The first difference is that the monopole length is 7.5 cm, that is half of the dipole length. The second difference is that the antenna elements are attached to the PEC plate since monopole antennas need a ground plane for proper operation. Therefore, the array is not elevated. The FEKO model for the 8-element UCA with monopole antennas attached to the circular PEC plate is presented in Figure 5.2.

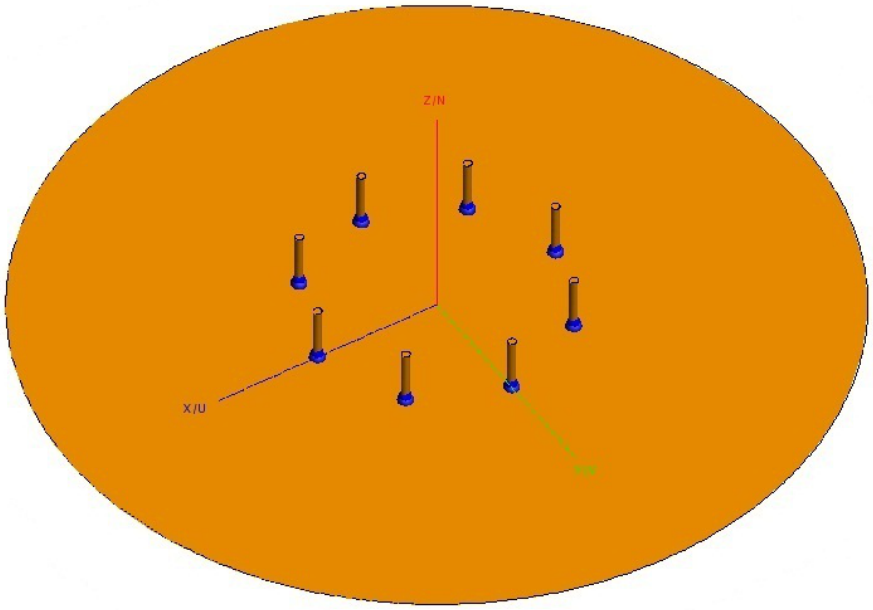

Figure 5.2: The FEKO model for the 8-element UCA with monopole antennas attached to a circular PEC plate.

In order to evaluate the performance of the composite matrix approach, the array is excited with a single source whose elevation angle is fixed and azimuth angle is swept with one degree steps, i.e., $\phi = 0°, 1°, \ldots, 359°$. The experiments are repeated for three elevation angles of $\theta = 60°, 70°, 80°$. The 5-step procedure of the composite matrix approach is followed for both the dipole and the monopole antenna arrays. In the procedure, the performance criterion is chosen as a maximum RMSE of 0.05 degree. For the dipole array, the maximum sector width satisfying this performance criterion is found to be 120 degrees. Hence, the dipole array is calibrated using three distinct composite matrices. For the monopole array, the maximum sector width satisfying this performance criterion is found to be 90 degrees. Hence, the monopole array is calibrated using four distinct composite matrices.

The source azimuth angle is fixed to be $\phi = 70^\circ$ and the MUSIC spectra are examined for the dipole array. In Figures 5.3, 5.4 and 5.5, the MUSIC spectra are given for $\theta = 60^\circ, 70^\circ, 80^\circ$, respectively. As seen in Figures 5.3, 5.4 and 5.5, there is a sharp peak at the correct azimuth angle which points that the MUSIC algorithm can properly find the DOA angle when calibration with composite matrix approach is applied. Whereas, the uncalibrated array spectrum has a smooth rise around the correct azimuth angle, but there is no explicit peak. This may cause large errors in estimating the DOA angle.

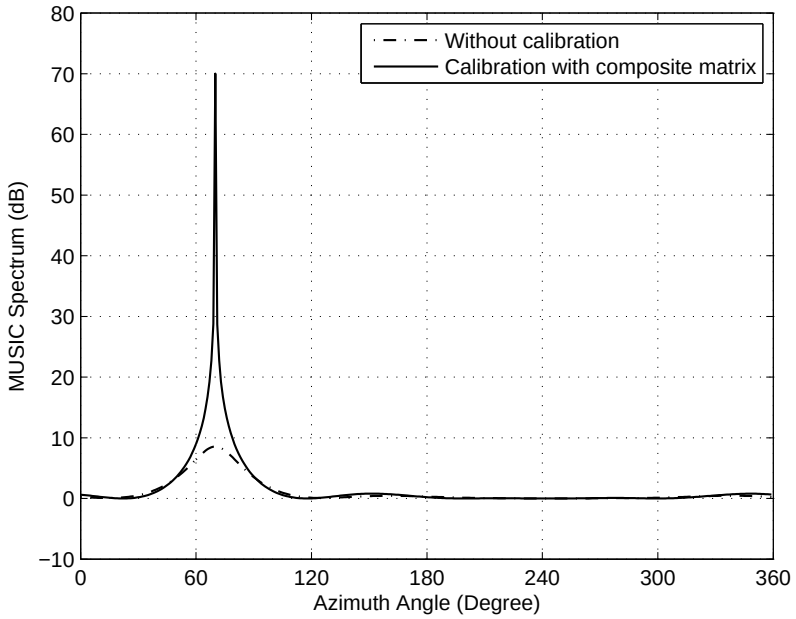

Figure 5.3: The MUSIC spectrum of the dipole antenna array calibrated using the composite matrix approach for $(\phi = 70^\circ, \theta = 60^\circ)$ direction. The composite matrices are found by using three non-overlapping azimuth sectors of 120° angular width.

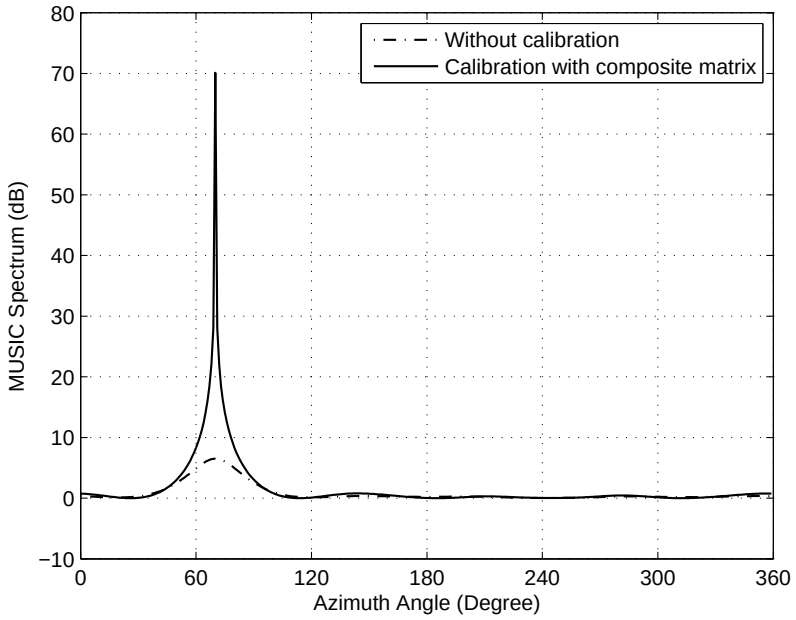

Figure 5.4: The MUSIC spectrum of the dipole antenna array calibrated using the composite matrix approach for $(\phi = 70°, \theta = 70°)$ direction. The composite matrices are found by using three non-overlapping azimuth sectors of 120° angular width.

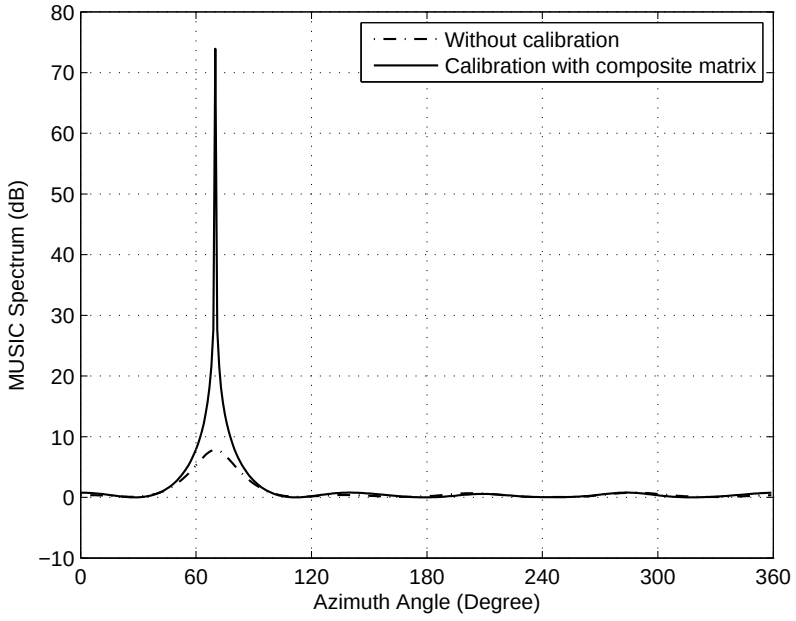

Figure 5.5: The MUSIC spectrum of the dipole antenna array calibrated using the composite matrix approach for $(\phi = 70°, \theta = 80°)$ direction. The composite matrices are found by using three non-overlapping azimuth sectors of 120° angular width.

The azimuth performances of the composite matrix approach for the dipole array are presented in Figures 5.6, 5.7 and 5.8 for $\theta = 60°, 70°, 80°$, respectively. As seen in Figures 5.6, 5.7 and 5.8, the calibrated array response is significantly better than the uncalibrated array response. Also, the determined performance criterion of maximum RMSE of 0.05 degree is satisfied in all of the three cases.

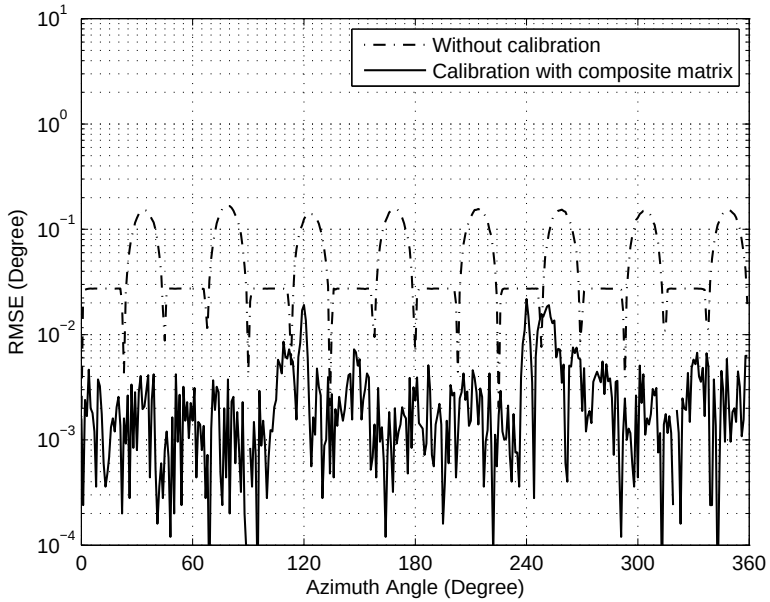

Figure 5.6: The azimuth performance of the dipole antenna array calibrated using the composite matrix approach for $\theta = 60°$. The calibration is done by using three non-overlapping azimuth sectors of 120° angular width.

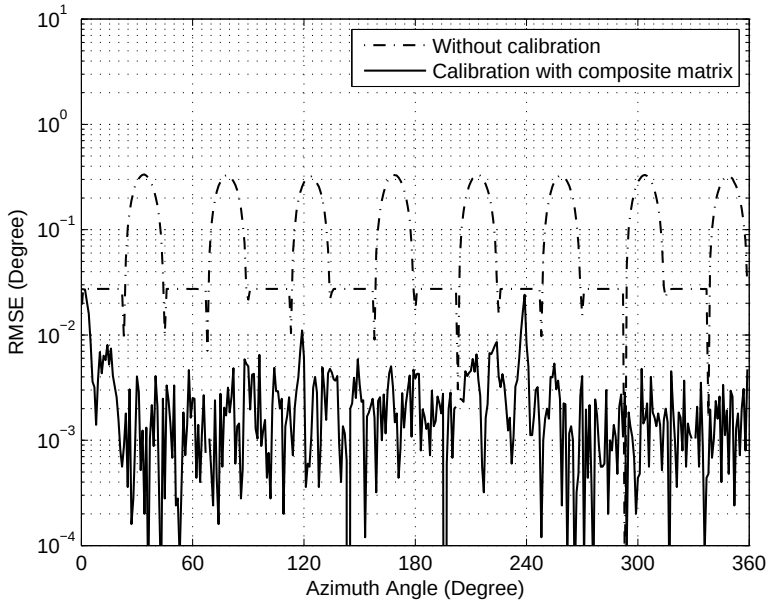

Figure 5.7: The azimuth performance of the dipole antenna array calibrated using the composite matrix approach for $\theta = 70°$. The calibration is done by using three non-overlapping azimuth sectors of 120° angular width.

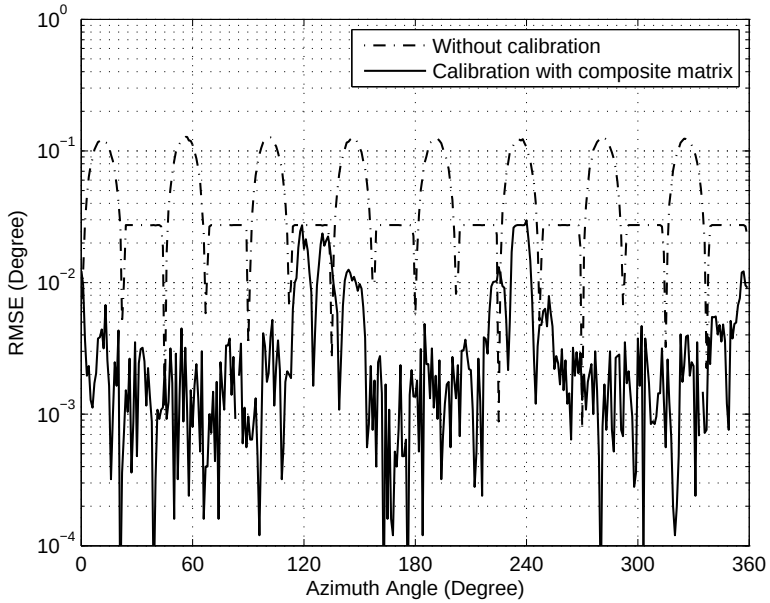

Figure 5.8: The azimuth performance of the dipole antenna array calibrated using the composite matrix approach for $\theta = 80°$. The calibration is done by using three non-overlapping azimuth sectors of 120° angular width.

When the 5-step procedure of the composite matrix approach is applied for the monopole antenna array using the same perfomance criterion of maximum RMSE of 0.05 degree, the sector width satisfying this criterion is found to be 90 degrees. The source azimuth angle is fixed to be $\phi = 80^\circ$ and the MUSIC spectra in this case are given in Figures 5.9, 5.10 and 5.11, for $\theta = 60^\circ, 70^\circ, 80^\circ$, respectively. As seen in Figures 5.9, 5.10 and 5.11, similar to the case with the dipole array, there is a sharp peak at the correct azimuth in the calibrated array spectrum, whereas, it is hard to find a distinct peak in the uncalibrated array spectrum.

When the calibrated array spectra of dipole and monopole arrays are compared for the same elevation angle, it is seen that levels of the sharp peaks in the monopole array spectra are lower than their counterparts in the dipole array spectra. On the other hand, when the same performance criterion of maximum RMSE of 0.05 degree is used for both dipole and monopole arrays, it is sufficient to use three non-overlapping angular sectors for the dipole array, whereas, the monopole array requires four non-overlapping angular sectors. Since the monopole array is closer to the plate when compared to the dipole array, the pattern disturbance in the monopole array should

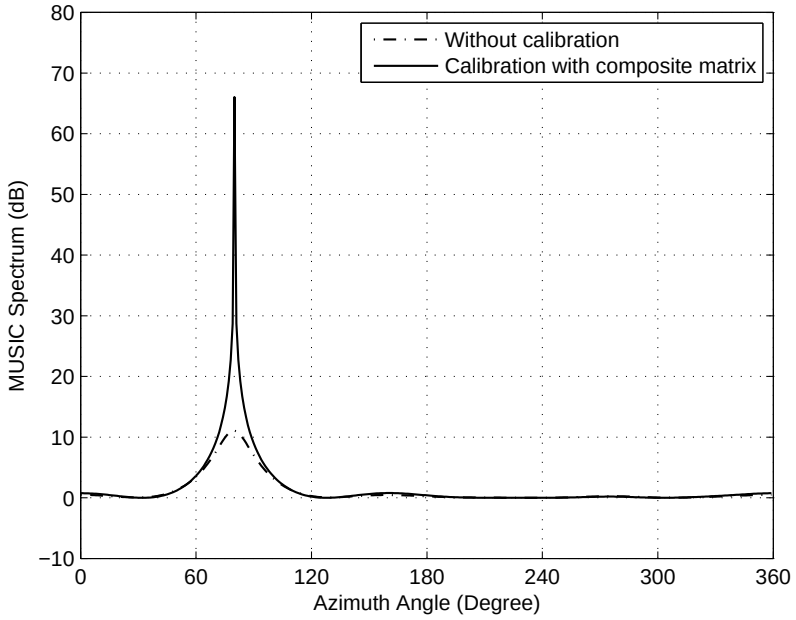

Figure 5.9: The MUSIC spectrum of the monopole antenna array calibrated using the composite matrix approach for $(\phi = 80^\circ, \theta = 60^\circ)$ direction. The composite matrices are found by using four non-overlapping azimuth sectors of 90° angular width.

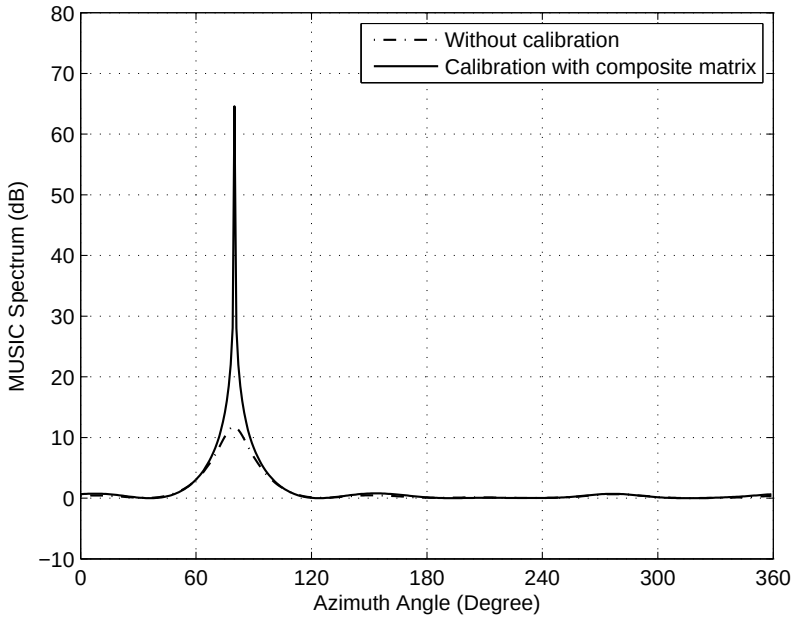

Figure 5.10: The MUSIC spectrum of the monopole antenna array calibrated using the composite matrix approach for $(\phi = 80°, \theta = 70°)$ direction. The composite matrices are found by using four non-overlapping azimuth sectors of 90° angular width.

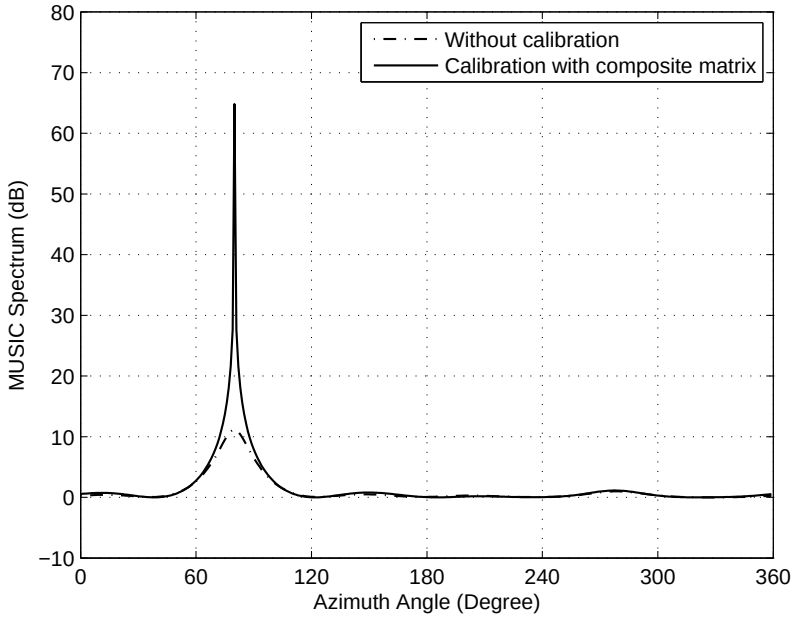

Figure 5.11: The MUSIC spectrum of the monopole antenna array calibrated using the composite matrix approach for $(\phi = 80°, \theta = 80°)$ direction. The composite matrices are found by using four non-overlapping azimuth sectors of 90° angular width.

be greater than the pattern disturbance in the dipole array. Therefore, we need more sectors for calibrating the monopole array.

The azimuth performances of the composite matrix approach for the monopole array are presented in Figures 5.12, 5.13 and 5.14 for $\theta = 60°, 70°, 80°$, respectively. As seen in Figures 5.12, 5.13 and 5.14, the calibrated array response is significantly better than the uncalibrated array response. Also, the determined performance criterion of maximum RMSE of 0.05 degree is satisfied in all of the three cases.

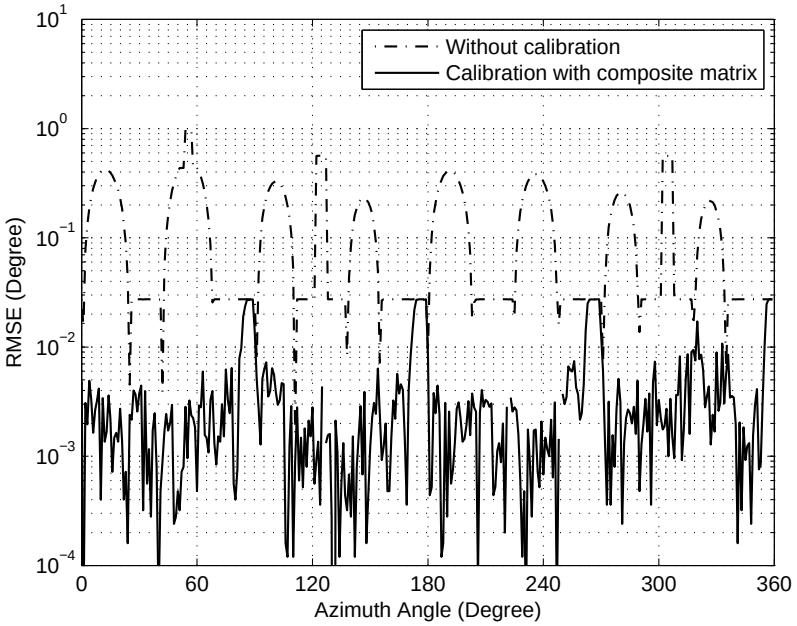

Figure 5.12: The azimuth performance of the monopole antenna array calibrated using the composite matrix approach for $\theta = 60°$. The calibration is done by using four non-overlapping azimuth sectors of $90°$ angular width.

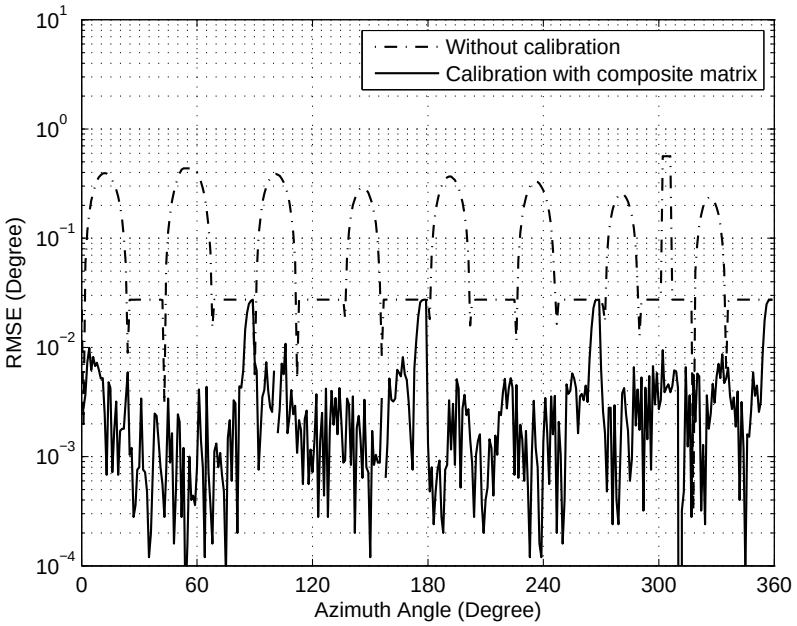

Figure 5.13: The azimuth performance of the monopole antenna array calibrated using the composite matrix approach for $\theta = 70°$. The calibration is done by using four non-overlapping azimuth sectors of 90° angular width.

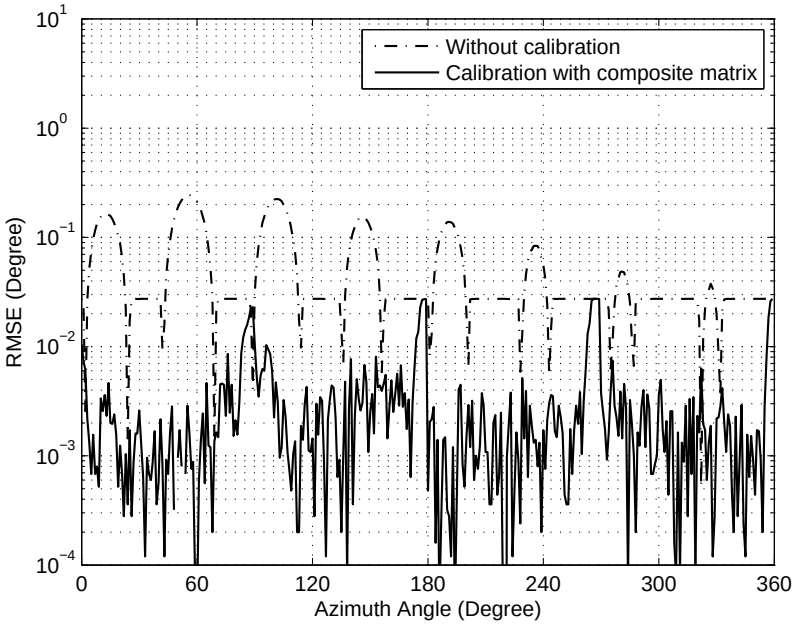

Figure 5.14: The azimuth performance of the monopole antenna array calibrated using the composite matrix approach for $\theta = 80°$. The calibration is done by using four non-overlapping azimuth sectors of 90° angular width.

In order to evaluate the performance of the composite matrix approach for the changes in source elevation angle, the dipole array is excited with a single source. The composite matrices found for $\theta = 70^\circ$ are used while the experiment is repeated for elevation angles varying from 68° to 72° with 0.25 degree steps. The source azimuth angle is swept as $\phi = 0^\circ, 1^\circ, \ldots, 359^\circ$ and the average of the RMSE values for these azimuth angles is used for each elevation angle, that is:

$$E(\theta) = \frac{1}{360} \sum_{\phi=0^\circ}^{359^\circ} e(\phi, \theta), \qquad \theta = 68^\circ, 68.25^\circ, \ldots, 72^\circ \tag{5.10}$$

where $e(\phi, \theta)$ is the RMSE value found for (ϕ, θ) direction and $E(\theta)$ is the average error for the corresponding elevation angle. The elevation performance of the composite matrix approach for the dipole array is presented in Figure 5.15. As seen in Figure 5.15, the best performance for the calibrated array is obtained for $\theta = 70^\circ$ since the composite matrices found for $\theta = 70^\circ$ are used. The calibrated array response is better than the uncalibrated array response for a sector of 2 degrees between $\theta = 69^\circ - 71^\circ$.

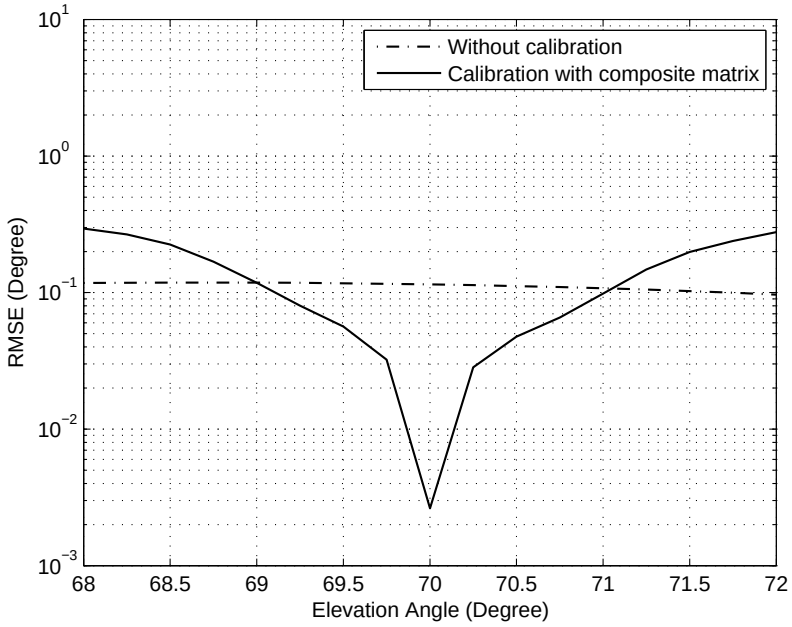

Figure 5.15: The elevation performance of the dipole antenna array calibrated using the composite matrix approach. The composite matrices found for $\theta = 70^\circ$ are used while the elevation angle is swept from 68° to 72° with 0.25 degree steps.

The experiment is repeated for the monopole array. The elevation performance of the monopole array is presented in Figure 5.16. As seen in Figure 5.16, the best performance for the calibrated array is obtained for $\theta = 70^\circ$ since the composite matrices found for $\theta = 70^\circ$ are used. The calibrated array response is better than the uncalibrated array response for a sector of 3 degrees between $\theta = 68.5^\circ - 71.5^\circ$. When Figures 5.15 and 5.16 are compared, the performance of the dipole array is better than the monopole array for $\theta = 70^\circ$. However, the composite matrices found for $\theta = 70^\circ$ work for a larger elevation sector for the monopole array.

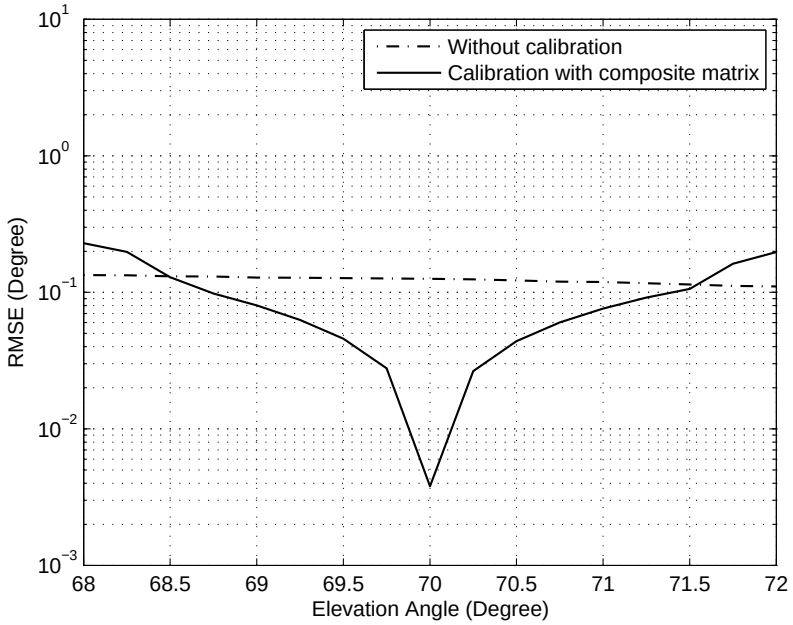

Figure 5.16: The elevation performance of the monopole antenna array calibrated using the composite matrix approach. The composite matrices found for $\theta = 70^\circ$ are used while the elevation angle is swept from 68° to 72° with 0.25 degree steps.

In order to evaluate the performance of the composite matrix approach for the changes in source frquency, the dipole array is excited with a single source. The source elevation angle is fixed to be $\theta = 70^\circ$. The composite matrices found for $f = 1000$ MHz are used, whereas the experiment is repeated for source frequencies varying from 995 MHz to 1005 MHz with 0.25 MHz steps. The source azimuth angle is swept as $\phi = 0^\circ, 1^\circ, \ldots, 359^\circ$ and the average of the RMSE values for these azimuth angles is used for each frequency value, that is:

$$E(f) = \frac{1}{360} \sum_{\phi=0^\circ}^{359^\circ} e(\phi, f), \qquad f = 995MHz, 995.25MHz, \ldots, 1005MHz \tag{5.11}$$

where $e(\phi, f)$ is the RMSE value found for $(\phi, \theta = 70^\circ)$ direction at f frequency and $E(f)$ is the average error for the corresponding frequency. The frequency performance of the composite matrix approach for the dipole array is presented in Figure 5.17. As seen in Figure 5.17, the best performance for the calibrated array is obtained for f = 1000 MHz since the composite matrices found for f = 1000 MHz are used. The calibrated array response is better than the uncalibrated array response for all the analyzed frequency band.

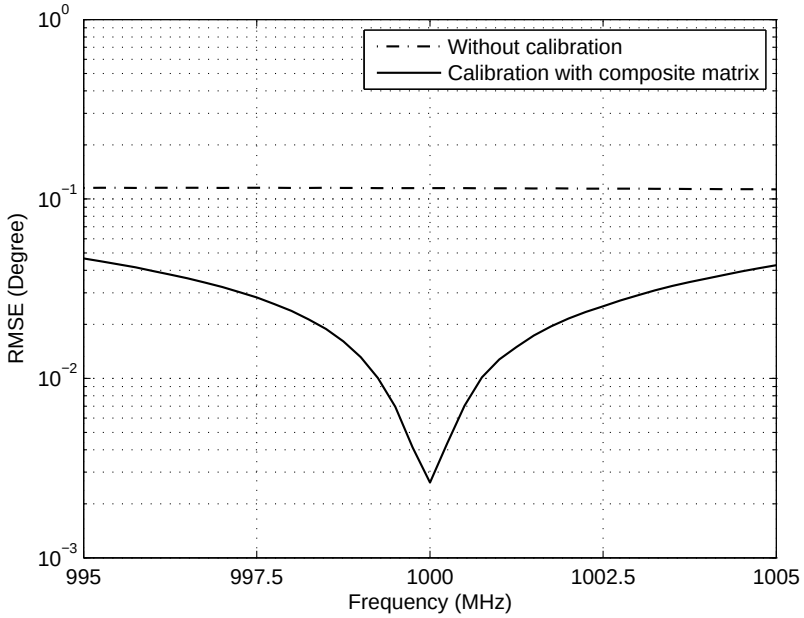

Figure 5.17: The frequency performance of the dipole antenna array calibrated using the composite matrix approach. The composite matrices found for f = 1000 MHz are used while the source frequency is swept from 995 MHz to 1005 MHz with 0.25 MHz steps.

The experiment is repeated for the monopole array. The frequency performance of the monopole array is presented in Figure 5.18. As seen in Figure 5.18, the best performance for the calibrated array is obtained for f = 1000 MHz since the composite matrices found for f = 1000 MHz are used. The calibrated array response is better than the uncalibrated array response for all the analyzed frequency band. When

Figures 5.17 and 5.18 are compared, the performance of the dipole array is better than the performance of the monopole array at $f = 1000$ MHz. However, as the frequency is deviated from 1000 MHz, there is a less amount of increase in the error for the monopole array.

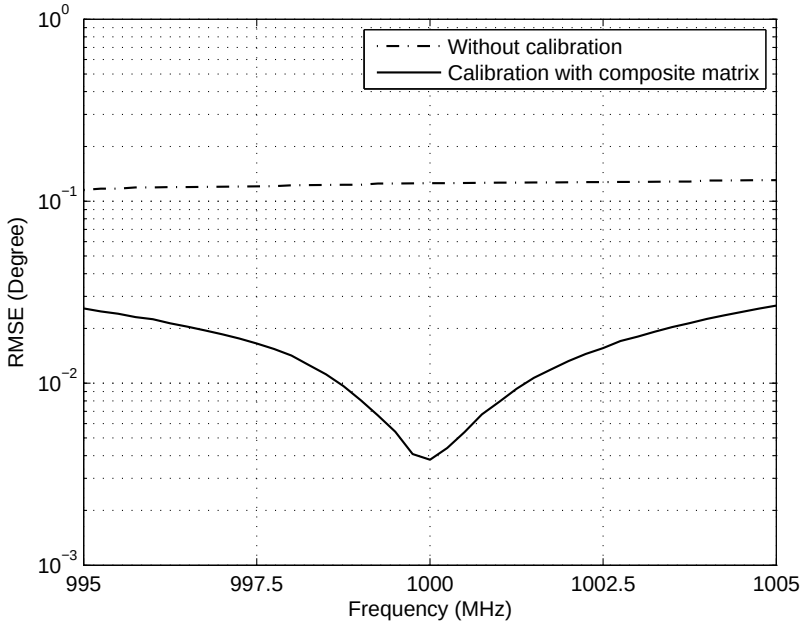

Figure 5.18: The frequency performance of the monopole antenna array calibrated using the composite matrix approach. The composite matrices found for $f = 1000$ MHz are used while the source frequency is swept from 995 MHz to 1005 MHz with 0.25 MHz steps.

CHAPTER 6

CONCLUSIONS

There are different techniques for DOA estimation where the main issue is processing the data acquired by a sensor array. In wireless communications, the arrays are constituted by antennas. There are many distortion sources in an antenna array reducing DOA estimation accuracy, such as antenna misplacements, mismatches in cable lengths, mutual coupling between antennas or gain/phase mismatches due to antenna radiation patterns. Mutual coupling is defined as the interactions between array elements caused by the scattering and re-radiation of the impinging signal from the array elements. Mutual coupling may cause large errors in DOA estimation results and should be corrected for any antenna array.

In this thesis, mutual coupling effect is analyzed for different cases and appropriate calibration methods are proposed for each case. The case of arrays with identical and omnidirectional antennas in a noise free environment is analyzed. This is the most common case treated in the literature. Hence, the initial effort is devoted to this case in this study as well. In most of the previous studies, it is seen that the proposed calibration techniques are based on antenna mutual impedances. However, there exist methods using a transfer function to model the mutual coupling effect. In this context, a similar transformation approach is presented for determining the mutual coupling matrix which is known to be direction independent for omnidirectional antennas in the literature. Transformation approach is a simple method where the relation between the measured and the ideal array data is represented through a linear transformation. Furthermore, it is computationally efficient compared to the conventional methods.

A measurement reduction method (MRM) is proposed in order to reduce the number

of measurements required in the transformation approach. MRM is based on the symmetry planes in an array geometry where multiple measurement vectors are generated from a single measured vector through data permutations. MRM leads to a significant reduction in the number of required measurements where it is shown that a single measurement is sufficient for the calibration of a UCA using MRM. While MRM uses the symmetry planes in the array, it generates the data vectors by turning 360 degrees around the antenna array. By this means, MRM has a high numerical accuracy and robustness. Moreover, it is shown that many well known array geometries, such as UCA, ULA, etc., include symmetry planes which make them suitable for the use of MRM.

In this thesis, the proposed methods are evaluated over DOA estimation accuracies using the MUSIC algorithm. The required measurements are obtained through numerical electromagnetic simulations in FEKO. In order to evalute the transformation approach combined with MRM, an 8-element UCA composed of identical dipole antennas is used. The results show that the proposed calibration technique can effectively identify and compansate for the mutual coupling effect in the antenna array. Different experiments are carried out in order to examine the effects of changes in source frequency, azimuth and elevation angles. The results show that the transformation method combined with MRM still provides an effective mutual coupling calibration under these conditions.

Secondly, the arrays composed of non-omnidirectional (NOD) antennas is considered where the mutual coupling matrix changes with direction. In this context, a single coupling matrix is shown to be insufficient for modelling the mutual coupling effect in an NOD antenna array. However, antenna pattern is a smooth function of azimuth and elevation angles for most of the antenna types. In addition, the mutual coupling effect in an antenna array does not change rapidly as the azimuth and elevation angles change. Therefore, the coupling matrix can be assumed to remain unchanged for a sufficiently small angular sector. As a result, a sectorized approach seems to be a natural choice for mutual coupling calibration of NOD antenna arrays. In this context, a sectorized calibration approach is proposed for proper calibration of NOD antenna arrays where the mutual coupling calibration is done in angular sectors. Furthermore, MRM is extended for NOD antenna arrays with identical elements. In this case,

the symmetry of the array pattern due to symmetric array elements is used, and multiple array data are generated from a single measured array data through data permutations.

A non-symmetric dipole patch antenna is used in the performance evaluations. This novel antenna is a wideband semi-omnidirectional antenna which has an omnidirectional characteristics for the lower frequency band while it exhibits a non-omnidirectional characteristics for the upper frequency band. The semi-omnidirectional antenna is used in its upper frequency band so that it can be taken as an NOD antenna. Different experiments are done in order to evaluate the performance of the sectorized calibration approach combined with MRM for the changes in source frequency, azimuth and elevation angles. The results show that the proposed approach provides a robust mutual coupling calibration for NOD antenna arrays even if the source parameters are varied as explained.

As a final study, the case of an antenna array over a perfect electric conductor (PEC) plate is analyzed. In this case, the PEC plate brings additional distortion because of the reflections from its surface. These reflections distort the receiving pattern of the antenna array which results in gain/phase mismatches in the antenna elements. Similar to mutual coupling, these gain/phase mismatches also need to be calibrated for an acceptable DOA estimation accuracy. In this context, a composite matrix approach is proposed in order to jointly model the mutual coupling and the gain/phase mismatch. In the composite matrix approach, the idea is to model both mutual coupling and gain/phase mismatch effects using a single composite calibration matrix rather than using two distinct matrices as one matrix for each effect. The composite matrix approach is an extension to the transformation method presented in Section 3.2 where a linear transformation is utilized to jointly model the mutual coupling and the gain/phase mismatch. Since gain/phase mismatch is a direction dependent effect, the composite calibration matrix is also direction dependent. Therefore, we need to follow a sectorized approach while using the composite matrix approach.

In the analysis, the arrays composed of identical and omnidirectional antennas are considered. The composite matrix approach is evaluated using a dipole antenna array elevated over a circular PEC plate and a monopole antenna array attached to a circular

PEC plate, and the results for the two arrays are compared. The evaluations are done in order to examine the performance of the approach against the changes in source frquency, azimuth and elevation angles. The results show that the composite matrix approach provides an efficient calibration for both mutual coupling and gain/phase mismatch effects. Also, the approach is robust against the changes in source frquency, azimuth and elevation angles. When the dipole and monopole arrays are compared, it is seen that the dipole array can be calibrated by using less number of sectors when compared with the monopole array. In addition to this, the composite matrices found for a particular source frequency or elevation angle can be used in a larger frequency or elevation angle interval for the monopole array when compared with the dipole array.

REFERENCES

[1] Schmidt, R. O. (1986), Multiple emitter location and signal parameter estimation, *IEEE Trans. Antennas Propag., 34(3)*, 276–280.

[2] Hui, H. T. (2007), Decoupling methods for the mutual coupling effect in antenna arrays: a review, *Recent Pat. Eng., 1*, 187–193.

[3] Gupta, I. J., A.A. Ksienski (1983), Effect of mutual coupling on the performance of adaptive arrays, *IEEE Trans. Antennas Propag., 31(9)*, 785–791.

[4] Hui, H. T. (2002), Reducing the mutual coupling effect in adaptive nulling using a re-defined mutual impedance, *IEEE Microwave Wireless Compon. Lett., 12(5)*, 178–180.

[5] Hui, H. T. (2003), Compensating for the mutual coupling effect in direction finding based on a new calculation method for mutual impedance, *IEEE Antennas Wireless Propag. Lett., 2*, 26–29.

[6] Hui, H. T. (2004), A practical approach to compensate for the mutual coupling effect in an adaptive dipole array, *IEEE Trans. Antennas Propag., 52(5)*, 1262–1269.

[7] Lui, H. S., H.T. Hui (2010), Effective mutual coupling compensation for direction-of-arrival estimations using a new, accurate determination method for the receiving mutual impedance, *J. Electromagn. Waves Appl., 24*, 271–281.

[8] Yamada, H., Y. Ogawa, Y. Yamaguchi (2005), Mutual impedance of receiving array and calibration matrix for high-resolution DOA estimation, *IEEE/ACES Int. Conf. Wireless Comm. Applied Comp. Electromagn.*, 361–364.

[9] Sato, T., R. Kohno (2006), New calibration matrix calculation method for removing the effect of mutual coupling for uniform linear arrays, *IEEE 63rd Vehic. Tech. Conf., (6)*, 2686–2690.

[10] Mir, H. S. (2007), Transfer function based approaches to array calibration, *J. Commun. 2(3)*, 58–63.

[11] Aksoy, T., T.E. Tuncer (2011), Measurement reduction for mutual coupling calibration in DOA estimation, *submitted to Radio Science.*

[12] User's Manual, FEKO (2008), *EM Software and Systems S.A. Ltd.*

[13] Hui, H.T., M.E. Bialkowski, H.S. Lui (2010), Mutual coupling in antenna arrays, *Int. J. Antennas Propag.,* Article ID 736701, 1–2.

[14] Mirkamali, A., J. Nateghi, L.A. Asl (2009), Evaluation of mutual coupling models for calibrating the antenna arrays for DOA estimation, *Eur. Conf. Antennas Propag., 3rd, EuCAP 2009,* 1033–1036.

[15] Jordan, E.C. (1968), Electromagnetic Waves and Radiating Systems, Chapter 11, *Prentice-Hall Inc., Englewood Cliffs, N.J.*

[16] Friedlander, B., A.J. Weiss (1991), Direction finding in the presence of mutual coupling, *IEEE Trans. Antennas Propag., 39(3)*, 273–284.

[17] T.E. Tuncer (2011), Nonsymmetric wideband dipole antenna, *patent pending.*